Simulation of Hydraulic Jump to detect Heat Dissipation for 2Different Ambient Temperatures

A thesis
Submitted by

SUBHAM PAL

EXAMINATION ROLL NO: M6WRP22015

For partial fulfilment of the requirements for the degree of

MASTER OF ENGINEERING
in **Water Resources and Hydraulic Engineering**
Course affiliated to Faculty of Engineering & Technology
Jadavpur University

Under the guidance of

Dr. SUBHASISH DAS
Associate Professor
School of Water Resources Engineering
Jadavpur University

School of Water Resources Engineering
M.E. (Water Resources & Hydraulic Engineering)
course affiliated to
Faculty of Engineering & Technology
Jadavpur University
Kolkata-700032, India
2022

Simulation of Hydraulic Jump to detect Heat Dissipation for Different Ambient Temperatures

A thesis
Submitted by

SUBHAM PAL

EXAMINATION ROLL NO: M6WRP22015

For partial fulfilment of the requirements for the degree of

MASTER OF ENGINEERING
in **Water Resources and Hydraulic Engineering**
Course affiliated to Faculty of Engineering & Technology
Jadavpur University

Under the guidance of

Dr. SUBHASISH DAS
Associate Professor
School of Water Resources Engineering
Jadavpur University

School of Water Resources Engineering
M.E. (Water Resources & Hydraulic Engineering)
course affiliated to
Faculty of Engineering & Technology
Jadavpur University
Kolkata-700032, India
2022

DECLARATION OF ORIGINALITY AND COMPLIANCE OF ACADEMIC ETHICS

I hereby declare that this thesis contains a literatures survey and original research work by the undersigned candidate, as part of my **Master of Engineering** in **Water Resources & Hydraulic Engineering** (6 Semester) in the Faculty of Interdisciplinary Studies, Jadavpur University during the academic session 2021-2022.

All information in this document has been obtained and presented in accordance with academic rules and ethical conduct.

I also declare that, as required by these rules and conduct, I have fully cited and referenced all materials and results that are not original to this work.

Name	**:**	**SUBHAM PAL**
Exam Roll Number	**:**	**M6WRP22015**
Thesis Title	**:**	**Simulation of Hydraulic Jump to detect Heat Dissipation for Different Ambient Temperatures**
Signature with Date	**:**	

CERTIFICATE OF RECOMMENDATION

This is to certify that the thesis entitled **"Simulation of Hydraulic Jump to detect Heat Dissipation for Different Ambient Temperatures"** is a bonafide work carried out by **Mr. Subham Pal** under my supervision and guidance for partial fulfilment of the requirement for the Post Graduate Degree of Master of Engineering in Water Resources & Hydraulic Engineering (6 Semester) during the academic session 2021-2022.

THESIS ADVISOR
Dr. Subhasis Das
Associate Professor
School of Water Resources Engineering
Jadavpur University

DIRECTOR
Prof. (Dr.) Pankaj Kumar Roy
School of Water Resources Engineering
Jadavpur University

DEAN
Prof. (Dr.) Subenoy Chakraborty
Faculty of Interdisciplinary Studies, Law & Management
Jadavpur University

CERTIFICATE OF APPROVAL **

This foregoing thesis is hereby approved as a credible study of an engineering subject carried out and presented in a manner satisfactorily to warranty its acceptance as a prerequisite to the degree for which it has been submitted. It is understood that by this approval the undersigned do not endorse or approve any statement made or opinion expressed or conclusion drawn therein but approve the thesis only for the purpose for which it has been submitted.

Committee of Final Examination for
evaluation of the thesis

******Only in case the thesis is approved

ACKNOWLEDGEMENTS

*I express my sincere gratitude to my thesis supervisor **Dr. Subhasish Das**, Associate Professor, School of Water Resources Engineering, Jadavpur University, under whose supervision and guidance this work has been carried out. It would have been impossible to carry out this thesis work with confidence without his wholehearted involvement, advice, support, and constant encouragement throughout. Dr. Subhasish Das, being a wonderful human being, shall always be a source of inspiration to me for pursuing higher education and research works.*

*I would express my sincere thanks to **Prof. (Dr.) Arunabha Majumder**, Emiretus Professor; **Pror. (Dr.) Asis Mazumdar,** Professor; **Prof. (Dr.) Pankaj Kr. Roy**, Director; **Dr. Rajib Das**, Assistant Professor; **Dr. Gourab Banerjee**, Assistant Professor of school of Water Resources Engineering, Jadavpur University , for being wonderful teachers throughout the course.*

*I would like to express my deepest thanks to **Mr. Saikat Mondal**, Research scholar, School of Water Resources Engineering for his unparalleled support and practical suggestions throughout my work. I must also thank **Mr. Buddhadeb Nandi,** Research scholar, School of Water Resources Engineering for extending his ingenious suggestions.*

Finally, I would like to express my gratitude to my parents and thanks to my younger brother to whom I owe this work. They have been a source of moral support and perseverance.

Date:
Place: Jadavpur University

SUBHAM PAL
(M6WRP22015)

ABSTRACT

Hydraulic jump has been a very interesting topic of study for its wide application in industries and environmental engineering. A lot of work regarding its capability of energy dissipation and aeration has been conducted in past and with the advent of several simulation softwares, several attempts are being made successfully to simulate the phenomenon. Modern society is heavily dependent on power plants and a wide range of industries that in turn discharge thermally polluted water into the water bodies like canals, rivers, and lakes. The hydraulic jump could be an efficient and economic means of dissipating heat from the water discharged from the power plants and other industries. However, this topic has not been extensively studied.

The present study attempts to simulate a hydraulic jump in a simple rectangular flume and determine the capability of the hydraulic jump to enhance the dissipation of heat from the water to the ambient. The inlet water temperature was kept constant at 40ºC while six different ambient temperatures were considered – 10ºC, 15ºC, 20ºC, 25ºC, 30ºC and 35ºC. The hydraulic jump for each of the ambient temperature was simulated and the drop in average temperature at a section downstream of the jump was determined. Drops in average specific entropy and average specific enthalpy were also determined and these drops in average temperature, specific enthalpy and specific entropy, for each ambient temperature, were compared with the drop in the corresponding quantities due to natural convection and conduction without the occurrence of hydraulic jump.

The heat transfer from the water to the ambient aided by hydraulic jump resulted in an improvement in the drop in temperature, specific entropy, and specific enthalpy as compared to the drops in these quantities owing to heat transfer due to convection and conduction without the hydraulic jump. This improvement showed a non-linear variation with the ambient temperature and decreased with the increase in ambient temperature. However, for establishing the exact relationship between this enhancement of drop in temperature, specific enthalpy, and specific entropy by hydraulic jump with the ambient temperature and also the water temperature, a few more simulations with different water temperatures and with few more ambient temperatures have to be performed.

TABLE OF CONTENTS

Topics **Page no.**

List of Figures

List of Tables

CHAPTER 1

1.1 Introduction

The 21st century has seen a tremendous growth in the number of thermal, nuclear and hydel power stations and industrial plants that have been installed and are operational both within the country and abroad. These Power stations and many industrial plants discharge thermally polluted water to the natural water bodies such as rivers, canals, bays or lakes, consequently damaging the aquatic life. Though there are several methods to cool the heated water before discharging into the water bodies, the application of the hydraulic jump to enhance the dissipation of heat to the ambient could be of both technological and economic significance.

The heat transfer between the natural water bodies, which mostly involves turbulent flows, and the atmosphere is itself a complex phenomenon and several models exist for studying the same. Williams (1963), in his paper, presented measurements of heat losses from a lake through convection and radiations. Spalding (1977) discussed the laws governing heat and mass transfer between rivers, lakes, bays and estuaries. Jobson and Keefer *(*1979) developed a numerical model for highly transient flow involving mass and heat transfer in rivers and particularly applied this model to Chattahoochee river, Georgia to predict and verify temperature changes in the month of October and March, along the entire reach of the river. The prediction showed good results when verified. Stang (1982) developed a simple model for the heat exchange between flowing water and the atmosphere and applied this model to the Orkla river to demonstrate the capability of analysis of diurnal variations of water and air temperature to predict the downstream decay of the temperature changes originating from the man-made releases. Rashidi *et al.* (1991) studied the mechanism of heat and mass transport between the gas-liquid interface and the corresponding models. Hydraulic jump involves vigorous aeration and hence the effect of aeration in heat transfer is also of significance. Several investigators (Ford *et al*., 1972; Novotny and Krenkel, 1973; Talati, 1988; Gulliver *et al.*, 1990; Chanson *et al.*, 2007) have studied the air entrainment in free-surface flows, the heat and mass transfer during aeration and have developed suitable numerical models to capture these phenomena.

In recent years, due to overwhelming progress in computation algorithms and capabilities, several CFD codes have been developed and implemented to simulate the open channel flows with heat and mass transfer. These CFD codes are also capable of simulating hydraulic jumps and resolving the air-water interaction with good accuracy. Numerical simulation and analysis of hydraulic jumps with several turbulence models have been conducted by many researchers. Among the RANS models, standard k-ε models were applied by Chipadda (1996), Zhao *et al.* (2004), and Harada and Li (2018). Numerical simulations of hydraulic jumps were studied by Carvalho *et al.* (2008), and Abbaspour and Farsadizadeh (2009) using the RNG k-ε model. Bayon and Jimenez (2015) conducted a comparison study of numerical simulation of the hydraulic jump using the Standard k-ε model, RNG k-ε model and SST k-ω model. Bayon *et al.* (2016) tested the capabilities of OPEN FOAM and FLOW 3D CFD codes to numerically simulate the hydraulic jump. Viti *et al.* (2018) presented a comprehensive study of several other turbulence models and their comparative capabilities to simulate the hydraulic jump.

Both in the past and present, investigations have been conducted in an attempt to study the relationship between hydraulic jumps and the temperature of the water. Baddour (1990) explored the characteristics of a thermal-hydraulic jump at two different ambient temperatures. Rahber *et al.* (2008) conducted several experiments investigating the effect of various hydraulic structures on cooling heated water in open channels. Simulations using CFD codes were also carried out to verify the results. Wang and Khayat (2019) studied the influence of hydraulic jump obtained over a heated circular disc. Mondal *et al.* (2020) attempted to study the thermal effect on the oscillating hydraulic jump.

Although open channel flows with and without involving the hydraulic jumps have been simulated by implementing several turbulence models, the effect of hydraulic jumps on heat transfer between water and the ambient has not been simulated extensively. Given, all the progress achieved to date in simulating the hydraulic jump and heat-mass exchange in turbulent flows using several models and CFD codes, there remains scope for investigating the nature of heat transfer aided by hydraulic jump. The present study focuses on simulating a hydraulic jump in a rectangular flume using Ansys fluent and thereby observing the effect of heat transfer from the water to the ambient on average thermal quantities of flow such as temperature, specific entropy, and specific enthalpy for six different ambient temperatures. It was found that the hydraulic jump tends to increase the drop in temperature, specific enthalpy and specific entropy at a section downstream of the jump as compared to a drop in the corresponding quantities just with natural convective and conduction heat transfer. However, the reason for this and the exact nature of the hydraulic jump in dissipating the heat for different temperature differences between the ambient and the water remains a matter of further study.

1.2 Hydraulic Jump

Hydraulic jump is an interesting phenomenon that occurs in an open channel flow when a supercritical stream meets a subcritical stream of sufficient depth. The depth of the supercritical flow is considerably lower than the depth of the subcritical flow and when these two streams meet, there is a rapid change in depth characterised by the formation of large-scale eddies and a reverse flow roller. The supercritical stream jumps to meet its alternate depth but due to the large disturbances and reverse flow, it falls short of its alternate depth resulting in a huge loss of energy. The roller is basically a huge amount of air entrained within the water and there is an intense continuous turbulent mixing of air and water that gives the roller a consequent white, choppy and frothy appearance. Since several flow properties change abruptly within a very short distance, the hydraulic jump is an example of a rapidly varied flow. Hydraulic jump serves as an energy dissipator in applications where excess energy of the flow downstream of a hydraulic structure, such as a spillway or sluice gate, has to be dissipated. Hydraulic jump also finds its application in the mixing of chemicals, in deaeration or gas transfer in chemical processes, in desalination of seawater, and in aeration of streams which are polluted by bio-degradable wastes. Fig. 1.1 is a sketch of a hydraulic jump formed in a prismatic horizontal channel.

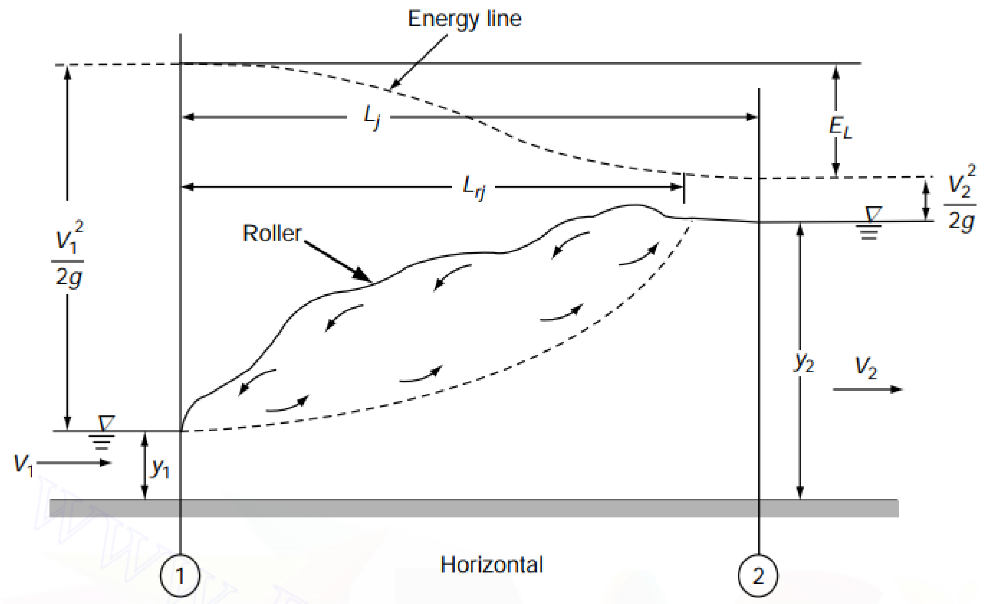

Fig. 1.1 Sketch of a hydraulic jump. y_1 and y_2 are the flow depths corresponding to supercritical and subcritical streams. L_j is the jump length and L_{rj} denotes the roller length

1.2.1 Belanger Momentum Equation

Application of momentum equation across section 1 and section 2 (Fig. 1.1), yields an equation, well known as Belanger momentum equation (Eq. 1.1), relating sequent depth ratio (y_2/y_1) and the initial Froude number F_1:

$$\frac{y_2}{y_1} = \frac{1}{2}\left(-1+\sqrt{1+8F_1^2}\right) \tag{1.1}$$

where

$F_1 = \frac{V_1}{\sqrt{g.y_1}}$; V_1 = average velocity of flow at section 1.

1.2.2 Energy Loss in Hydraulic Jump

The loss of specific energy due to hydraulic jump is expressed as:

$$E_L = E_1 - E_2$$

or

$$E = \left(y_1 + \frac{q^2}{2gy_1^2} \right) - \left(y_1 + \frac{q^2}{2gy_2^2} \right) \tag{1.2}$$

where

E_1 and E_2 are specific energy of flow at section 1 and section 2.

q=Volume flow rate per unit width of the channel.

This energy loss can be expressed in terms of the flow depths y_1 and y_2 as:

$$E_L = \frac{\left(y_2 - y_1\right)^3}{4y_1y_2} \tag{1.3}$$

The relative energy loss in terms of the initial Froude number is expressed as:

$$\frac{E_L}{E_1} = \frac{\left(-3 + \sqrt{1+8F_1^2}\right)^3}{8\left(2+F_1^2\right)\left(-1+\sqrt{1+8F_1^2}\right)} \tag{1.4}$$

1.3 Turbulent Flow

Turbulent fluid motion can be described as an irregular condition of flow in which various quantities show a random variation with time and space so that statistically distinct average values can be discerned. Many researchers describe turbulence as eddying motion which is a locally swirling motion where vorticity could be very intense. These eddies are present in varying scales within the turbulent motion and are responsible for imparting a mixing nature to the flow. Almost all fluid motions that we encounter in nature and in engineering applications involve turbulence. At large Reynolds numbers, fluids inertia overcomes the viscous stresses and the laminar motion becomes unstable. Rapid velocity and pressure fluctuations appear and a two-dimensional motion becomes inherently three-dimensional and unsteady. When this occurs, we describe the motion as being turbulent. A turbulent flow has a number of characteristic features:

- Irregularity: Turbulent flow is irregular and chaotic consisting of eddies of different scales. These turbulent eddies exist within a certain region for a certain time and are consequently destroyed by the cascade process (Fig. 1.2). They have a characteristic length and velocity. The largest eddies can be of the order of flow geometry (i.e. boundary layer thickness, jet width etc.) and at the other end of this spectrum of eddies, we have the smallest eddies which are dissipated by the viscous forces into thermal energy. Even though the turbulence is chaotic, it is deterministic and is described by Navier-Stokes equations.
- Diffusivity: In turbulent flow the diffusivity increases. The turbulence increases the exchange of momentum within and across boundary layers. The increased diffusivity also increases the resistance (wall friction) and heat transfer.
- Large Reynolds numbers: Turbulent flows occur at a high Reynolds number. In the case of open channel flows the transition from laminar to turbulence occurs for Reynolds numbers greater than 1000 and less than 3000.
- Vortex Stretching: The vorticity in turbulent flow is itself three-dimensional so that the vortex lines in the flow are non-parallel. The resulting vigorous stretching in vortex lines maintains ever-present fluctuating vorticity in turbulent flows.
- Continuum: Even though we have small turbulent scales in the flow, they are much larger than the molecular scale and we can treat the flow as a continuum.

1.3.1 Smallest scales of turbulence

The cascade process present in all turbulent flows involves a transfer of turbulence kinetic energy (per unit mass), k, from larger eddies to smaller eddies. Dissipation of kinetic energy to heat through the action of molecular viscosity occurs at the scale of the smallest eddies. Small scale eddying motions are independent of the relatively slow dynamics of large eddies and of the mean flow. The smaller eddies are in a state where the rate of receiving energy from the larger eddies is very nearly Equal to the rate at which the smallest eddies dissipate the energy to the heat. This is the well-known Kolmogorov's universal Equilibrium theory. According to this theory, the motion at the smallest scales is dependent upon the rate at which the larger eddies supply energy, represented as, $\varepsilon = -dk/dt$ and the kinematic viscosity, ν.

After establishing ε and ν as appropriate dimensional quantities, the following length (η), time (τ) and velocity (υ) scales can be obtained:

$$\eta \equiv \left(\nu^3/\varepsilon\right)^{1/4} \quad , \quad \tau \equiv \left(\nu/\varepsilon\right)^{1/2} \quad , \quad \upsilon_\eta \equiv \left(\nu\varepsilon\right)^{1/4} \qquad (1.5)$$

These are the Kolmogorov scales of length, time and velocity.

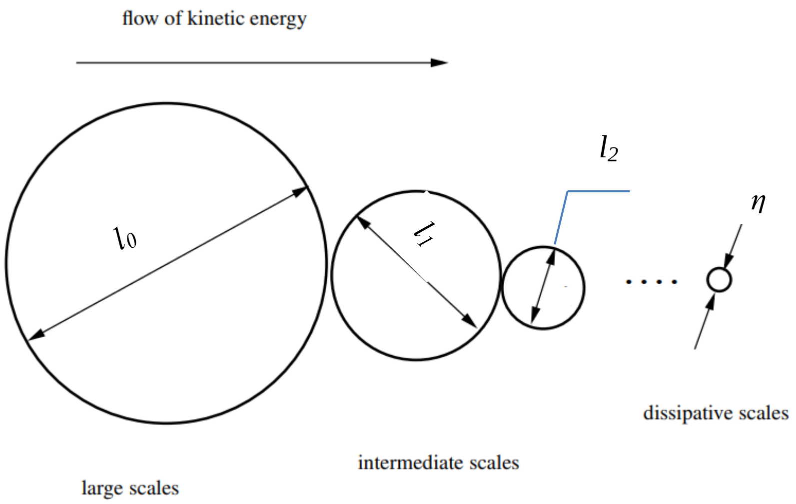

Fig. 1.2 Cascade process with a spectrum of eddies. The energy-containing eddies are denoted by l_0; l_1 and l_2 denote the size of the eddies in the inertial subrange such that $l_2 < l_1 < l_0$; η is the size of the dissipative eddies.

1.3.2 Spectral Representation

Turbulence contains a continuous spectrum of scales and as such, it is often convenient to analyse the turbulence energy in terms of the spectral distribution of energy. In general, a spectral representation is a Fourier decomposition into wavenumbers, κ. In this context, the reciprocal of κ can be thought of as eddy size.

If E(κ)*d*κ is the turbulence kinetic energy contained between wavenumbers κ and κ + *d*κ, we can say,

$$k = \int_0^\infty E(\kappa) d\kappa \tag{1.6}$$

where k is the total turbulent kinetic energy per unit mass given by

$$k = \frac{1}{2}\left(\overline{u_i' u_i'}\right) \tag{1.7}$$

The spectrum of E is shown in Fig. 1.3. There exist three regions within the energy spectrum:

- Region I – In this region, we have large eddies which carry most of the energy. These eddies interact with the mean flow and extract energy from the mean flow. Part of the energy extracted per unit time by the largest eddies is transferred to slightly smaller scales. The eddies' velocity and the length scales are v_o and l_0 respectively.

- Region III – Also known as dissipation range. The eddies are small and isotropic and here the turbulent kinetic energy is dissipated to thermal energy. The energy transfer is governed by ε. The scales of the eddies are described by Kolmogorov's scale.
- Region II – Termed as inertial subrange, the existence of this region requires that the Reynolds number is high (fully turbulent flow). The eddies in this region represent the mid-region and the turbulence is also isotropic here. This region is the transport region in the cascade process, the transport being termed as the spectral transfer. Energy per unit time, ε, is coming from larger eddies at the lower part of this range and is transferred per unit time to the dissipation range at the higher part. The eddies in this region, being independent of both the large eddies and the small eddies in the dissipation range, is characterised by the spectral transfer of energy per unit time (ε) and the size of the eddies ($1/\kappa$).

  Dimension analysis shows that the spectral distribution of kinetic energy in this region is given by:

  $$E(\kappa) = C_K \varepsilon^{\frac{2}{3}} \kappa^{-\frac{5}{3}} \tag{1.8}$$

  where the Kolmogorov constant, $C_K \simeq 1.5$.This is known as Kolmogorov's -5/3 law.

It can be proved that the ratio velocity (v_0), length (l_0) and time (τ_0) scales of larger eddies to the corresponding velocity, length and times scales of the smaller eddies is of the following form:

$$\frac{\upsilon_0}{\upsilon_\eta} = (\upsilon_0 l_0 / \nu)^{1/4} = \mathrm{Re}^{1/4} \quad , \quad \frac{l_0}{\eta} = \mathrm{Re}^{3/4} \quad , \quad \frac{\tau_0}{\tau} = \mathrm{Re}^{1/2} \tag{1.9}$$

These ratios increase with increasing Reynolds number and hence larger the eddy, the larger the difference between the smallest and largest scales and the larger the eddy range of the intermediate range. With a computational grid, we must resolve all the eddies. So the Reynolds number increases, the number of grid cells increases rapidly and the computational cost also becomes expensive.

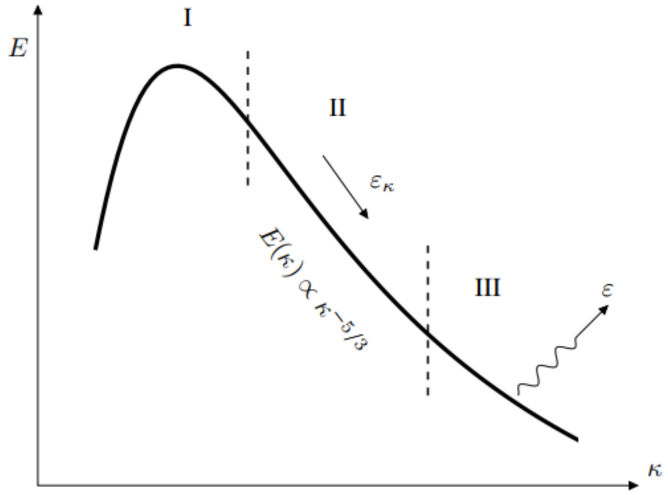

Fig. 1.3 Spectrum of turbulent kinetic energy, *k*. Region I corresponds to large eddies. Region II corresponds to the inertial subrange that dissipates the kinetic energy of relatively large eddies to smaller eddies. Region III corresponds to the smallest eddies that dissipate their kinetic energy in form of heat.

1.3.3 Reynold’s Averaged Navier-Stokes Equation

In general, for incompressible flow, the Navier Stokes equations can be written as follows in Eqs. (1.10-1.11) (Davidson, 2022):

$$\frac{\partial u_i}{\partial x_i} = 0 \tag{1.10}$$

$$\rho \frac{du_i}{dt} = -\frac{\partial p}{\partial x_i} + \frac{\partial}{\partial x_j}\left[\mu\left(\frac{\partial u_i}{\partial x_j} + \frac{\partial u_j}{\partial x_i}\right)\right] + \rho f_i \tag{1.11}$$

In turbulent flows, the instantaneous variables are decomposed into a mean value and a fluctuating value, i.e.

$$u_i = \overline{u}_i + u_i'$$

$$p = \overline{p} + p' \tag{1.12}$$

where in general, any quantity a' represents fluctuating value and $\overline{a}$ denotes a time average of quantity a defined as

$$\overline{a} = \frac{1}{2T}\int_{-T}^{T} a dt \tag{1.13}$$

where T is sufficiently large.

Time averaging all the components of velocities and pressure in the Navier stokes equations (Eqs. 1.10-1.11) and with few modifications, we obtain the following sets of equations:

$$\frac{\partial \overline{u}_i}{\partial x_i} = 0 \tag{1.14}$$

$$\rho \overline{u_j} \frac{\partial \overline{u}_i}{\partial x_j} = -\frac{\partial \overline{p}}{\partial x_i} + \frac{\partial}{\partial x_j}\left(\mu \frac{\partial \overline{u}_i}{\partial x_j} - \rho \overline{u_i' u_j'} \right) \tag{1.15}$$

Eq. 1.14 is the time-averaged continuity equation and Eq. 1.15 is the time-averaged Navier-Stokes equation. These equations are called Reynolds Averaged Navier Stokes (RANS) equation. New terms $\rho \overline{u_i' u_j'}$ appear on the right side of Eq. 1.14 which are collectively known as Reynolds stress tensor. This tensor is symmetric i.e. $\overline{u_i' u_j'} = \overline{u_j' u_i'}$. The terms appearing in the Reynolds stress tensor are additional terms and are unknown. So the number of unknowns is seven (three components of velocity, pressure and three stresses) but the number of Equations is four (continuity equation and three components of the momentum Equation). Therefore, we need some sort of model for $\overline{u_i' u_j'}$ to close the system of equations (Eqs. 1.14-1.15). This is known as a closure problem.

Similar transport equation for temperature, θ can be written for an incompressible flow (Davidson, 2022):

$$\frac{\partial \theta}{\partial t} + \frac{\partial u_i \theta}{\partial t} = \alpha \frac{\partial^2 \theta}{\partial x_i \partial x_i} \tag{1.16}$$

In a turbulent flow, instantaneous temperature can be decomposed as

$$\theta = \theta' + \overline{\theta} \tag{1.17}$$

Introducing this in Eq. 1.16, we obtain, time averaged transport equation for temperature (Davidson, 2022):

$$\frac{\partial \overline{\theta}}{\partial t} + \frac{\partial \overline{u}_i \overline{\theta}}{\partial x_i} = \alpha \frac{\partial^2 \overline{\theta}}{\partial x_i \partial x_i} - \frac{\partial \overline{u_i' \theta'}}{\partial x_i} \tag{1.18}$$

The last term in the above equation is an additional unknown term whose physical meaning is turbulent heat flux vector. This is similar to Reynolds stress terms and needs to be modelled.

The turbulence models based on RANS can be described as a set of equations needed to determine the unknown turbulent correlations that have come up due to the averaging process. RANS turbulence models of varying complexity have been developed and, with very few exceptions, can be broadly classified into eddy viscosity models and Reynolds stress models. Eddy viscosity models are based on Boussinesq assumptions (Section 3.1).

CHAPTER 2

2.1 Literature Review

Numerous studies regarding heat transfer from open channels have been conducted in the past by Moss (1976). Heat transfer involved in aeration has also been studied by Argaman (1977), and Novotny and Krenkel (1973). The phenomenon of thermal-hydraulic jump has been studied by Baddour (1990). Rahber *et al.* (2008) studied the effects of different hydraulic structures on heat transfer from the open channel and simulated these results using CFD codes. Mollik *et al.* (2017) numerically simulated heat transfer in flow through a channel using RANS turbulence models and compared the results obtained using DNS. Viti *et al.* (2018) presented a comprehensive review of the capabilities of different turbulence models for the simulation of hydraulic jumps including their ability to capture the air-water interaction. Wang and Khayat (2019) studied heat transfer involved in circular hydraulic jump. Bayon *et al.* (2019) conducted a detailed analysis of the simulation of a hydraulic jump using standard k-ε, RNG k-ε and k-ω SST models using Openfoam CFD code. Mondal *et al.* (2020) performed experiments in order to study the thermal effect on jump characteristics and correlate the variation of temperatures with several jump parameters.

Moss (1976) studied the effect of turbulence on heat dissipation in open channels. The study investigated factors that affect heat transfer from open channel flow. The effect of channel roughness was examined so as to find a means of increasing heat transfer by enhanced turbulence. The study suggested the use of artificially roughened channels as an alternative means of accomplishing an increase in evaporative cooling as a consequence of increased turbulent mixing in open channel flow and hence utilise this result for dissipation of excess industrial heat. Expressions were developed that related the heat transfer rates under several hydraulic conditions and the surface water temperature. An iterative algorithm was proposed for the determination of heat transfer. Finally, the model gave good results in the determination of heat transfer in the range of natural water temperatures and elevated temperatures found in the discharges from thermal power plants and other chemical plants.

Argaman (1977) presented a comprehensive model for temperature predictions in diffused aeration and sub-surface mechanical aeration system. During the course of the model development, expressions suggested by Novotny and Krenel (1973) were adopted to account for the heat loss by surface aeration that included heat loss due to evaporation and conduction from water droplets in aerator spray. A steady-state heat balance Equation for the aeration basin was considered. The heat balance included heat lost by long wave radiation, the heat lost by evaporation from basin surface, heat lost by conduction from the basin surface, heat lost by conduction and evaporation by aerator spray, heat gained due to solar radiation, heat gained from mechanical energy input, heat gained from biochemical reaction and heat lost by conduction through basin walls and bottom. The model developed resulted in good agreement between the predicted and measured values of temperatures for two aerated lagoons using surface aerators and diffused air.

Baddour (1990) investigated thermally stratified internal hydraulic jump in a fresh water ambient which has a temperature Equal to or greater than 4ºC. A non-linear buoyancy function was used to obtain the thermal jump solutions. A considerable difference in behaviour between thermal and density jump was revealed in a temperature range of 4ºC. The error of treating a thermal jump as a density jump is found to increase with Froude number and temperature difference and was found to decrease with ambient temperature. Thermal jump experiments were conducted for ambient water temperatures of 4ºC and 16ºC. Froude number, Reynolds number and temperature difference were identical for both the sets of the experiments. Experimental observations were comparable with the thermal jump theory. The analysis of the temperature fluctuations suggests that the ambient temperature also modified the internal mixing characteristics of the thermal jumps.

Rahber *et al.* (2008) investigated the effect of mounting various structures in an open channel and the effect of various flow rates on the natural cooling of water. The effect of hydraulic jump on the heat transfer was also studied. The hydraulic jump was obtained by incorporating structures like gates, weirs, crump weirs, stairs, and ribs. The experiments were numerically simulated using Fluent. k-ε turbulence model was used and the VOF model was used to capture the air-water interaction during the flow and hydraulic jump in simulation. The objective of this study was to decide the best factor for cooling water flowing in open channels. The experiments were conducted in a rectangular flume, 4.15 m long and 8 cm wide. Water was heated to 40º Celcius and flown through the flume and circulated through a pump. The ambient temperature was kept constant at 24ºC. The measurements were carried out using a thermometer of 0.01ºC tolerance. It was observed that more is the mixing of air and water, more is the heat transfer and hence mounting a weir or gate to create a hydraulic jump was found useful in cooling the water.

Bayon *et al.* (2015) made a detailed analysis of simulations of hydraulic jumps using RANS turbulence models namely Standard k-ε, RNG k-ε and k-ω SST. Their main goal was to determine the accuracy of the turbulence models for simulating a hydraulic jump. A 3D model was set up in OpenFOAM, the VOF approach coupled with an interface compression algorithm was used to capture the flow aeration phenomena and a structured mesh of cubic cells was employed along with a convergence analysis to ensure grid independence of the results. It was found that for the same flow conditions and the flow domain, the results differed depending upon the RANS turbulence model adopted.

Finally, it was concluded that the most accurate turbulence model for analysis of hydraulic jump is the RNG k-ε followed by both Standard k-ε and k-ω SST. However, the k-ω SST model requires much greater computational time than the standard k-ε model.

Mollik *et al.* (2017) studied seven turbulence models based on RANS Equations comparatively to justify their accuracy and suitability as compared to DNS for turbulent channel flow between two horizontal walls subsequent and heat transfer. The flow in the channel was assumed to be fully developed turbulent flow and uniform heat flux was applied at the top and bottom walls. Numerical simulations were carried out for four different Reynolds numbers. Different turbulent statistics such as mean streamline velocity, mean temperature and streamwise turbulent heat flux are calculated and compared with the data obtained by DNS. It was concluded that the turbulence models not assuming wall function can determine the near-wall flow and thermal quantities quite accurately. The low Reynolds number model k-ε can provide accurate mean flow in the near-wall region within some tolerance. High accuracy was achieved in the outer wall region. The selected k-ε model was found to be in good agreement with the DNS data for mean velocity and temperature distributions for different Reynolds and Prandtl numbers. It was further inferred that the turbulent heat flux can be accurately computed by the low Reynolds number model.

Viti *et al.* (2018) in their review paper presented a detailed study of several numerical simulations of hydraulic jumps carried out in the last two decades. The main characteristics of the most common CFD approach, namely, the Eulerian approach - RANS, Large Eddy Simulation (LES), Direct Numerical Simulation (DNS), hybrid RANS-LES such as DES (detached eddy simulation) and Lagrangian approach – Smooth particle hydrodynamics (SPH) were discussed. It was observed that the RANS modelling in several cases was able to provide accurate results for the mean flow variables. Among the RANS models, while the RNG k-ε model performed the best to simulate the hydraulic jump with respect to all the four parameters -sequent depth relations, roller length, efficiency and mean free surface considered together, the standard k-ε model provided more accurate results in terms of roller length and the free surface. The high fidelity models such as LES and DES reproduced turbulent quantities of the hydraulic jump with good accuracy. Considering the computational resources currently available, RANS models based on simulations of the hydraulic jump are of greater relevance for hydraulic engineering applications.

Wang and Khayat (2019) studied the hydrodynamics and heat transfer of impinging jet flow and a circular hydraulic jump. The influence of heat transfer on the axi-symmetrical spreading and structure of the hydraulic jump of a liquid impinging on a circular heated disk was examined theoretically. The disk was maintained at either constant heat flux or constant temperature. It was assumed that the liquid viscosity and surface tension are dependent on temperature. The viscosity was taken to follow the VTF model and surface tension was assumed to decrease linearly with temperature. Karman-Pohlhausen's (K-P) integral approach is adopted to capture the flow and heat transfer in the region upstream of the jump. Across the jump, an energy balance was developed to simultaneously determine the hydraulic and thermal jumps, downstream flow and thermal fields. The jump was found to move outwards (downstream) with the increasing higher wall temperature and heat flux. The jump height decreased with enhanced thermal input at the wall.

Mondal *et al.* (2020) conducted hydraulic jump experiments by increasing the temperature of water from 32-42ºC. The objective of the research was to study the thermal effect on the jump characteristics and correlate the temperature variation with the basic parameters of the hydraulic jump. Measurements of sequent depths, specific energy, velocity, and post-hydraulic jump depths were conducted. It was observed that the difference in Froude numbers pre and post-jump has increased with the increase in water temperature. Reynold’s number also increases with the increase in water temperature for the same flow conditions.

CHAPTER 3

3.1 Boussinesq Assumption:

Analogous to the co-efficient of viscosity for laminar flow, J. Boussinesq assumed a mixing co-efficient μ_t for the Reynolds stress terms (Eq. 1.14) by invoking

$$\tau_t = -\rho \overline{u_i' u_j'} = \mu_t \left(\frac{\partial \overline{u}_i}{\partial x_j} + \frac{\partial \overline{u}_j}{\partial x_i} \right) = \rho \nu_t \left(\frac{\partial \overline{u}_i}{\partial x_j} + \frac{\partial \overline{u}_j}{\partial x_i} \right) \tag{3.1}$$

So we can write,

$$\overline{u_i' u_j'} = -\nu_t \left(\frac{\partial \overline{u}_i}{\partial x_j} + \frac{\partial \overline{u}_j}{\partial x_i} \right) \tag{3.2}$$

But this equation is not valid upon contraction (as the right-hand side of this equation becomes zero due to the continuity equation but the left-hand side may not be zero). So the equation is re-written as

$$\overline{u_i' u_j'} = -\nu_t \left(\frac{\partial \overline{u}_i}{\partial x_j} + \frac{\partial \overline{u}_j}{\partial x_i} \right) + \frac{1}{3} \delta_{ij} \overline{u_k' u_k'} \tag{3.3}$$

noting that $k = \frac{1}{2} \overline{u_k' u_k'}$, the above equation can be modified as

$$\overline{u_i' u_j'} = -\nu_t \left(\frac{\partial \overline{u}_i}{\partial x_j} + \frac{\partial \overline{u}_j}{\partial x_i} \right) + \frac{2}{3} \delta_{ij} k \tag{3.4}$$

which is now valid upon contraction ($\overline{u_i' u_j'} = 2k$). Eq. 3.3 is a result of the Boussinesq assumption.

Considering Boussinesq assumption, Eq. 1.14 is now written as

$$\frac{\partial \overline{u}_i \overline{u}_j}{\partial x_j} = -\frac{1}{\rho} \frac{\partial \overline{p}}{\partial x_i} + \frac{\partial}{\partial x_j} \left(\left(\nu + \nu_t \right) \left(\frac{\partial \overline{u}_i}{\partial x_j} + \frac{\partial \overline{u}_j}{\partial x_i} \right) \right) \tag{3.5}$$

The term ν_t appearing in Eqs. 3.1-3.2 is known as *eddy viscosity*. The difficulty in using Eq. 3.2 is that ν_t is an additional unknown because, unlike ν which is a property of the fluid considered, ν_t is a quantity derived from the random fluctuations in the turbulent flow. There are ways in which ν_t or μ_t are modelled in terms of other parameters that in turn are expressed with the time-averaged quantities. These models are called *eddy viscosity* models. There are a number of eddy viscosity models but only the two-Equation, k-ε models have been discussed in the following sections.

Boussinesq's assumption can also be extended to model the turbulent heat flux appearing in Eq. 1.18 as follows:

$$\overline{u_i'\theta'} = -\alpha_t \frac{\partial \overline{\theta}}{\partial x_i} \tag{3.6}$$

where α_t denotes turbulent thermal diffusivity given by

$$\alpha_t = \frac{\nu_t}{\mathrm{Pr}_t}$$

where Pr_t is a turbulent Prandtl number which is usually set to $0.7 < \mathrm{Pr}_t < 0.9$.

3.2 k-ε Turbulence Models:

3.2.1 Standard k-ε Turbulence Model:

3.2.1.1 Overview:

Proposed by Launder and Spalding (1983), standard k-ε is a RANS-based model that employs Boussinesq's hypothesis to calculate the value of "μ_t" - turbulent viscosity as a function of "k" – turbulent kinetic energy and "ε"-turbulence dissipation rate. This model provides two additional transport Equations for k and ε apart from the momentum and continuity equation. The transport Equation for ε is semi-empirical while the transport equation for k is derived from the exact transport equation. While deriving the k- ε model, it is assumed that the flow is fully turbulent and it is a high Reynolds no. model. Due to its robustness, economy and reasonable accuracy for a wide range of turbulent flow, the k-ε model has gained huge popularity in industrial flow and heat transfer simulations.

3.2.1.2 Modelling the turbulent viscosity:

The turbulent (eddy) viscosity is computed in terms of k and ε as follows:

$$\mu_t = \rho C_\mu \frac{k^2}{\varepsilon} \tag{3.7}$$

where C_μ is a constant.

3.2.1.3 Transport Equations for standard k- ε model:

The turbulent kinetic energy, *k* and the turbulence dissipation rate *ε* are obtained by solving the following transport Equations:

$$\frac{\partial}{\partial t}(\rho k) + \frac{\partial}{\partial x_i}(\rho k u_i) = \frac{\partial}{\partial x_j}\left[\left(\mu + \frac{\mu_t}{\sigma_k}\right)\frac{\partial k}{\partial x_j}\right] + G_k + G_b - \rho\varepsilon - Y_M + S_k \tag{3.8}$$

$$\frac{\partial}{\partial t}(\rho\varepsilon)+\frac{\partial}{\partial x_i}\left(\rho\varepsilon u_i\right)=\frac{\partial}{\partial x_j}\left[\left(\mu+\frac{\mu_t}{\sigma_\varepsilon}\right)\frac{\partial\varepsilon}{\partial x_j}\right]+C_{1\varepsilon}\frac{\varepsilon}{k}\left(G_k+C_{3\varepsilon}G_b\right)-C_{2\varepsilon}\rho\frac{\varepsilon^2}{k}+S_\varepsilon \qquad (3.9)$$

where,
G_k represents the generation of turbulence kinetic energy due to mean velocity gradients

G_b represents the generation of turbulence kinetic energy due to buoyancy effects.

Y_M represents the contribution of fluctuating dilatation in compressible turbulence in the overall dissipation rate.

S_k and S_ε are user-defined source terms.

$C_{1\varepsilon}$, $C_{2\varepsilon}$, and $C_{3\varepsilon}$ are constants and σ_k, and σ_ε are turbulent Prandtl numbers for k and ε respectively.

3.2.1.4 Model constants for Standard k-ε turbulence model:

The constants $C_{1\varepsilon}$, $C_{2\varepsilon}$, σ_k and σ_k in the above transport equations of standard k-ε model and C_μ in eddy viscosity Equation(Eq. 3.7) model have the following default values Launder and Spalding (1983):

$$C_{1\varepsilon} = 1.44,\ C_{2\varepsilon} = 1.92,\ C_\mu = 0.09,\ \ \sigma_k = 1.0,\ \ \sigma_\varepsilon = 1.3$$

These default values have been obtained from experiments with air and water for fundamental turbulent shear flows and isotropic grid turbulence. They have been found to work fairly well for wide ranges of wall-bounded and free shear flows.

The value for $C_{3\varepsilon}$ depends upon whether the buoyancy effects on turbulence dissipation ε are included or not. In Ansys Fluent, the buoyancy effect is neglected by setting G_b to zero, by default. As such, the necessity of $C_{3\varepsilon}$ is eliminated. However, one can opt to consider the buoyancy effects on ε in Ansys Fluent and in that case, $C_{3\varepsilon}$ is not specified but rather calculated using the following equation:

$$C_{3\varepsilon} = \tanh\left|\frac{\upsilon}{u}\right| \qquad (3.10)$$

where υ is the component of flow velocity parallel to the gravitational vector and u is the component of the flow velocity perpendicular to the gravitational vector. As can be observed, $C_{3\varepsilon}$ will become 1 for the buoyant shear layer for which the main flow direction is aligned with the direction of gravity. For the buoyant shear layers that are perpendicular to the gravitational vector, $C_{3\varepsilon}$ will become zero.

3.2.2 RNG k-ε turbulence model:

3.2.2.1 Overview:

This model is very similar in form to the standard k-ε with certain refinements that are achieved using statistical techniques named Renormalisation Group Theory (RNG) (Yakhot and Orszag, 1992) applied to Navier Stokes equations rendering the RNG k-ε model more accurate and reliable for a wider class of flow than the standard k-ε model. The RNG model has an additional term in its ε equation that significantly improves the accuracy for rapidly strained flows. As compared to the standard k-ε model that uses either specified or user-specified turbulent Prandtl numbers, the RNG model provides an analytical formula for turbulent Prandtl numbers. While the standard k-ε model is a high Reynolds number model, the RNG model accounts for low Reynolds number effects depending upon appropriate near-wall region treatment.

3.2.2.2 Transport Equations for the RNG k-ε model:

The transport equations for k and ε in the RNG k-ε model are as follows:

$$\frac{\partial}{\partial t}(\rho k)+\frac{\partial}{\partial x_i}\left(\rho k u_i\right)=\frac{\partial}{\partial x_j}\left[\alpha_k \mu_{eff}\frac{\partial k}{\partial x_j}\right]+G_k+G_b-\rho\varepsilon-Y_M+S_k \tag{3.11}$$

$$\frac{\partial}{\partial t}(\rho\varepsilon)+\frac{\partial}{\partial x_i}\left(\rho\varepsilon u_i\right)=\frac{\partial}{\partial x_j}\left[\alpha_\varepsilon \mu_{eff}\frac{\partial \varepsilon}{\partial x_j}\right]+C_{1\varepsilon}\frac{\varepsilon}{k}\left(G_k+C_{3\varepsilon}G_b\right)-C_{2\varepsilon}\rho\frac{\varepsilon^2}{k}-R_\varepsilon+S_\varepsilon \tag{3.12}$$

where,
G_k represents the generation of turbulence kinetic energy due to mean velocity gradients

G_b represents the generation of turbulence kinetic energy due to buoyancy effects.

Y_M represents the contribution of fluctuating dilatation in compressible turbulence in the overall dissipation rate.

S_k and S_ε are user-defined source terms.

$C_{1\varepsilon}$, $C_{2\varepsilon}$, and $C_{3\varepsilon}$ are constants and α_k, and α_ε are inverse effective Prandtl numbers for k and ε respectively.

3.2.2.3 Modelling Effective Viscosity:

RNG theory provides a differential equation for turbulent viscosity:

$$d\left(\frac{\rho^2 k}{\sqrt{\varepsilon\mu}}\right) = 1.72 \frac{\hat{v}}{\sqrt{\hat{v}^3 - 1 + C_v}} d\hat{v} \tag{3.13}$$

where

$\hat{v} = \mu_{eff} / \mu$

$C_v \approx 100$

Eq. 3.13 is integrated to obtain effective viscosity whose transport accurately varies with the effective Reynolds number (or eddy scale), allowing the model to handle low Reynolds number and near-wall flows better than the standard k-ε model. In high Reynolds number limit, Eq. 3.7 gives

$$\mu_t = \rho C_\mu \frac{k^2}{\varepsilon} \tag{3.14}$$

with C_μ=0.0845, derived using RNG theory.

3.2.2.4 Calculating the Inverse Effective Prandtl Numbers

The inverse effective Prandtl numbers α_k and α_ε are computed using the following equations as derived from RNG theory:

$$\left|\frac{\alpha - 1.3929}{\alpha_0 - 1.3929}\right|^{0.6321} \left|\frac{\alpha + 2.3929}{\alpha_0 + 2.3929}\right|^{0.3679} = \frac{\mu_{mol}}{\mu_{eff}} \tag{3.15}$$

where α_o=1.0. In the high Reynolds number limit ($\mu_{mol} / \mu_{eff} \ll 1$), $\alpha_k = \alpha_\varepsilon \approx 1.393$.

3.2.2.5 The R$_\varepsilon$ term in the ε Equation

The transport equation for turbulence dissipation rate, ε, has one additional term given by

$$R_\varepsilon = \frac{C_\mu \rho \eta^3 \left(1-\eta/\eta_0\right)}{1+\beta\eta^3}\frac{\varepsilon^2}{k} \tag{3.16}$$

where

$\eta = \dfrac{Sk}{\varepsilon}$, $\eta_0 = 4.38$, $\beta = 0.012$.

S is defined asthe modulus of mean rate of strain tensor, calculated as

$$S = \sqrt{2S_{ij}S_{ij}} \tag{3.17}$$

The effects of this term in the RNG transport equation for ε can be seen more clearly by rearranging Eq. 3.12. Replacing Eq. 3.16 and merging the third and the fourth terms on the right-hand side of Eq. 3.12, the resultant transport equation for ε can be written as

$$\frac{\partial}{\partial t}(\rho\varepsilon) + \frac{\partial}{\partial x_i}\left(\rho\varepsilon u_i\right) = \frac{\partial}{\partial x_j}\left[\alpha_\varepsilon \mu_{eff}\frac{\partial \varepsilon}{\partial x_j}\right] + C_{1\varepsilon}\frac{\varepsilon}{k}\left(G_k + C_{3\varepsilon}G_b\right) - C^*_{2\varepsilon}\rho\frac{\varepsilon^2}{k} \tag{3.18}$$

where $C^*_{2\varepsilon}$ is given by

$$C^*_{2\varepsilon} = C_{2\varepsilon} + \frac{C_\mu \eta^3 \left(1-\eta/\eta_0\right)}{1+\beta\eta^3} \tag{3.19}$$

It can be observed that in the regions where $\eta < \eta_0$, the R term has a positive effect and $C^*_{2\varepsilon}$ becomes larger than $C_{2\varepsilon}$. Also for $\eta \approx 3.0$, $C^*_{2\varepsilon} \approx 2.0$ which is comparable with the value for $C^*_{2\varepsilon}$ in the standard k-ε model. Thus for weakly to moderately strained flows, the RNG model tends to give results largely comparable to the standard k-ε models.

In the regions of large strain rate ($\eta > \eta_0$), the R term makes a negative contribution so that the value of $C^*_{2\varepsilon}$ becomes less than $C_{2\varepsilon}$. Thus in the RNG model, smaller destruction of ε augments ε which in turn reduces k and eventually the effective viscosity. Therefore, the RNG model is more responsive to the effects of rapid strain and streamlined curvature than the k-ε model thus explaining the superiority of the RNG k-ε model over the standard k-ε model for certain classes of flow.

3.2.2.6 Model Constants

The constants $C_{1\varepsilon}$ and $C_{2\varepsilon}$ used in Eq. 3.12 have values derived from RNG theory and the default values are

$$C_{1\varepsilon} = 1.42,\ C_{2\varepsilon} = 1.68$$

3.2.3 Realizable k-ε Turbulence model

3.2.3.1 Overview

“Realizable” means that the model satisfies certain mathematical constraints on the Reynolds stresses. consistent with the physics of turbulent flows. Neither the standard k-ε model nor the RNG k-ε model is realizable. The Realizable k-ε model (Shih et al., 1995) differs from the standard k-ε model in the formulation of turbulent viscosity and in the derivation of a new transport Equation for ε term in terms of transport of the mean square vorticity fluctuations. The eddy viscosity formula involving the constant C_μ in the standard k-ε model is now a variable in the Realizable k-ε model as proposed by Reynolds. To understand the significance of the variable C_μ, let us consider combining the Boussinesq relationship (Eq. 3.4) and the eddy viscosity definition to obtain the following Equation for normal Reynolds stress in an incompressible strained mean flow:

$$\overline{u^2} = \frac{2}{3}k - 2\nu_t \frac{\partial U}{\partial x} \tag{3.20}$$

where U is the time averaged velocity of the mean strained flow. Now, replacing ν_t with μ_t/ρ and using Eq. 3.7 , one obtains the following expression for $\overline{u^2}$:

$$\overline{u^2} = \frac{2}{3}k - 2\frac{C_\mu k^2}{\varepsilon}\frac{\partial U}{\partial x} \tag{3.21}$$

Normal Reynolds stress, $\overline{u^2}$, by definition is positive but as can be seen from the above Equation, $\overline{u^2}$ becomes negative i.e. “non-realizable”, when the strain is large enough to satisfy

$$\frac{k}{\varepsilon}\frac{\partial U}{\partial x} > \frac{1}{3C_\mu} \approx 3.7 \tag{3.22}$$

Therefore, the most straightforward way to ensure the reliability (or positivity of the normal stresses) is to make the *Cμ* variable i.e. expressing it as some function of mean flow (mean deformation) and the turbulence (k, ε).

It is found that both the realizable k-ε model and the RNG k-ε model have substantial improvements over the standard k-ε model where the flow features include streamlined curvature, vortices and rotation. Besides, initial studies have shown that the realizable k-ε model provides the best performance of all the k-ε models for several validations of separated flows and flows with complex secondary flow features.

One limitation of the Realizable k-ε model is that it produces non-physical turbulent viscosities in situations when the computational domain contains both the rotating and stationary fluid zones (e.g. multiple reference frames).

3.2.3.2 Transport Equations for the Realizable k-ε Model

The modelled transport Equations for k and ε are

$$\frac{\partial}{\partial t}(\rho k)+\frac{\partial}{\partial x_i}\left(\rho k u_i\right)=\frac{\partial}{\partial x_j}\left[\left(\mu+\frac{\mu_t}{\sigma_k}\right)\frac{\partial k}{\partial x_j}\right]+G_k+G_b-\rho\varepsilon-Y_M+S_k \qquad (3.23)$$

$$\frac{\partial}{\partial t}(\rho\varepsilon)+\frac{\partial}{\partial x_i}\left(\rho\varepsilon u_i\right)=\frac{\partial}{\partial x_j}\left[\left(\mu+\frac{\mu_t}{\sigma_k}\right)\frac{\partial\varepsilon}{\partial x_j}\right]+\rho C_1 S\varepsilon-\rho C_2\frac{\varepsilon^2}{k+\sqrt{\nu\varepsilon}}+C_{1\varepsilon}\frac{\varepsilon}{k}C_{3\varepsilon}G_b+S_\varepsilon \qquad (3.24)$$

where

$$C_1=\max\left[0.43,\frac{\eta}{\eta+5}\right], \qquad \eta=S\frac{k}{\varepsilon}, \qquad S=\sqrt{2S_{ij}S_{ij}} \qquad (3.25)$$

S is the modulus of the mean rate of the strain tensor.

In the above transport equations,
G_k represents the generation of turbulence kinetic energy due to mean velocity gradients
G_b represents the generation of turbulence kinetic energy due to buoyancy effects.
Y_M represents the contribution of fluctuating dilatation in compressible turbulence in the overall dissipation rate. S_k and S_ε are user-defined source terms.
C_1, $C_{1\varepsilon}$, C_2, *and* $C_{3\varepsilon}$ are constants and α_k, α_ε are inverse effective Prandtl numbers for k and ε respectively.

Even though the transport equation for k is similar to the other k-ε models, except few changes in the constants, there are notable differences in the ε transport equation. The production term in the ε transport Equation does not involve the production of k i.e it does not contain the same G_k term as in other k-ε models. It is believed that the present form represents the spectral energy transfer better. Another desirable feature is that the destruction term in the ε transport Equation does not have any singularity as compared to

Eqs. 3.9 and 3.12. As a result, even if k vanishes or becomes less than zero. the denominator never vanishes.

3.2.3.3 Modelling the Turbulent Viscosity

As in other k-ε models, the eddy viscosity is computed from

$$\mu_t = \rho C_\mu \frac{k^2}{\varepsilon} \tag{3.26}$$

In realizable k-ε model , the C_μ is not constant , rather it is computed as

$$C_\mu = \frac{1}{A_0 + A_s \frac{kU^*}{\varepsilon}} \tag{3.20}$$

where

$$U^* \equiv \sqrt{S_{ij}S_{ij} + \Omega_{ij}\Omega_{ij}} \tag{3.27}$$

and

$$\Omega_{ij} = \Omega_{ij} - 2\varepsilon_{ij}\omega_k \tag{3.28}$$

$$\Omega_{ij} = \overline{\Omega_{ij}} - \varepsilon_{ijk}\omega_k$$

where $\overline{\Omega_{ij}}$ is the mean rate-of-rotation tensor viewed in a rotating reference frame with the angular velocity ω_k . The model constants A_0 and A_s are given by

$A_0 = 4.04$, $A_s = \sqrt{6}\cos\phi$

where

$$\phi = \frac{1}{3}\cos^{-1}(\sqrt{6}W)\,,\quad W = \frac{S_{ij}S_{jk}S_{ki}}{S^3}\,,\quad S = \sqrt{S_{ij}S_{ij}}\,,\quad S_{ij} = \frac{1}{2}\left(\frac{\partial u_j}{\partial x_i} + \frac{\partial u_i}{\partial x_j}\right) \tag{3.29}$$

As can be seen, C_μ is a function of mean strain and rotation rates, the angular velocity of the system rotation and the turbulence fields (k and ε). It can be shown that for an inertial sublayer in an equilibrium boundary layer, C_μ equals 0.09.

3.2.3.4 Model constants

The model constants $C_{1\varepsilon}$, C_2, σ_k and σ_ε and sigma have the following values:

$$C_{1\varepsilon} = 1.44,\ C_2 = 1.9,\ \sigma_k = 1.0,\ \sigma_\varepsilon = 1.2$$

3.2.4 Modelling Turbulent Production in the k-ε Models

The term G_k appearing in the transport Equations for k and ε, represents production of turbulence kinetic energy and is modelled identically for all the k-ε turbulence models as

$$G_k = -\rho \overline{u_i' u_j'} \frac{\partial u_j}{\partial x_i} \tag{3.30}$$

G_k can be evaluated in a manner consistent with the Boussinesq hypothesis

$$G_k = \mu_t S^2 \tag{3.31}$$

where S is the modulus of the mean rate-of-strain tensor and is defined as

$$S \equiv \sqrt{2 S_{ij} S_{ij}} \tag{3.32}$$

3.2.5 Effects of Buoyancy on Turbulence in k-ε Models

In presence of a non-zero-gravity field and temperature gradient simultaneously, the k-ε models account for the generation of k due to buoyancy. In the transport Equations, this generation of turbulence kinetic energy is represented by G_b and is given by

$$G_b = \beta g_i \frac{\mu_t}{\Pr_t} \frac{\partial \rho}{\partial x_i} \tag{3.33}$$

where $\Pr_t$ is the turbulent Prandtl number for energy and g_i is the component of the gravitational vector in the i^{th} direction. For the standard and realizable k- modes, the default $\Pr_t$ is 0.85. In the case of the RNG k-model, $\Pr_t = 1/\alpha$, where α is given by Eq. 3.14 with $\alpha_0 = 1/\Pr = k/\mu C_p$. The co-efficient of thermal expansion. Beta is defined as

$$\beta = -\frac{1}{\rho}\left(\frac{\partial p}{\partial T}\right)_p \tag{3.34}$$

For ideal gases, Equation (3.33) reduces to

$$G_b = -g_i \frac{\mu_t}{\mathrm{Pr}_t}\frac{\partial p}{\partial x_i} \tag{3.35}$$

3.2.6 Effects of Compressibility on Turbulence in k-ε Models

For, high Mach-number flows, compressibility affects turbulence through so-called “dilatation dissipation”, which is neglected for incompressible flows. Neglecting the dilatation dissipation fails to predict the observed decrease in spreading rate with increasing Mach number for compressible mixing and other free shear layers. To account for these effects in k-ε models, the dilatation dissipation term, Y_M is included in the k-ε Equation. This term is modelled according to a proposal by Sarkar and Lakshmanan (1990):

$$Y_M = 2\rho\varepsilon M_t^2 \tag{3.36}$$

where M_t is turbulent Mach number, defined as

$$M_t = \sqrt{\frac{k}{a^2}} \tag{3.37}$$

where $a\left(\equiv \sqrt{\gamma RT}\right)$ is the speed of sound.

This compressibility modification always takes effect when the compressible form of the ideal gas law is used. *T* in Eqs. 3.34 and 3.37 represents temperature on an absolute scale

3.3 Modelling a Multi-Phase flow

3.3.1 Overview

Open channel flow is a multiphase flow as the dynamics of two fluids are involved-the water and atmosphere above the water-free surface. As a consequence, the free surface is an interaction of these two phases and hence proper evaluation of the free surface properly becomes essential while simulating an open channel flow. During a hydraulic jump, there is vigorous mixing of water and air and when one studies the heat interaction between these two fluids during the hydraulic jump, the modelling of the interaction between these two phases becomes an essential part of the simulation. A large number of multiphase models are present in CFD.

In multiphase flow, a phase can be defined as an identifiable class of material that has a particular inertial response to and interaction with the flow and the potential field in which it is immersed. Multiphase flow regimes can be grouped into four categories: gas-liquid or liquid-liquid flows; gas-solid flows; and three-phase flows. Open channel flow falls under the gas-liquid multiphase flow regime.

3.3.2 Approaches to Multiphase Modelling

There are two approaches for the numerical calculation of multiphase flows in CFD – The Euler-Lagrange approach and the Euler-Euler approach.

3.3.2.1 The Euler-Euler Approach

In the Euler-Euler approach, the different phases are treated mathematically as interpenetrating continua. Since the volume of a phase cannot be occupied by the other phases, the concept of volume fraction (of individual phase) is introduced. These volume fractions are assumed to be continuous functions of space and time and their sum is Equal to one. Conservation Equations for each phase are derived to obtain a set of Equations, which have a similar structure for all phases. These Equations are closed by providing constitutive relations that are obtained from empirical information, or, in the case of granular flows, by application of kinetic theory. Three different Euler-Euler multiphase models available in Ansys fluent are: the volume of fluid (VOF) model, the mixture model and the Eulerian model. VOF model can be suitably used for free surface flows, for simulating the motion of liquid after a dam break, and for steady and transient tracking of any liquid-gas interface.

3.3.2.2 VOF (Volume of Fluid) model

3.3.2.2.1 Overview

The VOF model can model two or more immiscible fluids by solving a single set of momentum Equations and tracking the volume fraction of each of the fluids throughout the domain. Typical applications include the prediction of the jet breakup, motion of a large bubble in a liquid, motion of liquid after dam break problem, free-surface flows and steady and transient tracking of any liquid-gas interface.

3.3.2.2.2 Steady-State and Transient VOF Calculations

The VOF formulation (Hirt and Nichols, 1981) is generally sued to compute a time-dependent solution, but for problems in which one is concerned only with a steady-state solution, it is possible to perform a steady-state calculation. A steady-state VOF calculation is sensible only when the solution is independent of the initial conditions and there are distinct inflow boundaries for the individual phases. For example, the flow of water in a channel with a region of air on top and a separate air inlet can be solved with the steady-state formulation.

In VOF formulation, for each additional phase that one introduces, a variable is introduced: the volume fraction of the phase in the computational cell. In each cell (control volume), the volume fractions of all phases sum up to unity. The fields for all the variables and properties are shared by the phases and represent volume-averaged values. as long as the volume fraction of each of the phases is known at each location. Thus the variables and the properties in any given cell are either purely representative of one of the phases, or representative of a mixture of the phases, depending upon the volume fraction values. In other words, if the qth fluid's volume fraction in the cell is denoted as α_q then the following three conditions are possible:

- $\alpha_q = 0$; The cell is empty (of the qth fluid)
- $\alpha_q = 1$; The cell is full (of the qth fluid)
- $0 < \alpha_q < 1$; The cell contains the interface between the qth fluid and one or more other fluids.

Based on the local value of α_q, the appropriate properties and variables will be assigned to each control volume within the domain

3.3.2.2.3 Volume Fraction Equation

The tracking of the interface(s) between the phases is accomplished by the solution of a continuity Equation for the volume fraction of one (or more) of the phases. For the qth phase, this Equation has the following form:

$$\frac{1}{\rho_q}\left[\frac{\partial}{\partial t}\left(\alpha_q\rho_q\right)+\nabla.\left(\alpha_q\rho_q\vec{\upsilon}_q\right)=S_{\alpha q}+\sum_{p=1}^{n}\left(\dot{m}_{pq}-\dot{m}_{qp}\right)\right] \tag{3.38}$$

where $\dot{m}_{qp}$ is the mass transfer from phase q to phase p and $\dot{m}_{pq}$ is the mass transfer from phase p to phase q. By default, the source term on the right-hand side of Eq. 3.38, $S_{\alpha q}$ is zero but can any user-defined mass source for each phase can be specified.

The volume fraction is not solved for the primary phase. The primary phase-phase volume fraction is computed based on the following constraint:

$$\sum_{q=1}^{n}\alpha_q = 1 \tag{3.39}$$

The volume fraction Equation may be solved either through implicit or explicit time discretisation.

3.3.2.2.4 The implicit Scheme

An implicit scheme is used for time discretisation. Standard finite-difference interpolation schemes, QUICK, Second-Order Upwind and First-Order Upwind and Modified HRIC schemes are used to obtain the face fluxes for all cells, including those near the interface.

$$\frac{\alpha_q^{n+1}\rho_q^{n+1}-\alpha_q^{n}\rho_q^{n}}{\Delta t}V+\sum\left(\rho_q^{n+1}U_f^{n+1}\alpha_{q,f}^{n+1}\right)=\left[S_{\alpha q}+\sum_{p=1}^{n}\left(\dot{m}_{pq}-\dot{m}_{qp}\right)\right]V \qquad (3.40)$$

where $n+1$ = index for new (current) time step

n = index for new previous time step

$\alpha_{q,f}$ = face value of the q_{th} volume fraction.

V = volume of cell

U_f = volume flux through the face, based on normal velocity.

This Equation requires the volume fraction values at the current time step, a standard scalar transport Equation is solved iteratively for each of the secondary-phase volume fractions at each time step. The implicit scheme can be used for both time-dependent and steady-state calculations.

3.3.2.2.5 The Explicit Scheme

In the explicit approach, standard finite difference interpolation schemes are applied to the volume fraction values that were computed at the previous time step.

$$\frac{\alpha_q^{n+1}\rho_q^{n+1}-\alpha_q^{n}\rho_q^{n}}{\Delta t}V+\sum_f\left(\rho_q^{n}U_f^{n}\alpha_{q,f}^{n}\right)=\left[S_{\alpha q}+\sum_{p=1}^{n}\left(\dot{m}_{pq}-\dot{m}_{qp}\right)\right]V \qquad (3.41)$$

where $n+1$ = index for new (current) time step

n = index for new previous time step

$\alpha_{q,f}$ = face value of the q_{th} volume fraction, computed from the first or second order upwind, QUICK, modified HRIC, or CICSM scheme

V = volume of cell

U_f = volume flux through the face, based on normal velocity.

When the explicit scheme is used for time discretisation, the face fluxes can be interpolated either using interface reconstruction or using a finite volume discretisation scheme. The reconstruction-based schemes are Geo-Reconstruct and Donor-Acceptor. The discretisation schemes available with explicit schemes for VOF are first-order Upwind, Second-Order Upwind, CICSAM, Modified HRIC and QUICK.

3.4 Modelling Heat Transfer

3.4.1 The Generalised Energy Equation

The generalised energy Equation that many CFD codes like Ansys Fluent solves are as follows:

$$\frac{\partial}{\partial t}(\rho E)+\nabla.\left(\vec{u}\left(\rho E+p\right)\right)=\nabla.\left(k_{eff}\nabla T-\sum_j h_j\vec{J}_j+\left(\overline{\overline{\tau}}_{eff}.\vec{u}\right)\right)+S_h \qquad (3.42)$$

where k_{eff} is the effective conductivity which is defined as $k+k_t$, where k_t is the turbulent thermal conductivity, defined according to the turbulence model being used. $\vec{J}_j$ is the diffusion flux of species j. The first three terms on the right-hand side of Eq. 3.42 represent energy transfer due to conduction, species diffusion and viscous dissipation respectively. S_h includes the heat of chemical reaction and any other volumetric heat source that may be defined by the user.

In Eq. 3.42

$$E=h-\frac{p}{\rho}+\frac{v^2}{2} \qquad (3.43)$$

where sensible enthalpy h is defined for ideal gases as

$$h=\sum_j Y_j h_j \qquad (3.44)$$

and for incompressible flows as

$$h=\sum_j Y_j h_j+\frac{p}{\rho} \qquad (3.45)$$

In Equations 3.44 and 3.45 , Y_j is the mass fraction of species j and

$$h_j = \int_{T_{ref}}^{T} c_{p,j} dT \tag{3.46}$$

where T_{ref} is 298.15 K.

3.4.2 Natural Convection and Buoyancy-Driven Flows theory

When heat is added to a fluid and the fluid density varies with the temperature, flows can be induced due to the force of gravity acting on the density variations. Such buoyancy-driven flows are termed natural-convection (or mixed-convection) flows and can be modelled accordingly in Ansys fluent.

The importance of buoyancy forces in a mixed convection flow can be measured by the ratio of the Grashof and Reynolds numbers:

$$\frac{Gr}{\mathrm{Re}^2} = \frac{g\beta\Delta TL}{\nu^2} \tag{3.47}$$

When this number approaches or exceeds unity, one should expect strong buoyancy contributions of the flow. Conversely, if it is very small, buoyancy forces may be ignored. In pure natural convection, the strength of the buoyancy-induced flow is measured by the Rayleigh number:

$$Ra = \frac{g\beta\Delta TL^3\rho}{\mu\alpha} \tag{3.48}$$

where β is the thermal expansion co-efficient defined as

$$\beta = -\frac{1}{\rho}\left(\frac{\partial\rho}{\partial T}\right)_p \tag{3.49}$$

and α is the thermal diffusivity:

$$\alpha = \frac{k}{\rho c_p} \tag{3.50}$$

Rayleigh numbers less than 10^8 indicate a buoyancy–induced laminar flow, with the transition to turbulence occurring over the range of $10^8 < \mathrm{Ra} < 10^{10}$.

3.4.2.1 Modelling Convective heat transfer in k-ε Turbulence Models

Turbulent heat and mass transport are modelled using the concept of Reynolds' analogy to the turbulent momentum transfer. The modelled energy equation is thus given by the following:

$$\frac{\partial}{\partial t}(\rho E)+\frac{\partial}{\partial x_i}\left[u_i\left(\rho E+p\right)\right]=\frac{\partial}{\partial x_j}\left(k_{eff}\frac{\partial T}{\partial x_j}+u_i\left(\tau_{ij}\right)_{eff}\right)+S_h \qquad (3.51)$$

where E is the total energy, k_{eff} is the effective thermal conductivity and $\left(\tau_{ij}\right)_{eff}$ is the deviatoric stress tensor and is defined as

$$\left(\tau_{ij}\right)_{eff}=\mu_{eff}\left(\frac{\partial u_j}{\partial x_i}+\frac{\partial u_i}{\partial x_j}\right)-\frac{2}{3}\mu_{eff}\frac{\partial u_k}{\partial x_k}\delta_{ij} \qquad (3.52)$$

For the standard and the realizable k-ε model, the effective thermal conductivity is calculated as:

$$k_{eff}=k+\frac{c_p\mu_t}{\mathrm{Pr}_t} \qquad (3.53)$$

where *k*, in this case, is the thermal conductivity. The default value of the turbulent Prandtl number is 0.85

For the RNG k-ε model, the effective thermal conductivity is

$$k_{eff}=\alpha c_p\mu_{eff} \qquad (3.54)$$

where α is calculated from Eq. 3.15 and $\alpha_0=1/\mathrm{Pr}=k/\mu c_p$.

CHAPTER 4

4.1 Objectives

The objectives of this study are to simulate hydraulic jump in a two-dimensional rectangular flume and to observe the effects of the hydraulic jump on thermal properties – temperature, specific enthalpy and specific entropy of the flow across a section downstream the jump. Hydraulic jump is characterised by a highly turbulent flow with macro-scale vortices and involves a large amount of kinetic energy dissipation and intense mixing and aeration. The primary objective of the present study is to simulate a hydraulic jump to observe its effect on heat transfer from the water to the ambient for different ambient temperatures.

In the post-processing of the simulations, the following attempts have been made:

- To observe and calculate the decrease in the average temperature, specific enthalpy, and specific entropy at a section downstream of the hydraulic jump as compared to a section close to the inlet.
- Compare these decreases in temperature, specific enthalpy and specific entropy brought about by the hydraulic jump with respect to the decrease in the same quantities caused by only convection and conduction without any hydraulic jump.

4.2 Methodology

The CFD code Ansys Fluent was used to simulate the hydraulic jumps in a two-dimensional rectangular flume. Six simulations were performed with water at 40ºC flowing inside the flume in each of the simulation. The lowest ambient temperature considered was 10ºC and was increased by 5ºC for every consecutive simulation. The highest ambient temperature was 35ºC for the final simulation. Also, separate simulations for the flow without hydraulic jump were carried out for each of the ambient temperatures, to compare the effect of heat transfer with hydraulic jump and convection and with only convection. The entire methodology is represented in a nutshell in Fig. 4.1. The methodology adopted can be summarised as below:

- Modelling the flow domain – a two-dimensional rectangular flume with an inlet plate and the tailgate was developed in the Ansys design modeller.
- The entire domain was meshed and all the boundaries were named conveniently.
- The fluent solver was set up for calculating the flow. At this stage, several models such as turbulence model, air-water interface tracking model, and energy model were invoked, materials were selected, initial boundary conditions were defined, convergence criteria were set, locations for saving solution files were created etc.

- Suitable solution methods (discretisation schemes) were selected. Selection of quantities that are to be evaluated and stored for post-processing was made. Time step size, number of time steps and maximum number of iterations were set consequently calculating the flow.
- In the post-processing phase, sections were created, averaged flow quantities across the sections were measured and the data thus obtained were analysed.

The detailed methodology is presented below:

4.2.1 Modelling the flow domain

The two-dimensional flume was modelled using Ansys Design Modeller in Ansys Workbench. The length of the bed of the channel was taken to be 7m and the height of the channel was taken to be 0.6 meters, Fig. 4.2. A very mild slope of 1:2400 was provided to the channel bed. The sketch for the channel is shown in Fig. 4.3. The left vertical edge of the channel is the inlet plate that should be kept open to a height of 0.056m (Fig. 4.3) above the bed, during the simulations. So this edge is split into two parts with the lower part measuring 0.056m. The right vertical edge is the tailgate. The tailgate is intended to remain closed initially to obstruct the flow and open gradually during the flow. The right edge was split into two parts with the lower part being 0.1m. This lower part was further split into sixteen Equal parts(slots) as shown in Fig. 4.5. The reason for doing this is explained in section **4.2.4.8.1**. The same geometry file was used for all the simulations.

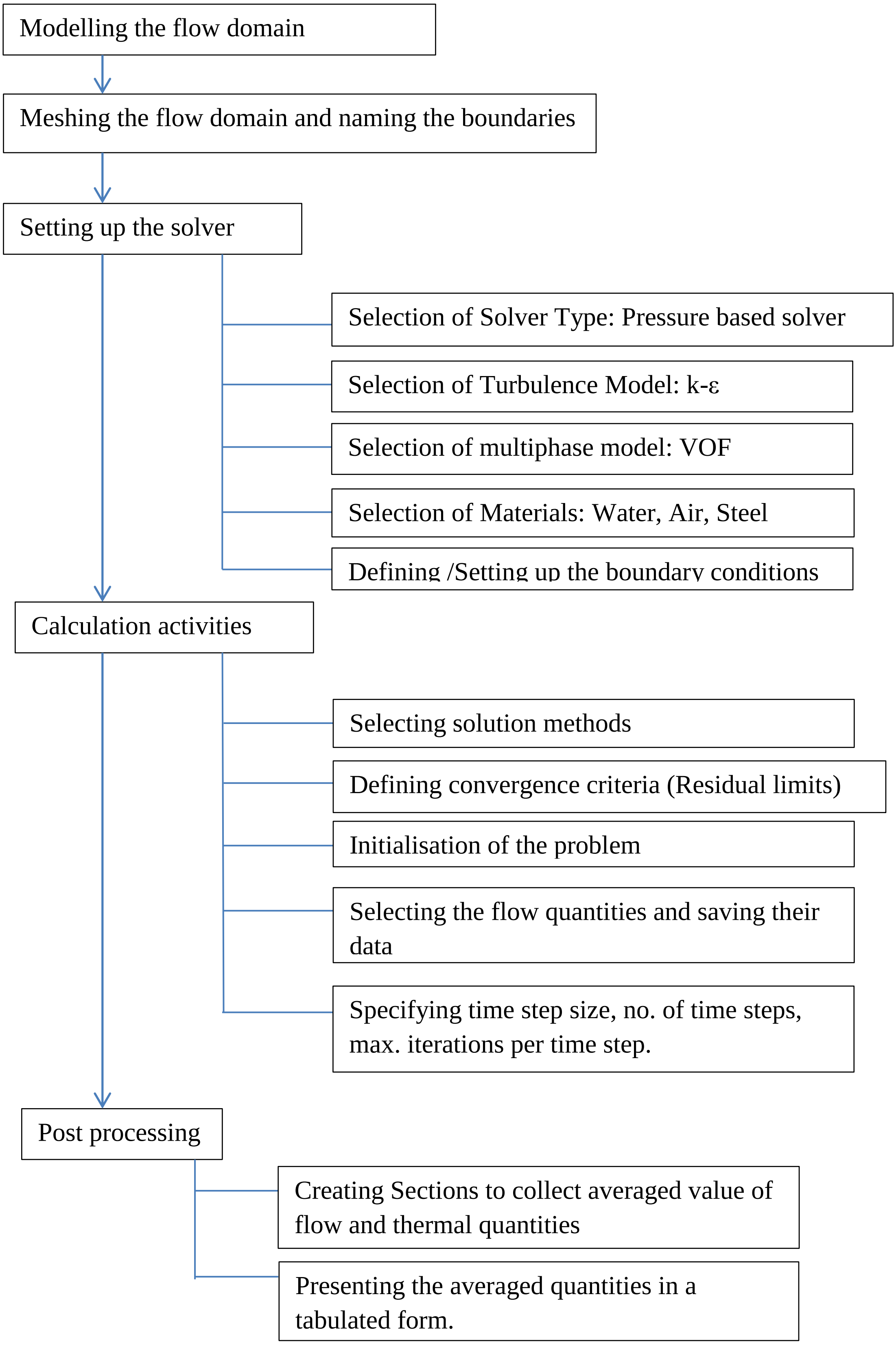

Fig. 4.1. Flow chart representing the methodology adopted.

4.2.2 Meshing the flow domain and naming the Boundaries

Since in the mesh properties table, physics was set to CFD and the solver was set to fluent, the Ansys meshing software (available within the Ansys Workbench) automatically set many meshing settings at suitable default, Fig. 4.8. Initially, a default mesh was generated. To refine the mesh further, the maximum face size was reduced to 0.01m. The exact cell (element) size could not be provided as the default size function was set to curvature (for CFD physics preference). Nevertheless, the size function was set to adaptive and the mesh was regenerated to check the element size keeping the other mesh settings at default. The element size was found to be 0.01m. After reverting back,

the mesh to curvature (default for CFD) size function, inflation with 5 inflation layers with a default growth rate of 1.2 (Fig. 4.7) was provided at the bed. Fig. 4.6 shows the mesh structure in comparison to the dimensions of the flume. Mesh reports regarding mesh statistics (Fig. 4.10), memory usage and mesh quality (Fig. 4.11) were obtained in Ansys “Fluent” solver console

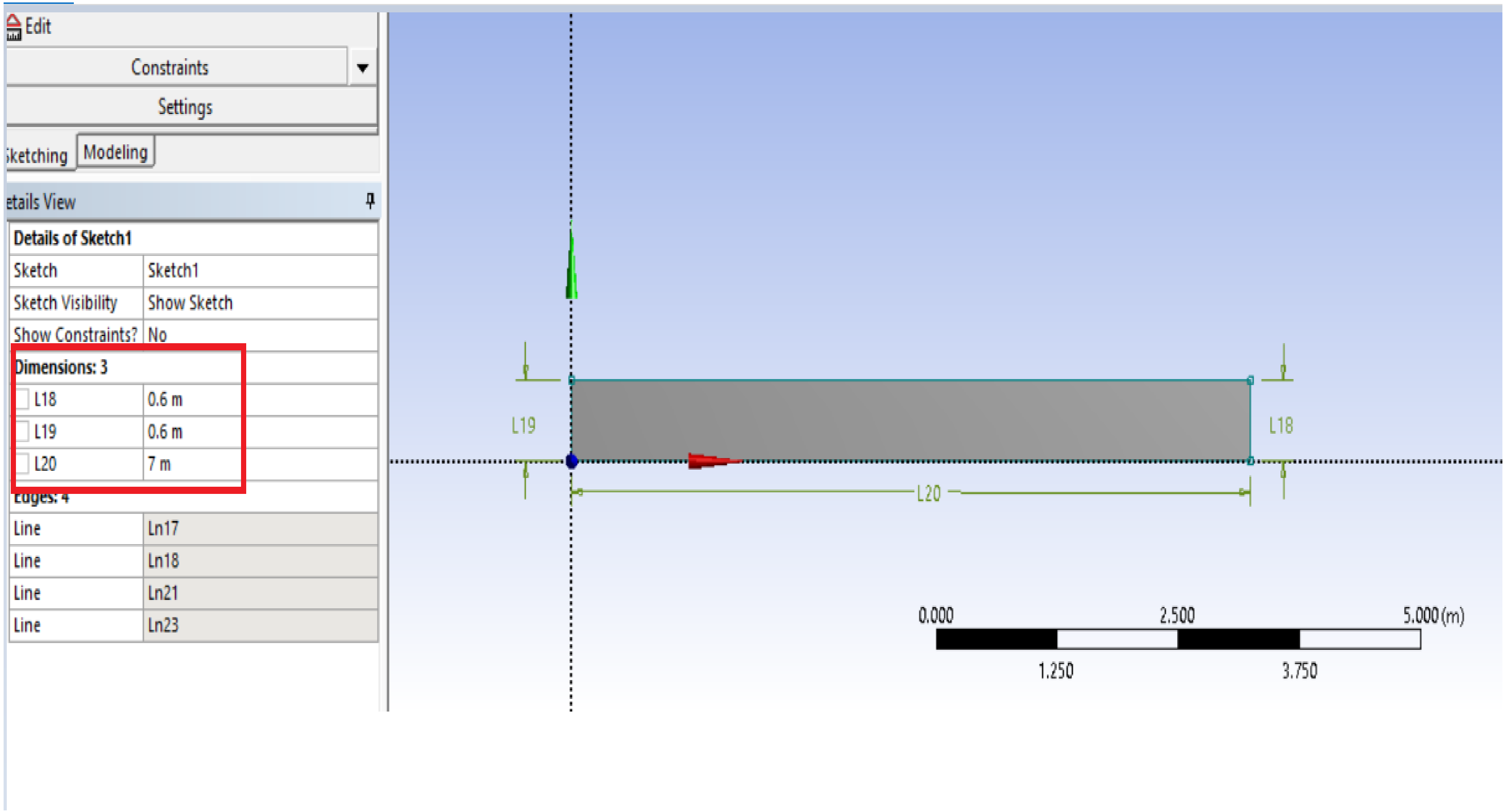

Details of Sketch1	
Sketch	Sketch1
Sketch Visibility	Show Sketch
Show Constraints?	No
Dimensions: 3	
☐ L18	0.6 m
☐ L19	0.6 m
☐ L20	7 m
Edges: 4	
Line	Ln17
Line	Ln18
Line	Ln21
Line	Ln23

Fig 4.2. Geometry of the rectangular flume with dimensions (enclosed in red box)

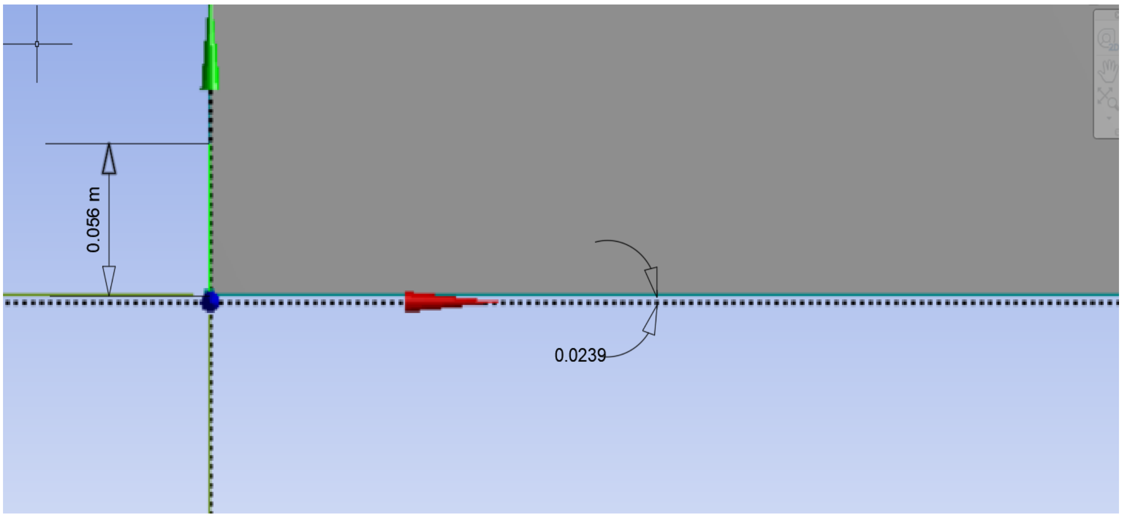

Fig. 4.3. Bed slope (in degrees) and the dimension of the inlet opening.

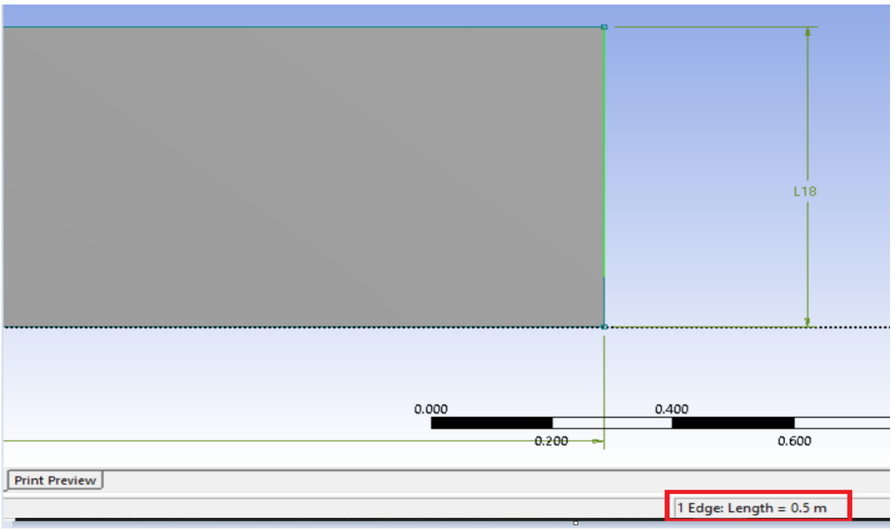

1 Edge: Length = 0.5 m

Fig. 4.4. Upper portion of the tailgate (highlighted in green) and its dimension (enclosed in red box)

1 Edge: Length = 0.00625 m

Fig. 4.5 One of the sixteen slots (highlighted in green) and its dimension (enclosed in red box)

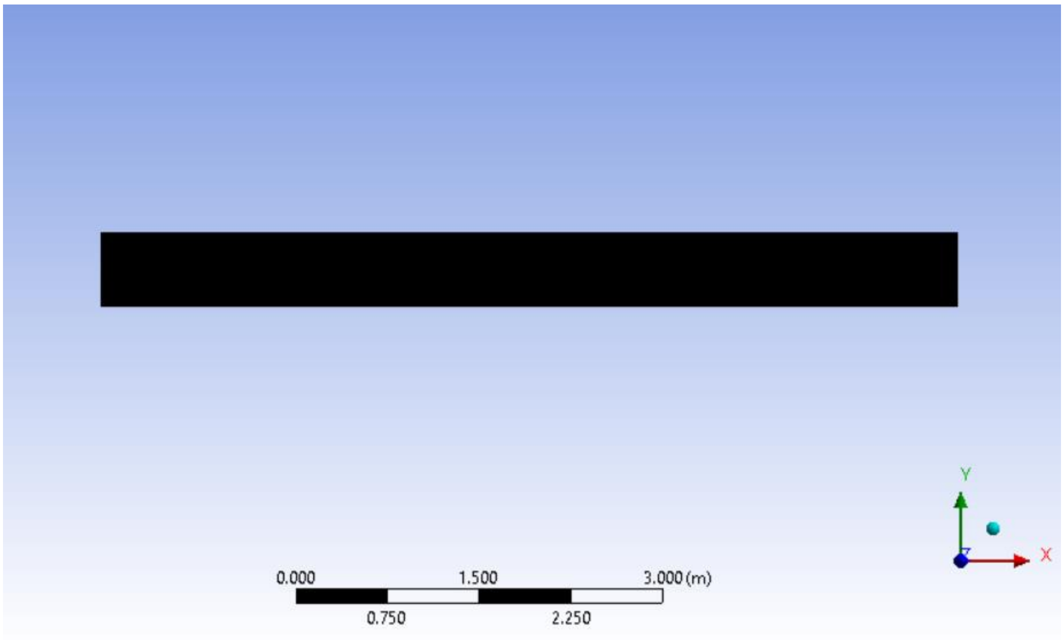

Fig. 4.6 Mesh structure as compared to the dimensions of the channel.

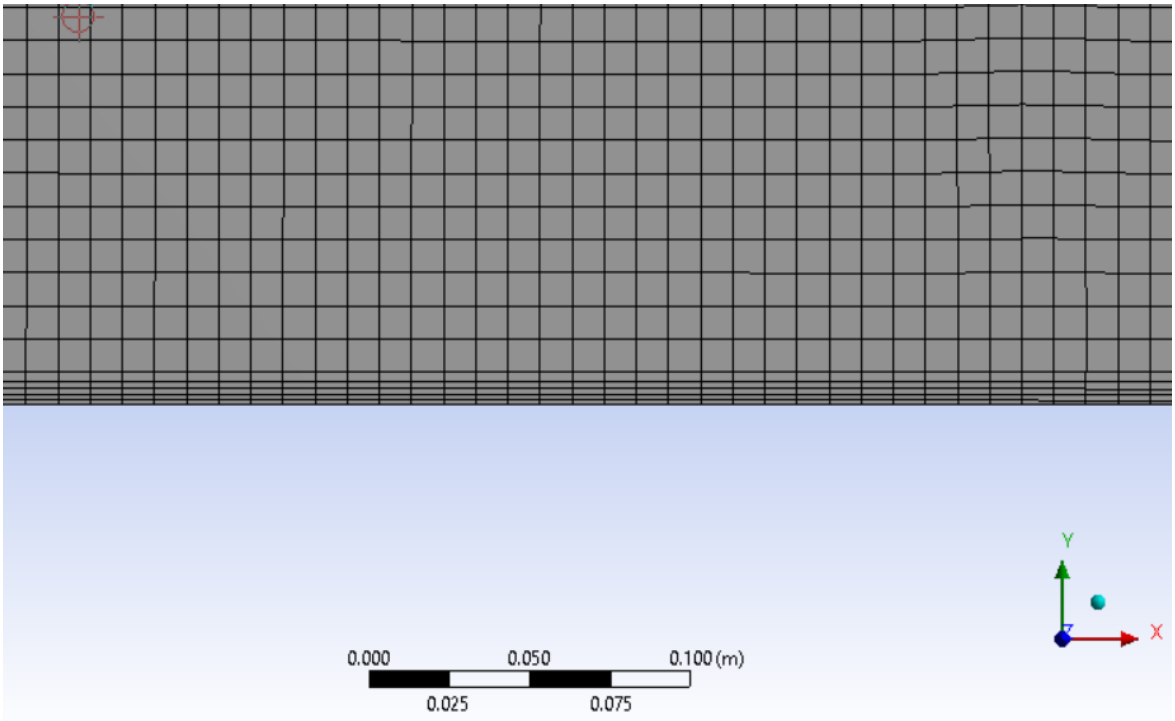

Fig. 4.7 Inflation layers at the bed

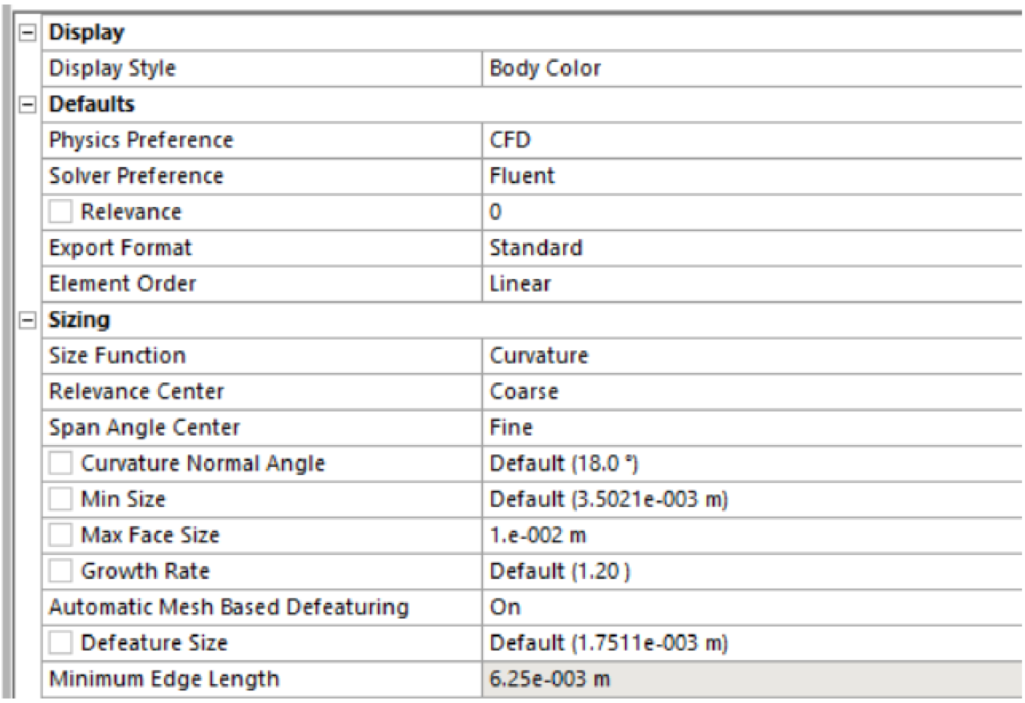

⊟ **Display**	
Display Style	Body Color
⊟ **Defaults**	
Physics Preference	CFD
Solver Preference	Fluent
☐ Relevance	0
Export Format	Standard
Element Order	Linear
⊟ **Sizing**	
Size Function	Curvature
Relevance Center	Coarse
Span Angle Center	Fine
☐ Curvature Normal Angle	Default (18.0 °)
☐ Min Size	Default (3.5021e-003 m)
☐ Max Face Size	1.e-002 m
☐ Growth Rate	Default (1.20)
Automatic Mesh Based Defeaturing	On
☐ Defeature Size	Default (1.7511e-003 m)
Minimum Edge Length	6.25e-003 m

Fig. 4.8. Physics, solver preferences, mesh sizing.

The figure below shows the settings for mesh quality check, advanced mesh, and mesh statistics

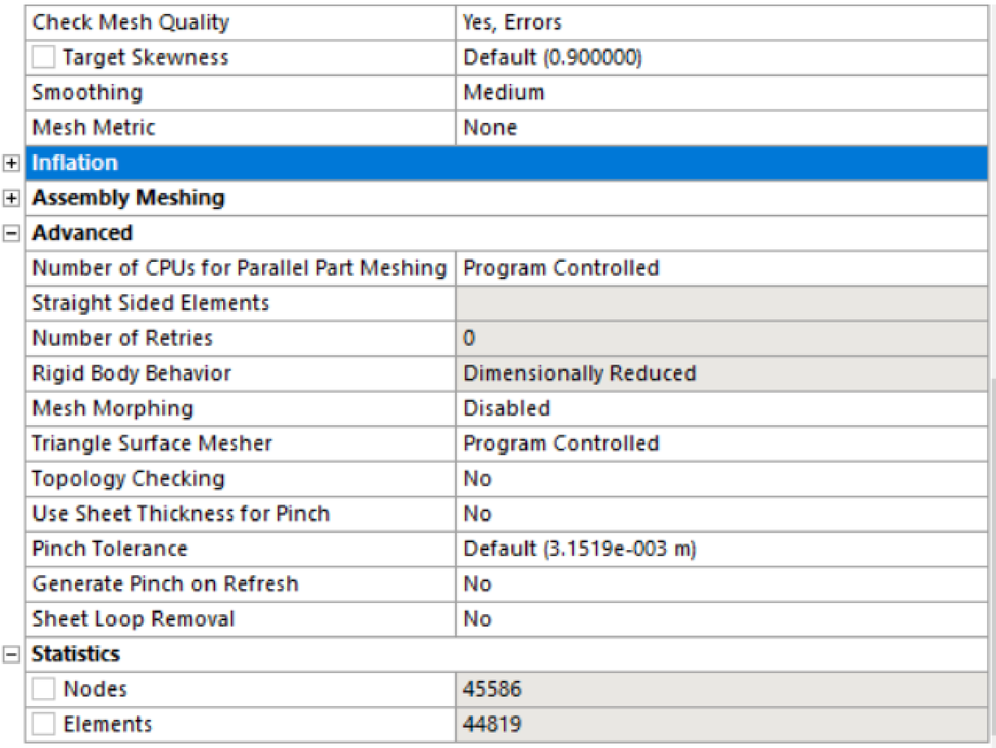

Check Mesh Quality	Yes, Errors
☐ Target Skewness	Default (0.900000)
Smoothing	Medium
Mesh Metric	None
⊞ **Inflation**	
⊞ **Assembly Meshing**	
⊟ **Advanced**	
Number of CPUs for Parallel Part Meshing	Program Controlled
Straight Sided Elements	
Number of Retries	0
Rigid Body Behavior	Dimensionally Reduced
Mesh Morphing	Disabled
Triangle Surface Mesher	Program Controlled
Topology Checking	No
Use Sheet Thickness for Pinch	No
Pinch Tolerance	Default (3.1519e-003 m)
Generate Pinch on Refresh	No
Sheet Loop Removal	No
⊟ **Statistics**	
☐ Nodes	45586
☐ Elements	44819

Fig. 4.9 settings for mesh quality check, advanced mesh, mesh statistics

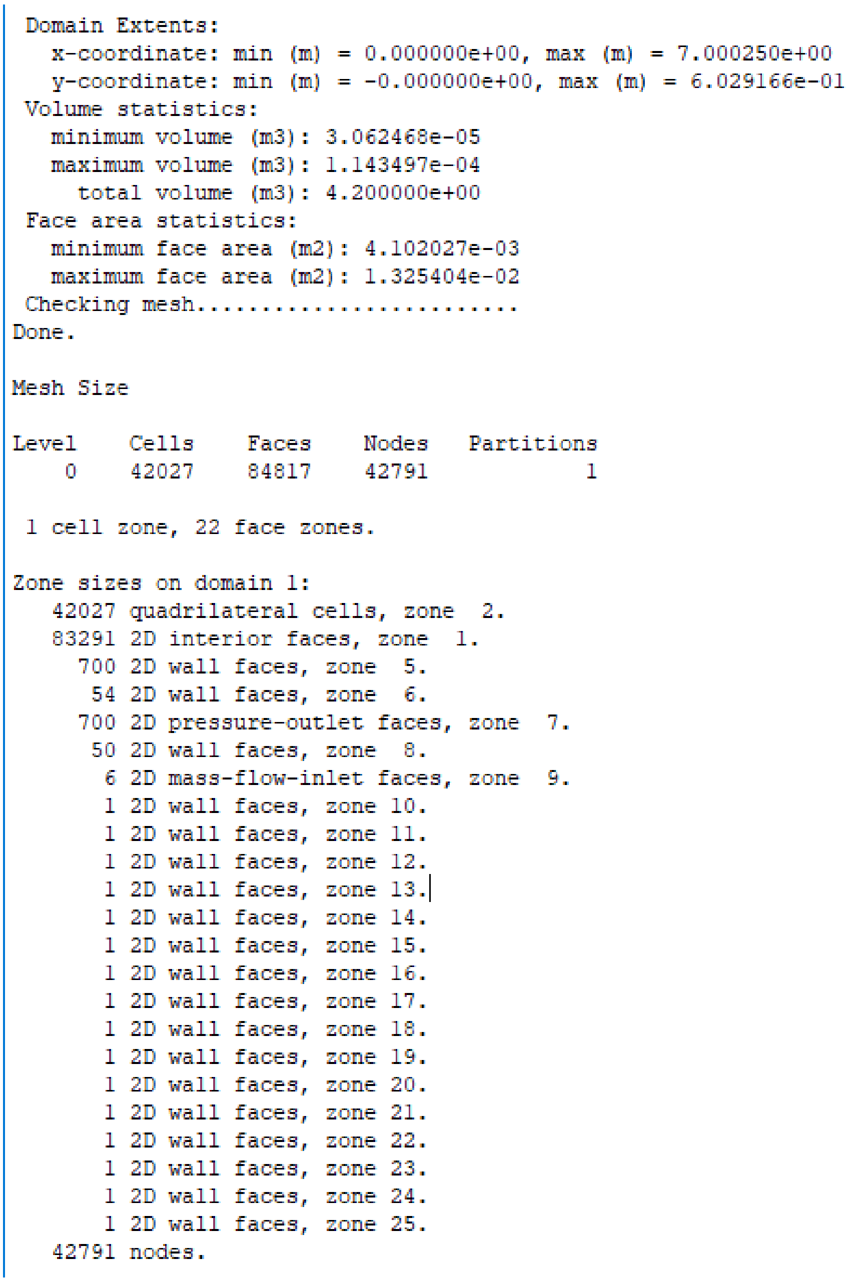

```
 Domain Extents:
   x-coordinate: min (m) = 0.000000e+00, max (m) = 7.000250e+00
   y-coordinate: min (m) = -0.000000e+00, max (m) = 6.029166e-01
 Volume statistics:
   minimum volume (m3): 3.062468e-05
   maximum volume (m3): 1.143497e-04
     total volume (m3): 4.200000e+00
 Face area statistics:
   minimum face area (m2): 4.102027e-03
   maximum face area (m2): 1.325404e-02
 Checking mesh.........................
Done.

Mesh Size

Level    Cells    Faces    Nodes   Partitions
    0    42027    84817    42791            1

 1 cell zone, 22 face zones.

Zone sizes on domain 1:
   42027 quadrilateral cells, zone  2.
   83291 2D interior faces, zone  1.
     700 2D wall faces, zone  5.
      54 2D wall faces, zone  6.
     700 2D pressure-outlet faces, zone  7.
      50 2D wall faces, zone  8.
       6 2D mass-flow-inlet faces, zone  9.
       1 2D wall faces, zone 10.
       1 2D wall faces, zone 11.
       1 2D wall faces, zone 12.
       1 2D wall faces, zone 13.
       1 2D wall faces, zone 14.
       1 2D wall faces, zone 15.
       1 2D wall faces, zone 16.
       1 2D wall faces, zone 17.
       1 2D wall faces, zone 18.
       1 2D wall faces, zone 19.
       1 2D wall faces, zone 20.
       1 2D wall faces, zone 21.
       1 2D wall faces, zone 22.
       1 2D wall faces, zone 23.
       1 2D wall faces, zone 24.
       1 2D wall faces, zone 25.
   42791 nodes.
```

Fig. 4.10 Report showing mesh statistics.

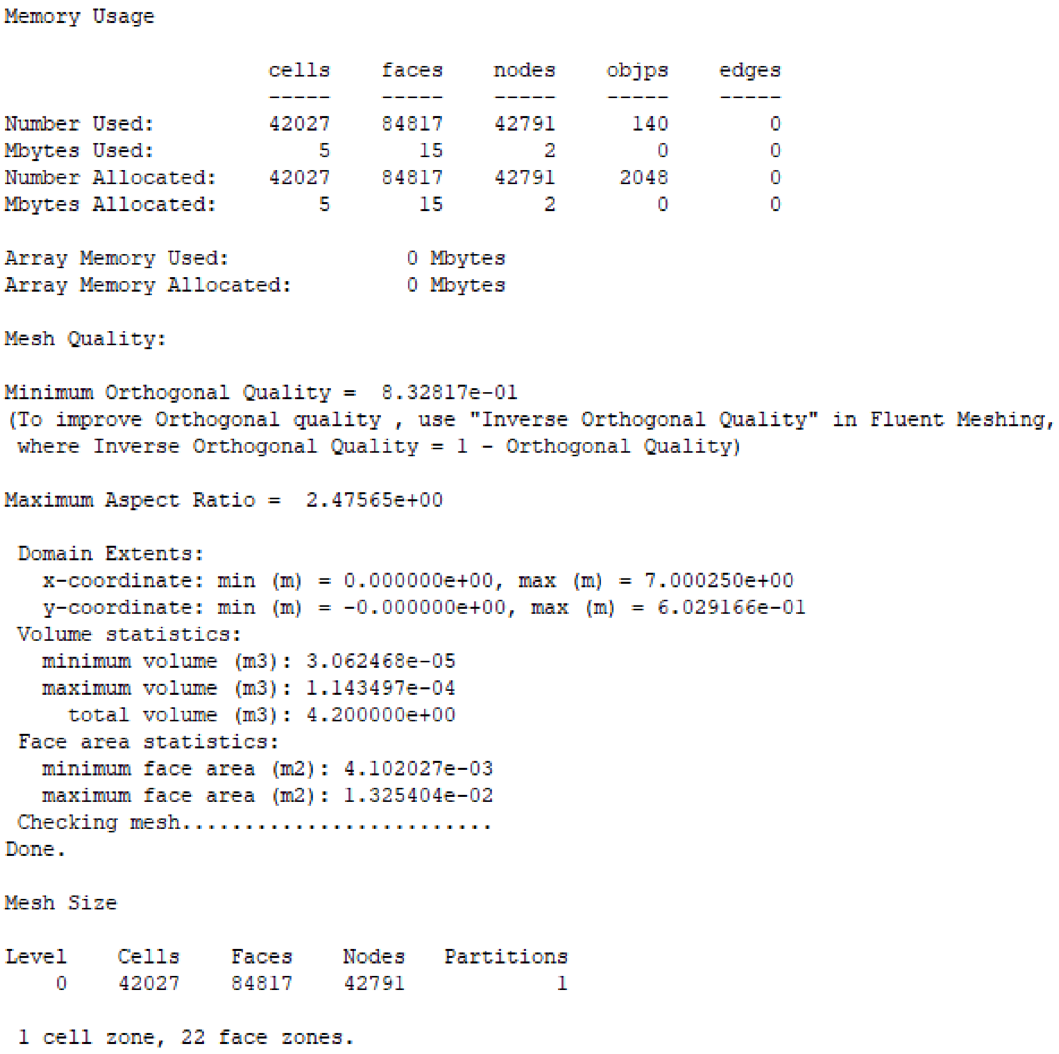

```
Memory Usage

                     cells     faces     nodes     objps     edges
                     -----     -----     -----     -----     -----
Number Used:         42027     84817     42791       140         0
Mbytes Used:             5        15         2         0         0
Number Allocated:    42027     84817     42791      2048         0
Mbytes Allocated:        5        15         2         0         0

Array Memory Used:              0 Mbytes
Array Memory Allocated:         0 Mbytes

Mesh Quality:

Minimum Orthogonal Quality =  8.32817e-01
(To improve Orthogonal quality , use "Inverse Orthogonal Quality" in Fluent Meshing,
 where Inverse Orthogonal Quality = 1 - Orthogonal Quality)

Maximum Aspect Ratio =  2.47565e+00

 Domain Extents:
   x-coordinate: min (m) = 0.000000e+00, max (m) = 7.000250e+00
   y-coordinate: min (m) = -0.000000e+00, max (m) = 6.029166e-01
 Volume statistics:
   minimum volume (m3): 3.062468e-05
   maximum volume (m3): 1.143497e-04
     total volume (m3): 4.200000e+00
 Face area statistics:
   minimum face area (m2): 4.102027e-03
   maximum face area (m2): 1.325404e-02
 Checking mesh........................
Done.

Mesh Size

Level    Cells    Faces    Nodes   Partitions
    0    42027    84817    42791            1

 1 cell zone, 22 face zones.
```

Fig. 4.11 Report showing memory usage by the mesh and “mesh quality”

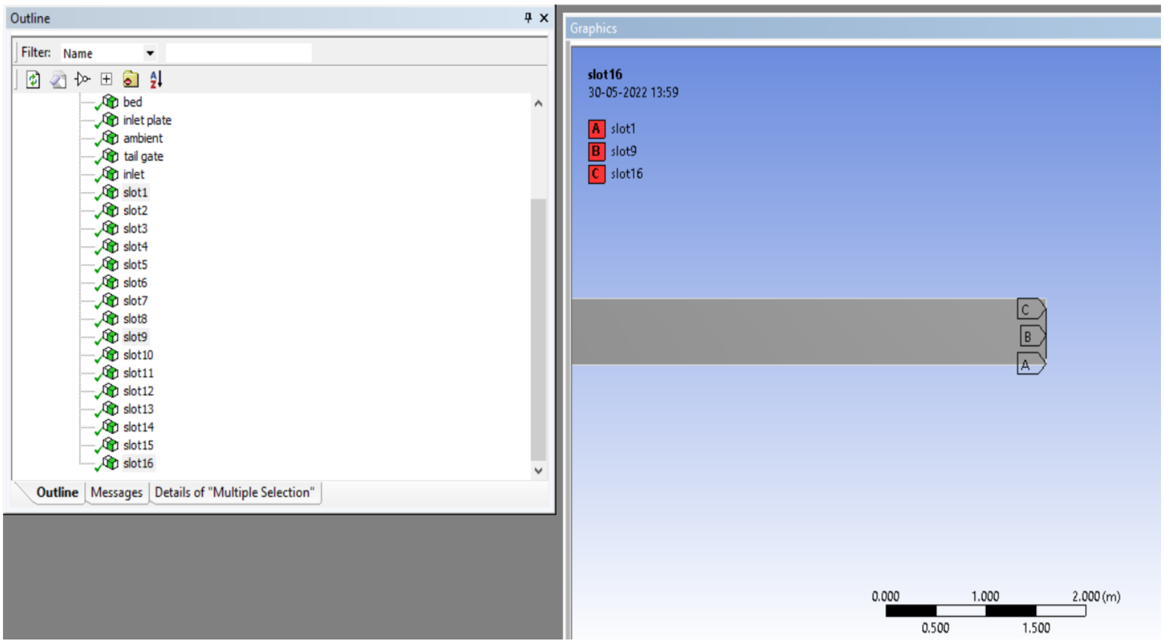

Fig. 4.12 "Named Selection" for slots 1, 9 and 16 are marked for display.

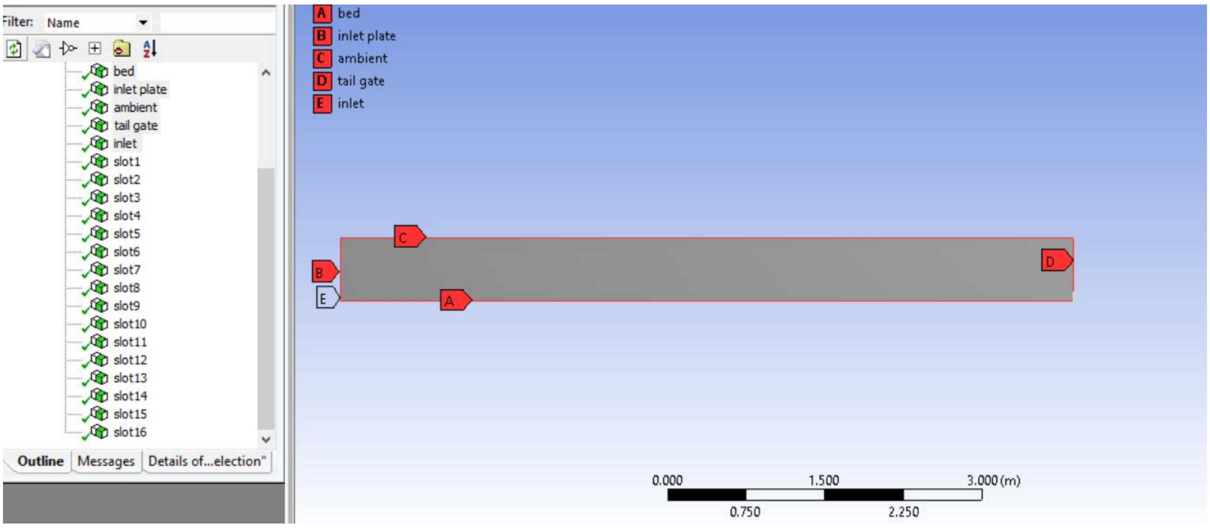

Fig. 4.13. Boundaries and their respective "named selections"

4.2.3 Setting up the Solver

4.2.3.1 General Setup

In the general setup (Fig. 4.14), for the solver settings, the “pressure based” type was selected and “Absolute” velocity formulation was selected, both by default. Under the time settings “transient” option was selected for 2D Space “Planar” was selected.

“Gravity” was activated and a value of -9.81 was assigned in the Y-component of the gravity. Units were set to S.I by default.

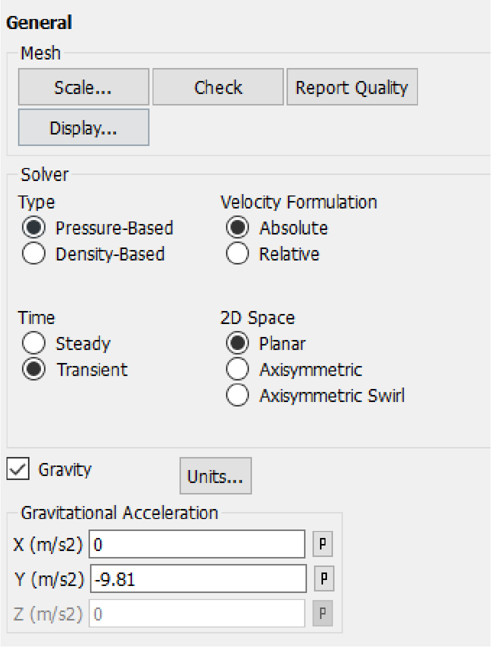

General

Mesh

Solver

Type
● Pressure-Based
○ Density-Based

Velocity Formulation
● Absolute
○ Relative

Time
○ Steady
● Transient

2D Space
● Planar
○ Axisymmetric
○ Axisymmetric Swirl

☑ Gravity

Gravitational Acceleration
X (m/s2) 0
Y (m/s2) -9.81
Z (m/s2) 0

Fig. 4.14. General settings for the solver.

4.2.3.2 Selection of various mathematical models

4.2.3.2.1 Selection of Turbulence Model and Activating the Energy model.

In Ansys fluent, the desired turbulence model may be selected using the “Viscous Model” option under the “Models” option. “k-ε” turbulence model was activated. “standard” k-ε model was selected. As for near-wall treatment “Standard” wall treatment was chosen. “Viscous heating” was also activated. The constants involved in k-ε turbulence models were left with their default values as shown in Fig. 4.15.

The “Energy” Model was activated for activating the thermal analysis of the flow for the consideration of the convection heat transfer effects particularly. “Radiation”, “Heat

Exchanger” and other models that were of very minimal to no significance, were kept inactivated as shown in Fig. 4.15

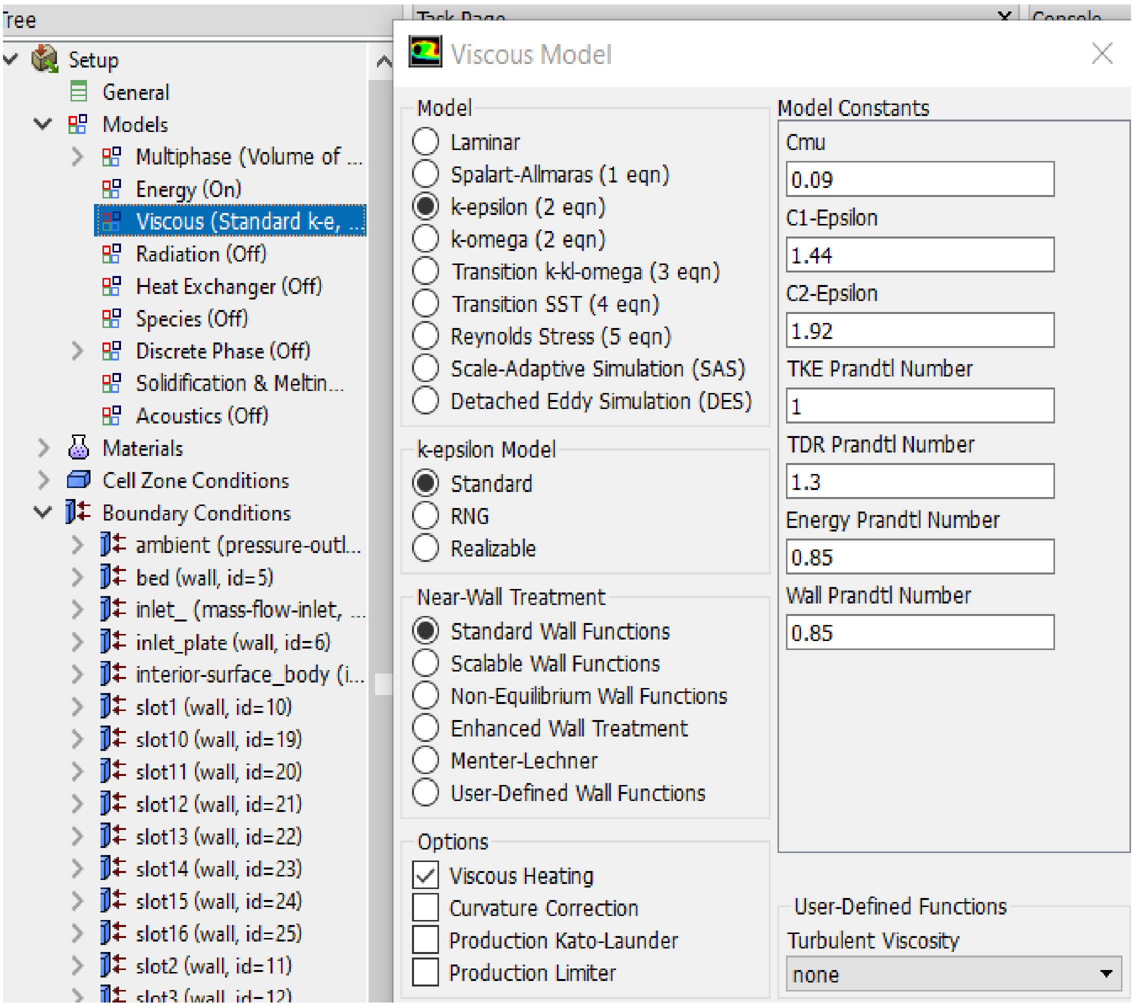

Viscous Model

Model
○ Laminar
○ Spalart-Allmaras (1 eqn)
● k-epsilon (2 eqn)
○ k-omega (2 eqn)
○ Transition k-kl-omega (3 eqn)
○ Transition SST (4 eqn)
○ Reynolds Stress (5 eqn)
○ Scale-Adaptive Simulation (SAS)
○ Detached Eddy Simulation (DES)

k-epsilon Model
● Standard
○ RNG
○ Realizable

Near-Wall Treatment
● Standard Wall Functions
○ Scalable Wall Functions
○ Non-Equilibrium Wall Functions
○ Enhanced Wall Treatment
○ Menter-Lechner
○ User-Defined Wall Functions

Options
☑ Viscous Heating
☐ Curvature Correction
☐ Production Kato-Launder
☐ Production Limiter

Model Constants
Cmu: 0.09
C1-Epsilon: 1.44
C2-Epsilon: 1.92
TKE Prandtl Number: 1
TDR Prandtl Number: 1.3
Energy Prandtl Number: 0.85
Wall Prandtl Number: 0.85

User-Defined Functions
Turbulent Viscosity: none

Fig. 4.15 Viscous model dialogue box showing settings for k-ε turbulence model

4.2.3.2.2 Selection of Multiphase models

“Volume of fluid” was selected as the multiphase model for the present simulation. Volume fraction parameters formulation was set to “implicit”. The value for volume fraction cut-off was 10^{-6}. “Implicit” Scheme was adopted for body force formulation. In interface modelling, the “sharp” option was selected. Finally, the number of Eulerian phases was set to 2, Fig. 4.16.

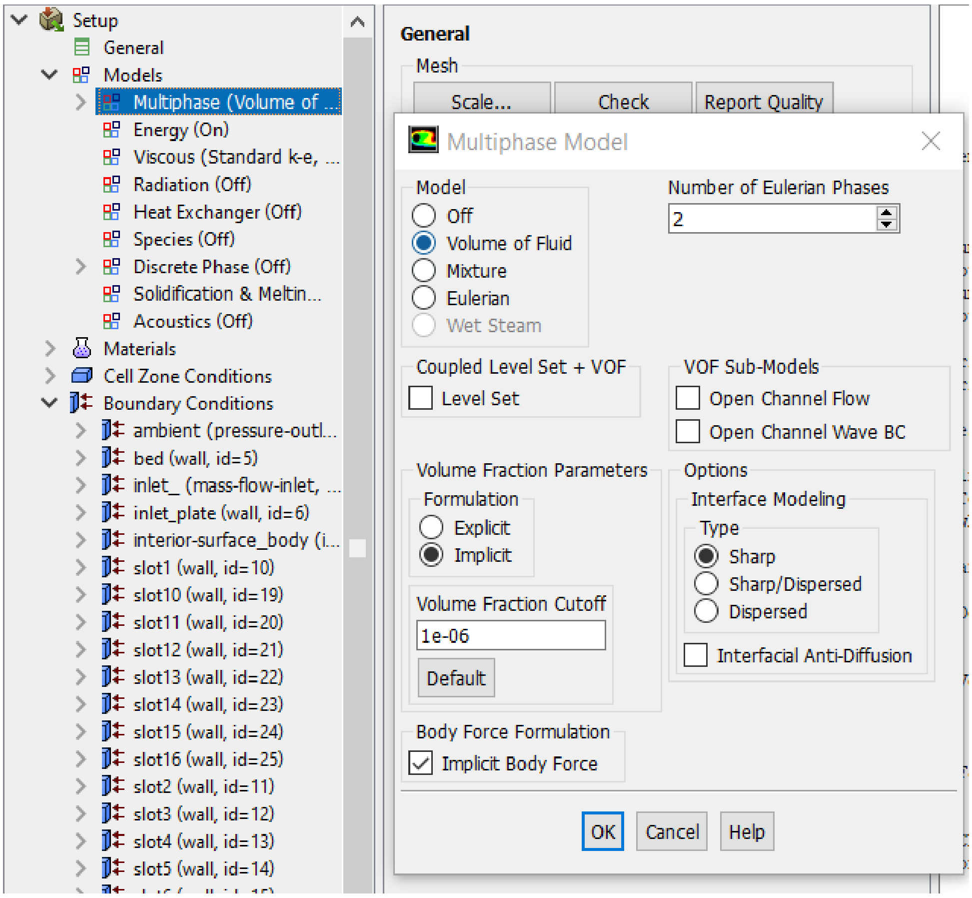

Multiphase Model

Model
- ○ Off
- ● Volume of Fluid
- ○ Mixture
- ○ Eulerian
- ○ Wet Steam

Number of Eulerian Phases: 2

Coupled Level Set + VOF
- ☐ Level Set

VOF Sub-Models
- ☐ Open Channel Flow
- ☐ Open Channel Wave BC

Volume Fraction Parameters
- Formulation
  - ○ Explicit
  - ● Implicit
- Volume Fraction Cutoff: 1e-06

Options
- Interface Modeling
  - Type
    - ● Sharp
    - ○ Sharp/Dispersed
    - ○ Dispersed
  - ☐ Interfacial Anti-Diffusion

Body Force Formulation
- ☑ Implicit Body Force

Fig. 4.16. Multiphase model dialogue box showing settings for VOF model.

4.2.3.3 Selection of materials

From the materials panel, water and air with their specified physical properties were selected as fluids. As for solids, steel and wood were selected. Steel was selected as materials to be applied to the inlet gate and the entire tailgate. Wood was selected to act as a hypothetical material for bed with the thermal properties of wood but with different friction property that was specified later. It was intended to minimise the conduction of heat from the water to the bed surface so that most of the heat transfer (loss) from the water could occur only due to convection to the ambient and hydraulic jump effects. Water was assigned as the secondary phase and air was assigned as the primary phase in the “phases” section under the “multiphase” tab.

4.2.3.4 Setting the Boundary conditions and Cell zone conditions.

Ansys fluent solver automatically lists all the boundaries that were named in the mesh module previously. These boundaries are now called zones. Also, the solver assigns default boundary conditions-e.g. materials, friction etc. and the initial conditions-volume fraction of each phase, temperature, velocity etc. to each of these zones. Most of these default values had to be changed to their proper values for each zone in the following manner:

4.2.3.4.1 Setting up the Inlet Boundary

For the “*inlet*” zone, corresponding to the mixture phase, the following edits were done:

The boundary “type” was changed to “mass-flow inlet” from its default value of “wall”.

In the Momentum tab, the Reference frame was kept at its default value of “Absolute”.

The initial gauge pressure was set to zero.

“Direction vector” was selected for the direction specification method for which the X-component of flow direction was assigned a value of 1 and the Y-component of flow direction was assigned a value of 0.

For “Turbulence”, default settings were kept for specification method – intensity and viscosity and hence for the turbulent intensity and turbulent viscosity ratio.

Under the “Thermal” tab, a total temperature of 313 K was set. This temperature is the inlet water temperature i.e. 40°C and remained the same for all the simulations.

For the same “inlet” zone, selecting the water phase enabled us to enter the “mass flow rate” of 106 kg/s. This value of mass flow rate was calculated based upon the assumed velocity, intended initial water depth of the supercritical flow, inlet opening dimension, density, and width of the channel (flume) as in experiments carried out by Mondal *et al*. (2020) for reference.

For the air phase, the mass flow rate value was assigned a value of zero.

4.2.3.4.2 Setting up the “Bed” Boundary

The boundary “type” was kept as “wall” which was the default “type” assigned by the solver.

For the “phase” selected as “mixture”, the following edits were done:

In the “Momentum” tab, “Stationary Wall” was selected for “Wall motion”.

“Shear Condition” was set to “no-slip”.

“Standard” Roughness Model was selected for “Wall Roughness”. Corresponding to this a “Roughness Height” of 4.5×10^{-5} m was assigned. This value of roughness height corresponds to a Perspex bed (Marriott and Jayaratne, 2010). “Roughness constant” was left at its default value of 0.5.

Under the “Thermal” tab, “Temperature” was selected for the “Thermal” Conditions. Since at initial conditions, the temperature of the bed will be Equal to the ambient temperature. So for every new simulation with a different ambient temperature, the “Temperature” value had to be changed. As, an example, if a simulation corresponds to an ambient temperature of 10ºC, the value for the “Temperature” of the bed will be 283.15 K. Obviously, this is the initial temperature of the “Wall” and will change as the calculations proceed due to heat transfer from the water. Since there is no heat source associated with the bed, the “heat generation” value was left at zero.

4.2.3.4.3 Setting up the “inlet plate” Boundary

Since the inlet plate is a vertical wall, so the boundary “type” was left at its default selection of “wall”. In the “Momentum” tab, “Stationary Wall” was selected for “Wall motion”. “Shear Condition” was set to “no-slip”, though it is of no significance in this case. “Standard” Roughness Model was selected for “Wall Roughness” and roughness height was assigned a value of zero. Under the “Temperature” tab, under the “Thermal” tab, “Temperature” was selected for the “Thermal” Conditions. As explained in **4.2.3.4.2,** the value of temperature would be that of the ambient temperature and the heat generation rate was zero.

4.2.3.4.4 Setting up the “tailgate” Boundary

The zone named “Tailgate” refers to the upper portion of the tailgate that was left *unsplitted*. For this boundary “type” was selected as “wall”. In the “Momentum” tab, “Stationary Wall” was selected for “Wall motion”. “Shear Condition” was set to “no-slip”, though it is of no significance in this case. “Standard” roughness model was selected for “Wall Roughness” and roughness height was assigned a value of zero. Under the “Temperature” tab, under the “Thermal” tab, “Temperature” was selected for the “Thermal” Conditions. As explained in **4.2.3.4.2,** the value of temperature would be that of the ambient temperature and the heat generation rate was zero.

4.2.3.4.5 Setting up the "tailgate slots" Boundary

The lower portion of the tailgate was splitted up into 16 parts (slots). The reason for this is explained in **4.2.4.8.1.** All the slots are initially set as "wall" type boundary as the tailgate is fully closed initially. As in any "wall" boundary, excluding the bed, "stationary wall", "no-slip condition" and zero "roughness height" were specified. "Temperature" was selected in the "thermal conditions" and its value was set Equal to the ambient temperature as explained in **4.2.3.4.2.** As the calculation proceeds, the slots have to be changed from "wall" type boundary condition to "outlet" type boundary condition as explained in **4.2.4.8.1**.

4.2.3.4.6 Setting up the "ambient" Boundary

The upper horizontal edge of the rectangular flume geometry was named "ambient" since this zone was indicative of the ambient. This zone was set up as a "pressure outlet" type boundary. For the "phase" selected as "mixture", the temperature was assigned the value for the ambient temperature considered. Other settings were left unchanged at their default values.

4.2.4 Calculations

Once the selection of the desired models, materials and setting up of the boundary conditions were done, it was necessary to select the solution method, set the criteria for residuals, specify the calculation activities, the path for saving the calculation data, create the contours for water volume fractions, creates solution animations and specifying time step size, number iterations etc. as explained in the sections below:

4.2.4.1 Selecting the Solution methods

On the "solution methods" task page, various methods and/or schemes for the calculations were selected.

Firstly, the scheme for "pressure-velocity" coupling was selected as "SIMPLE". Besides being the default value for the pressure-based segregated solver, this scheme has the ability to converge fast.

Under spatial discretisation, for the calculation of gradients of various quantities, the "Least-squares Cell-Based" method was used as it required lesser computational power but gave acceptable accuracy.

For pressure interpolation "PRESTO!" scheme was selected as the simulation of hydraulic jump involves intense turbulence and high swirls.

The “Second-Order Upwind” scheme was selected for spatial discretisation of the momentum Equation for its improved accuracy.

A “Compressive” scheme was selected for spatial discretisation of the volume fraction of phases.

“First order upwind” scheme i.e. the default scheme for the pressure-based solver, was selected for spatially discretising the transport equations for k (turbulence kinetic energy) and ε (turbulence dissipation rate).

For discretisation of energy conservation equation, “Second-order upwind scheme was used”.

4.2.4.2 Setting the Residual Monitor

The convergence criteria i.e. the acceptable residual limits can be set by selecting “Residual” in the “Monitor” option under “Solution” in the tree (navigation pane). In the residual monitor dialogue box Fig. 4.17, the “absolute criteria” for the scaled residuals related to continuity, *x*-velocity, *y*- velocity, k, ε, and vf-water Equations, were all set to 0.0001 but for the residual related to energy equation was kept at its default value of 10^{-6}. All the other parameters were left unchanged at their default values.

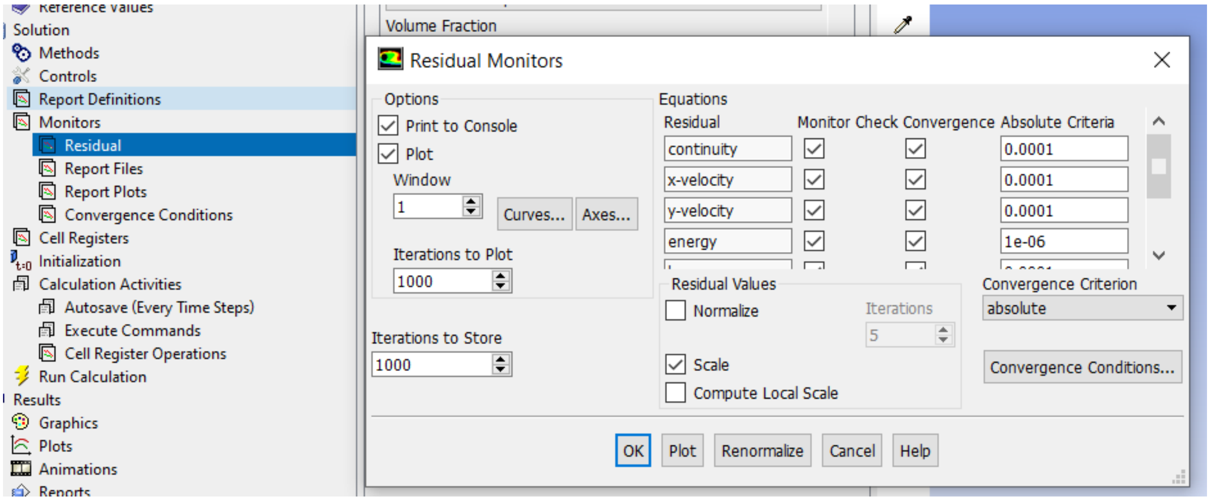

Residual Monitors

Options
☑ Print to Console
☑ Plot
Window 1
Iterations to Plot 1000
Iterations to Store 1000

Equations

Residual	Monitor	Check Convergence	Absolute Criteria
continuity	☑	☑	0.0001
x-velocity	☑	☑	0.0001
y-velocity	☑	☑	0.0001
energy	☑	☑	1e-06

Residual Values
☐ Normalize
Iterations 5
☑ Scale
☐ Compute Local Scale

Convergence Criterion absolute

Fig. 4.17 Residual monitor dialogue box showing convergence criteria

4.2.4.3 Initialising the solution.

The initialisation of the solution was done by opening the “initialization” task page Fig. 4.18 from the navigation pane. “Standard Initialization” was selected for the initialization method. All the variables were computed from the “Inlet” zone. Values for all the variables such as x-velocity, *y*-velocity, temperature, turbulence kinetic energy, turbulence dissipation rate and water volume fraction were computed at time *t*=0 automatically. However, the water volume fraction was computed as 1 which had to be changed to 0 manually. Also, any non-zero value for the *y*-component of the velocity had to be changed to zero. Finally, the solution was initialised by clicking “initialize”.

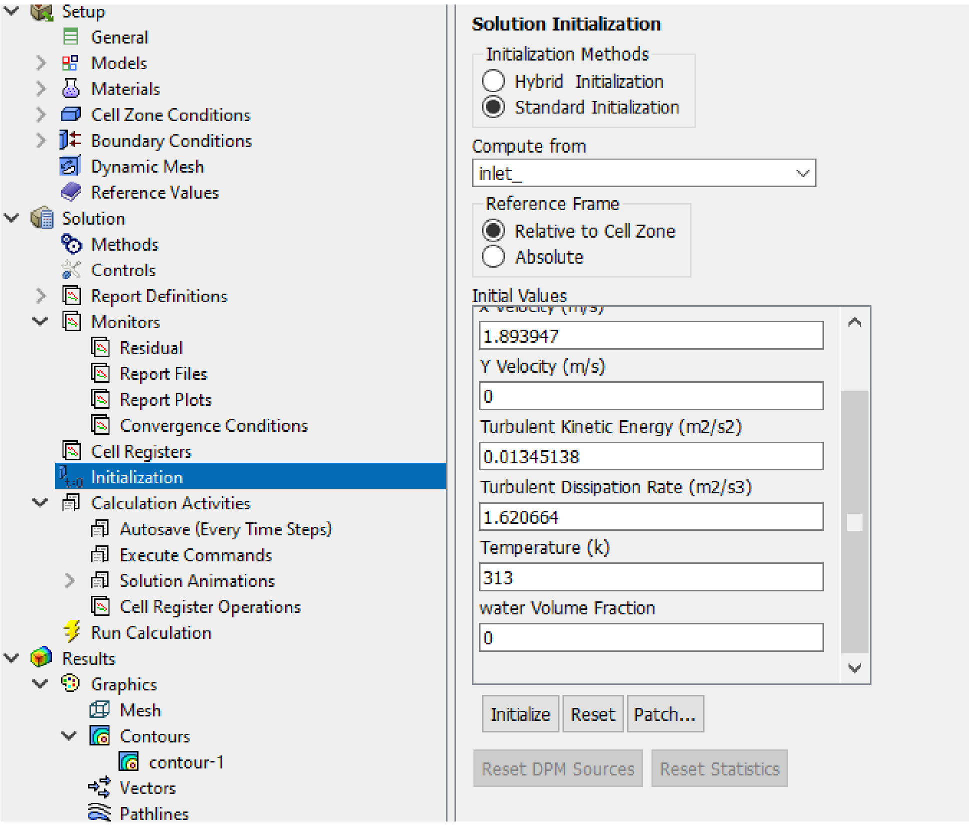

Solution Initialization

Initialization Methods
○ Hybrid Initialization
● Standard Initialization

Compute from: inlet_

Reference Frame
● Relative to Cell Zone
○ Absolute

Initial Values
X Velocity (m/s): 1.893947
Y Velocity (m/s): 0
Turbulent Kinetic Energy (m2/s2): 0.01345138
Turbulent Dissipation Rate (m2/s3): 1.620664
Temperature (k): 313
water Volume Fraction: 0

Fig. 4.18 Initialisation task page showing initialisation setup

4.2.4.4 Calculation activities and path for saving the case and data files.

The solution data and the setup data were exported from the solver to specific files for the convenience of using them during post-processing in CFD post.

The calculation activities task page was opened and the “automatic export” window (Fig. 4.20) was opened by “creating” solution data export. The file type was selected as “CFD-Post Compatible”. This was done in order to export the case files and data files together in .cdat format that is readable by CFD post (fluent post-processing software). “write case file every time” was ticked though this was completely optional.

- The frequency time-step was set to 10 so as to save the data and case files at an interval of 10 time steps. “Time-step” was selected to append with the file name.
- In the “cell zones” panel, “surface _body” was pre-selected as there was only one cell zone. The surfaces were also pre-selected by default.
- In the “Quantities” panel the following quantities (marked blue in Fig. 4.19) that are of importance for post-processing were selected:

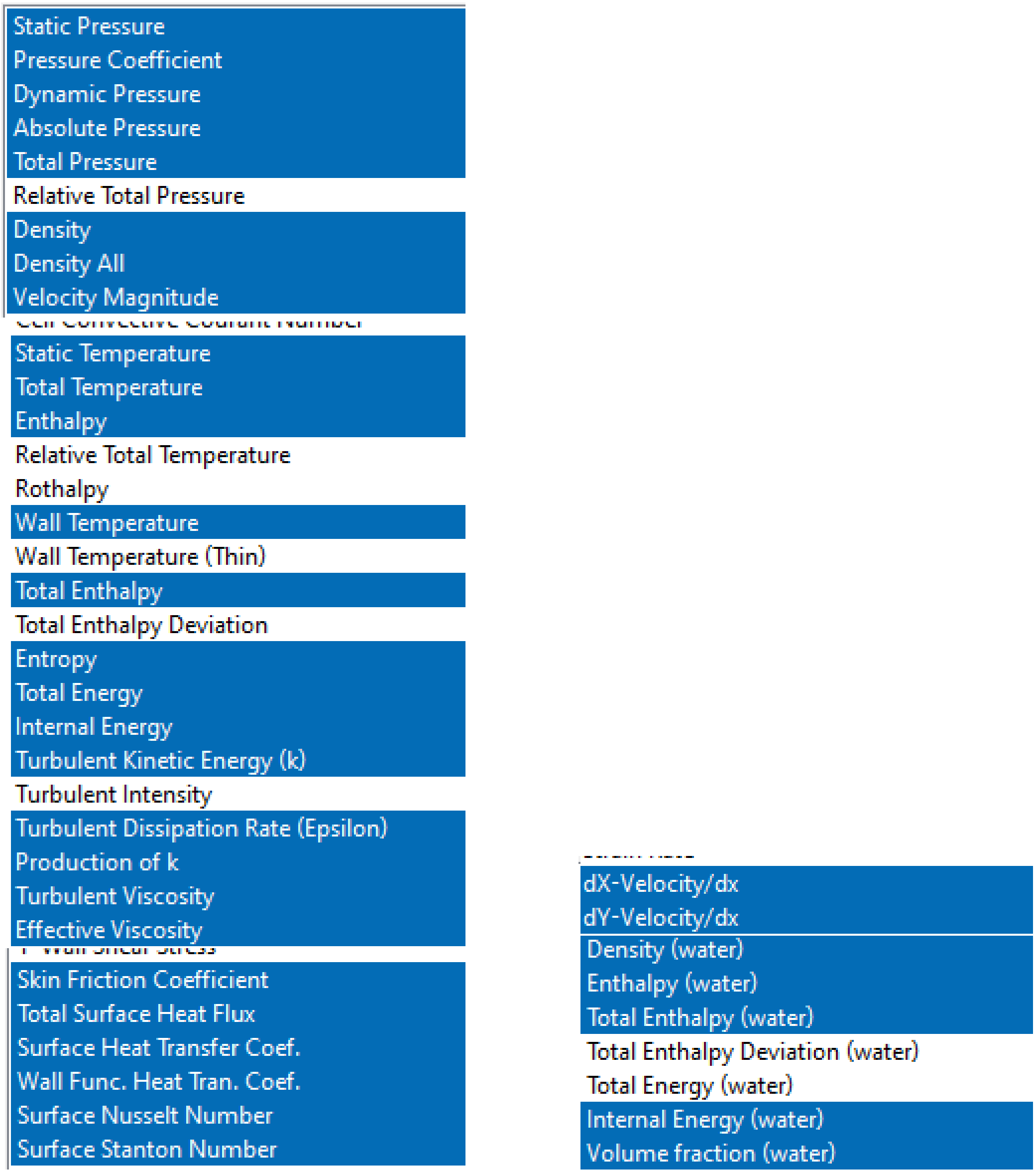

Static Pressure
Pressure Coefficient
Dynamic Pressure
Absolute Pressure
Total Pressure
Relative Total Pressure
Density
Density All
Velocity Magnitude
Static Temperature
Total Temperature
Enthalpy
Relative Total Temperature
Rothalpy
Wall Temperature
Wall Temperature (Thin)
Total Enthalpy
Total Enthalpy Deviation
Entropy
Total Energy
Internal Energy
Turbulent Kinetic Energy (k)
Turbulent Intensity
Turbulent Dissipation Rate (Epsilon)
Production of k
Turbulent Viscosity
Effective Viscosity
Skin Friction Coefficient
Total Surface Heat Flux
Surface Heat Transfer Coef.
Wall Func. Heat Tran. Coef.
Surface Nusselt Number
Surface Stanton Number

dX-Velocity/dx
dY-Velocity/dx
Density (water)
Enthalpy (water)
Total Enthalpy (water)
Total Enthalpy Deviation (water)
Total Energy (water)
Internal Energy (water)
Volume fraction (water)

Fig. 4.19 Quantities selected in automatic export settings.

- The data files were also exported in .dat.gz format to the same location because these data files are only readable by the Fluent solver (stand-alone application) and not the data files in .cdat format. To save the data file in this format, the autosave dialogue box (Fig. 4.21) was opened by clicking “autosave (Every Time Steps)” in Calculation Activities. Since the data files occupy a huge memory in the disc, “Retain only most recent files” was ticked and the maximum number of data files was limited to 5. Other settings were shown in Fig. 4.21.

Since it took a huge time to complete the simulations and the system gets heated, the fluent solver application was often shut down to cool down the system and again the application was re-launched. But every time the solver was re-launched, the case file in .cas format and the data files in .dat.gz format, both corresponding to the most recent time step(flow time) had to be read. As an example, if the calculations were stopped after a time step corresponding to a flow time of 10.5 seconds and the solver was shut down, to resume the calculation after re-launching the fluent solver (standalone application), case file named FFF-1050.cdat file and data file named as FFF-10.500000.dat.gz had to be read separately. Further explanation for this can be found in **4.2.4.8.1.**

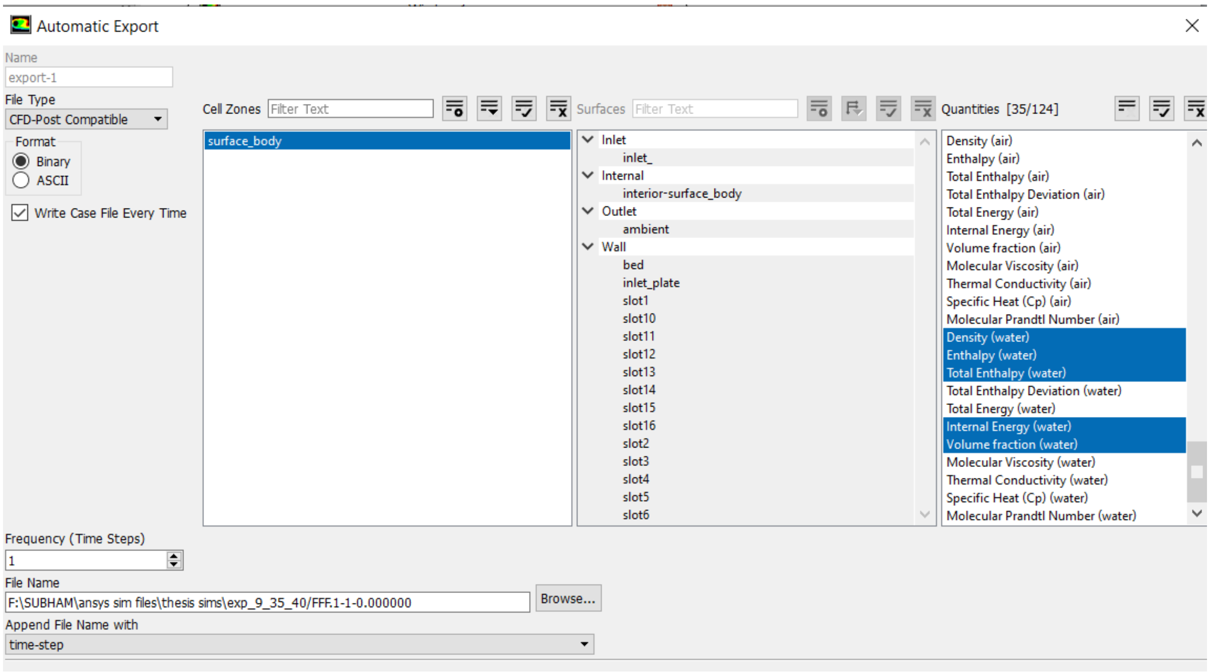
Automatic Export

Name: export-1

File Type: CFD-Post Compatible

Format: ● Binary ○ ASCII

☑ Write Case File Every Time

Cell Zones: surface_body

Quantities [35/124]

Frequency (Time Steps): 1

File Name: F:\SUBHAM\ansys sim files\thesis sims\exp_9_35_40/FFF.1-1-0.000000

Append File Name with: time-step

Fig. 4.20 Automatic Export window

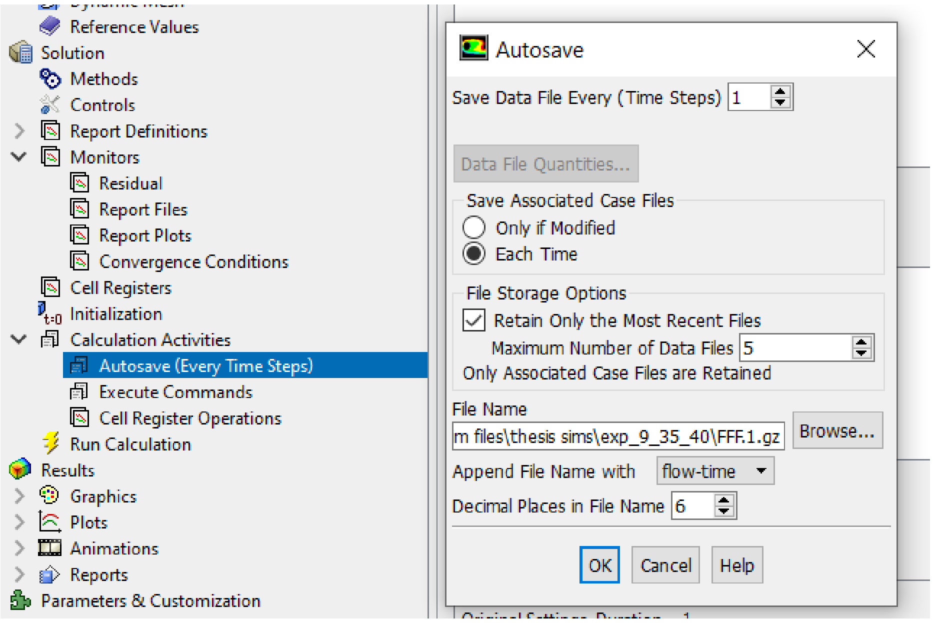
Autosave

Save Data File Every (Time Steps): 1

Save Associated Case Files: ○ Only if Modified ● Each Time

File Storage Options: ☑ Retain Only the Most Recent Files

Maximum Number of Data Files: 5

Only Associated Case Files are Retained

File Name: m files\thesis sims\exp_9_35_40\FFF.1.gz

Append File Name with: flow-time

Decimal Places in File Name: 6

Fig. 4.21 Autosave dialogue box

4.2.4.5 Creating Contours of water volume fraction

As the solution proceeds, information regarding the iterations is displayed on the console but at a very fast rate. Also, transient graphs for the scaled residuals are plotted but apart from this information, it is always advisable to graphically visualise the flow development.

So the contours of the volume fraction of phases were generated that would graphically give us the idea of the amount of water that has entered the channel in course of the calculation. This was done by opening the contours window (Fig. 4.22). Contours of "phases" was selected. "Water" was selected as the phase. All the surfaces were selected. Finally, the contours were displayed by clicking "Save and display". If all the previous setup and initialisation were done correctly, minimum and the maximum Values for the volume fraction of water would be automatically computed as 0 and 1 respectively. Fig. 4.23 shows contours of water volume fraction for a flow time of *t*=0 s and Fig. 4.24 shows contours of water volume fraction for a flow time of *t*=4.56 s.

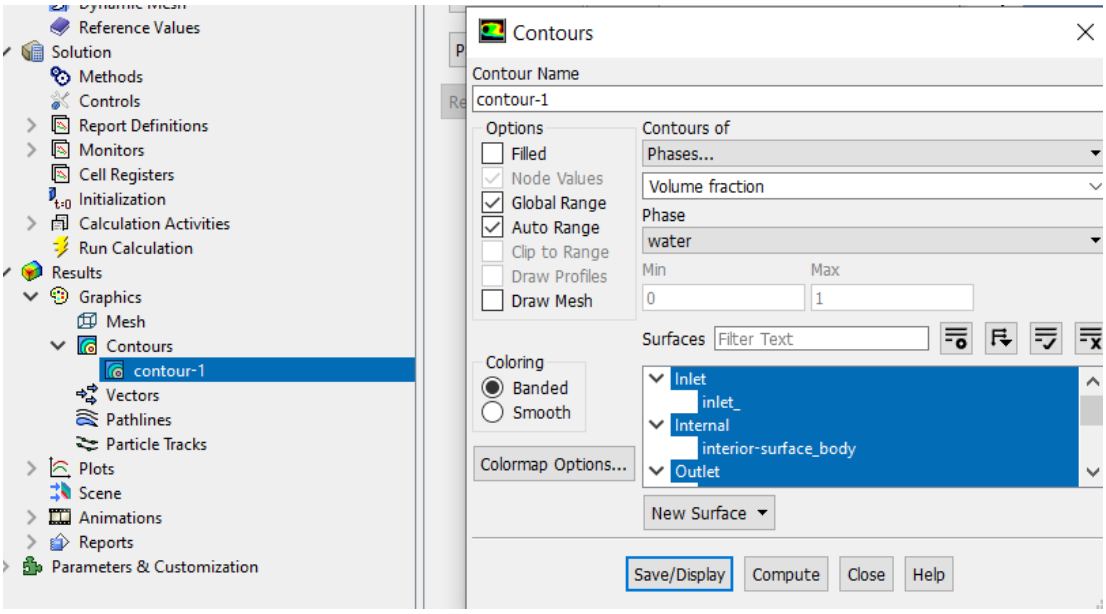

Contours

Contour Name: contour-1

Options:
☐ Filled
☑ Node Values
☑ Global Range
☑ Auto Range
☐ Clip to Range
☐ Draw Profiles
☐ Draw Mesh

Contours of: Phases...
Volume fraction

Phase: water

Min: 0
Max: 1

Surfaces: Filter Text
Inlet
inlet_
Internal
interior-surface_body
Outlet

Coloring:
● Banded
○ Smooth

Fig. 4.22 Contours dialogue box and settings for displaying contours of water volume fraction.

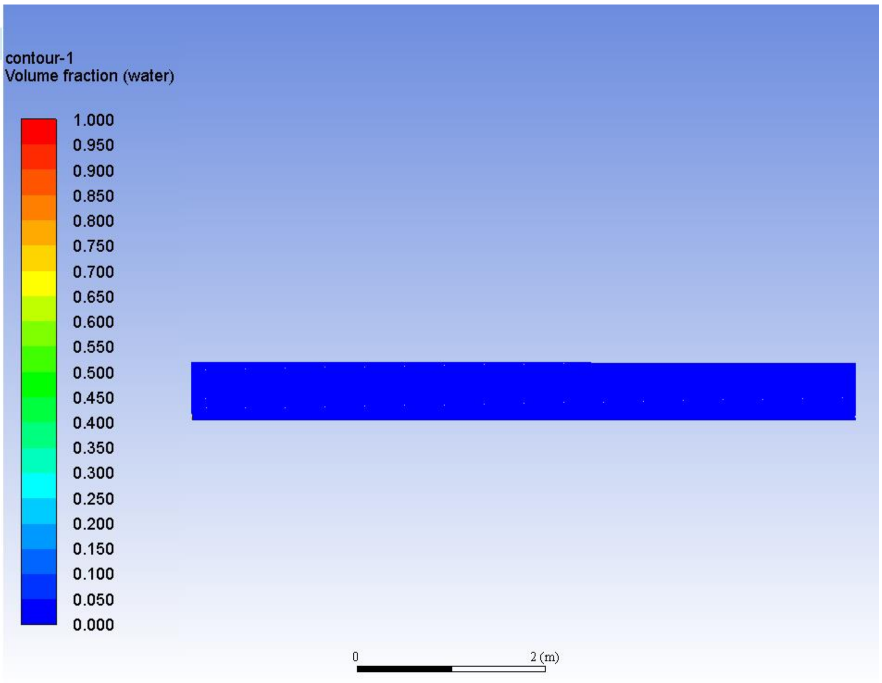

Fig. 4.23. Contours of water volume fraction at flow time *t*=0.0s

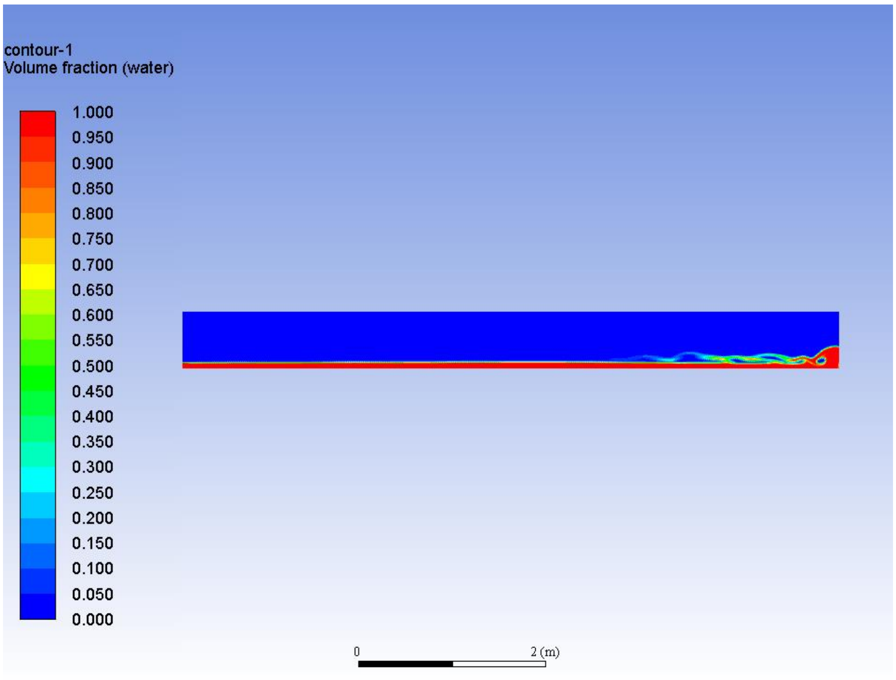

Fig. 4.24. Contours of water volume fraction at flow time *t*=4.56s

4.2.4.6 Creating solution animation

As was explained in **4.2.4.5**, it was intended to visualise the development of the flow as the calculations proceed. This was done by creating a solution animation. The “Animation definition” dialogue box (Fig. 3.25) was opened from the calculation activities in the navigation pane. Solution animation was recorded after every 1 “time step”. This interval can be increased as per the user to store fewer animation files. The animation files were stored in a specified location. The present “contour” created in the background “graphic” window was enlarged as per convenience and was captured for animation by selecting “contour-1” as the animation object and clicking “active view” in the animation definition dialogue box (window).

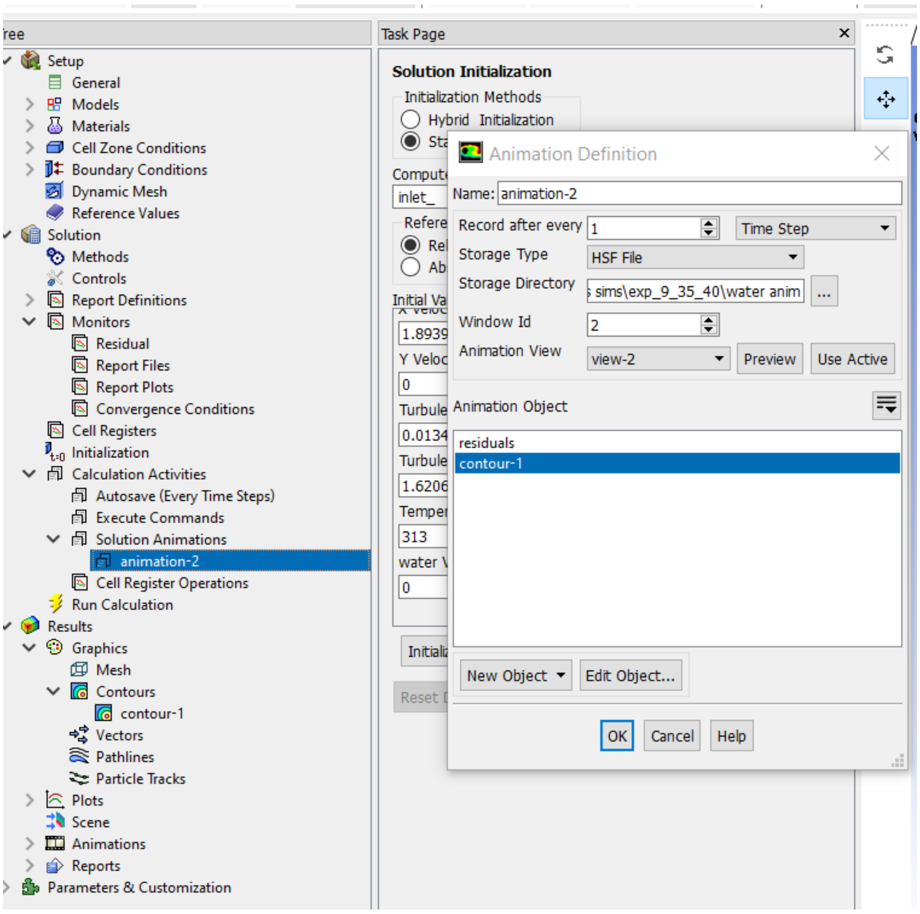

Name: animation-2
Record after every 1 Time Step
Storage Type HSF File
Storage Directory sims\exp_9_35_40\water anim
Window Id 2
Animation View view-2
Animation Object
residuals
contour-1

Fig. 4.25 “Animation definition” window and solution animation setup

4.2.4.7 Specifying the Time-Step size and Number of time steps

To specify the time step size, the number of time steps and the maximum number of iterations, the “Run Calculations” task page was opened. Even though for many of the quantities such as volume fraction, an “implicit” scheme for the solution was adopted and from literature, implicit schemes are stable even for large time steps, still the time step considered in this simulation was small enough so as to remain close to the Courant number =1.

Considering a time step of 0.01 seconds, assuming an average grid size of 0.01 m and inlet velocity of 1.89 m/s, the Courant number was found to be 1.89.

Initially, the calculations were carried out for 500 to 600 time steps i.e. a flow time of 5 seconds to 6 seconds till the water reached the tailgate and got obstructed.

A maximum of 300 iterations per time steps were considered but it was found that the solutions converged much earlier. So after a few time steps, 200 numbers of iterations were considered. Reporting intervals and profile update intervals were both kept at 20.

4.2.4.8 Calculation of flow

4.2.4.8.1 Calculating the flow with hydraulic jump

Once the calculations were run, the flow begin to develop till it reached the tailgate. Tailgate was initially fully closed i.e. all the slots were set to the “wall boundary” type as was discussed in **section 4.2.3.4.1**. The flow got reversed and water started accumulating at the tailgate. Calculations were carried out for a few more time steps (70 to 80) with these boundary conditions till water accumulated sufficiently.

Now the calculations were stopped by clicking “stop at the end of time step”. The boundary condition for the first slot (bottom most), slot 1, was changed (using Boundary Conditions task page) from “wall” to “pressure outlet”. Selecting “mixture” in the phase drop-down list for this slot1, the temperature for this slot was also changed to ambient temperature.

Then the calculation was resumed for a few more time steps, say 50.

This was done to approximately simulate the effect of raising the tailgate to a height of (dimension of the slot) and letting the flow stabilise.

In the actual practical experiments, the tailgate can be raised gradually or lowered keeping the flow running, as per our wish to form the hydraulic jump. To simulate the exact effect in Ansys fluent would be very similar to an attempt to change the boundary condition of a certain portion of the tailgate from wall to pressure outlet while the calculation (flow) is running. Achieving this was found to be very difficult and so an approximate approach was adopted in the following manner:

- The lower portion of the tailgate was splitted into very small parts(Slots), as explained in **4.2.1**.
- The boundary type for all the slots was initially set to “wall” as explained in section **4.2.3.4.1.**
- After the flow was developed and obstructed by the tailgate and sufficient water was accumulated in front of the tailgate, the calculation was stopped. The boundary condition of slot1 was changed from “wall” to “pressure outlet”. The temperature was assigned to the ambient temperature for this boundary zone (slot 1)
- Calculations were resumed for a few time steps – 40 or 50 i.e. for a flow time of 0.4s or 0.5s. This approximately simulated the effect of raising the tailgate gradually up to a height of 0.00625 m.
- The flow was stopped again, the boundary condition of slot2 was now changed from “wall” to “pressure outlet” and the temperature was changed to the ambient temperature. The calculation was resumed for further few time steps – 40 or 50. This approximately simulated the effect of raising the tailgate gradually up to a height of 0.0125 m.
- The same procedure was continued till slot12 after which it was observed that the sequent depth of the jump reduced than what was intended. So boundary condition of slot12 was reverted back to “wall” and calculations were continued till the intended sequent depth was regained.
- The depth of the water at any point was checked by “creating” “line/rake” using the “surface” menu. In the “Line/Rake” surface window, “Select point with mouse” was clicked. Right-clicking at any point on the free surface of the water displayed the coordinates of the point in the “Line/Rake” window. The y-coordinate value was taken as the depth of the water at that point.
- The hydraulic jump was obtained much earlier i.e for a flow time of about 11 seconds and in some instances, 13 seconds but the toe of the jump tended to move upstream.
- Slot 11 and slot 10 were closed and opened alternatively to obtain a more or less stable location of the jump toe.
- At any point in time, if the entire fluent solver had to be shut down due to the computer getting overheated, the calculations were resumed from the last updated solution as follows:
    - The “Fluent” solver was re-launched.
    - Case file in .cas format corresponding to the last time step/flow-time, in which the calculation was stopped, was read.
    - The corresponding data file in .dat.gz format was read. No other format of the data file could be read by the Fluent solver.
    - Desired values of time step size, number of time steps and maximum number of iterations were entered and the calculations were resumed.

4.2.4.8.2 Calculating the flow with a different ambient temperature

For simulating the hydraulic jump with another ambient temperature following methods were adopted:

- “Fluent” solver application was opened and the .cas file corresponding to the “0” time step/flow time of the previous simulation with the previous ambient temperature was “read”.
- The .dat.gz file corresponding to the “0” time step/flow time of the same previous simulation was “read”. This step and the above step automatically imported the original geometry, mesh and the problem setup.
- From the navigation panel, the “boundary conditions” task page was opened.
- Temperature for all the boundary “zones” - “ambient”, “bed”, “inlet plate”, “tailgate”, and “all slots” of the tailgate were changed to the current desired ambient temperature.
- The calculation activities task page was opened and the automatic export was “edited” to change the location of the case and data files. All other selections were kept unchanged.
- Navigating to the “solution animation” window, the location for the solution animation file was changed.
- The solution was calculated as explained earlier in section **4.2.4.8.1**.

4.2.4.8.3 Calculating the flow without hydraulic jump

For each ambient temperature, a separate flow was simulated without creating a hydraulic jump. This was achieved by opening quite a number of slots, (10 or 11) from the bottom. This is similar to the effect of raising the tailgate to a height of m. Since the water depth at the inlet was about 0.056 m, the water just passed through the tailgate opening on the other side without obstruction. This was done to study the heat transfer (heat loss) from water only due to convection and to compare this result with the heat transfer occurring with the hydraulic jump.

The steps are very similar as explained in **section 4.2.4.8.1** except for the fact that, at the beginning of the simulation, about 10 to 11 slots were opened i.e. their boundary type was changed from “wall” to “pressure outlet”. Also, the simulation was run at a stretch for a flow time of about 7 to 8 seconds as there was no requirement to stop the simulation for changing the boundary conditions for slots.

4.2.5 Post Processing

Post-processing of the results of the calculations was done using the “CFD-Post” application of Ansys fluent.

For the flows involving hydraulic jump, two sections were considered-one section just downstream of the inlet of the flume and one section downstream of the hydraulic jump. Averaged quantities-temperature, specific enthalpy, and specific entropy was measured in a tabulated form. Froude numbers in these two sections were also measured. These were achieved in the following manner:

4.2.5.1 Creating contours of water volume fraction.

- “.cdat” file corresponding to the final flow time (or any desired flow time) was opened by clicking “load results” from the file menu.
- “Contours” of water volume fraction were created from the toolbar. During generation of contours:
    - From the “domain” drop-down list, “all files corresponding to the specified flow time” was selected.
    - “Symetry1” was selected from the drop-down list of “location”.
    - From the “variable” drop-down list, “water volume fraction” was browsed.
    - The range was kept at its default selection of “Global”
    - 200 Number of contours were taken.

Fig. 4.26a and Fig. 4.26b show the contour of water volume fraction with and without hydraulic jump respectively, corresponding to a flow time of 12.10 seconds and ambient temperature of 35ºC, generated with the above settings respectively. Fig. 4.27 shows the task window for setting the contours of water volume fractions.

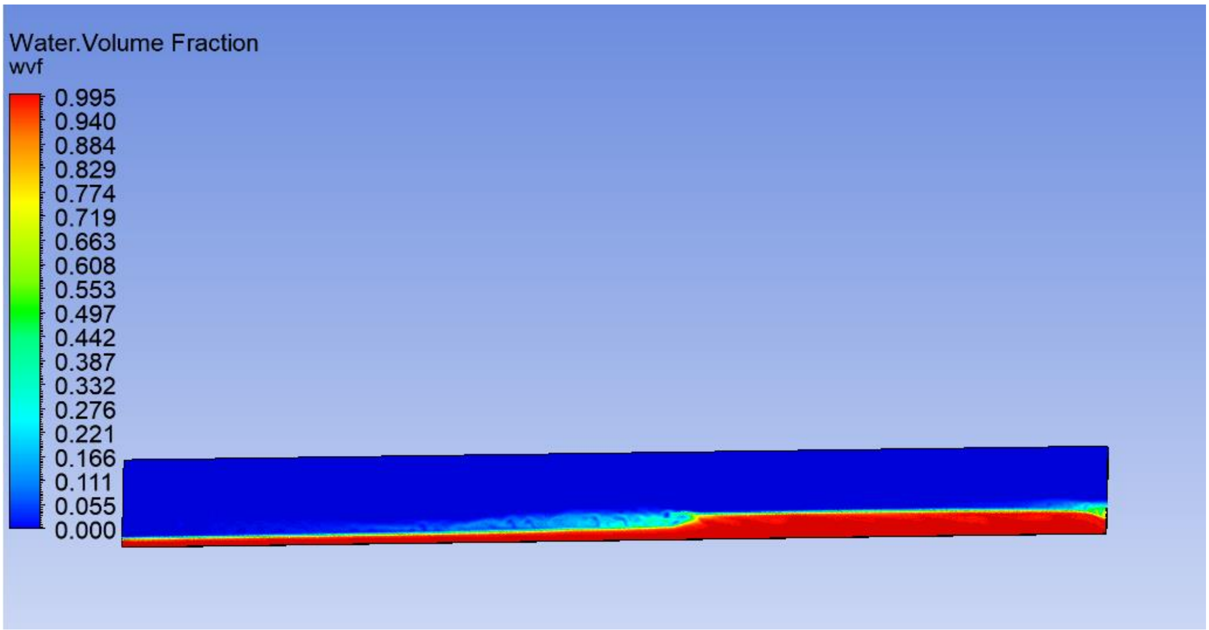

Fig. 4.26a Contours of water volume fraction for flow-time=2.10s and ambient temperature=35°C

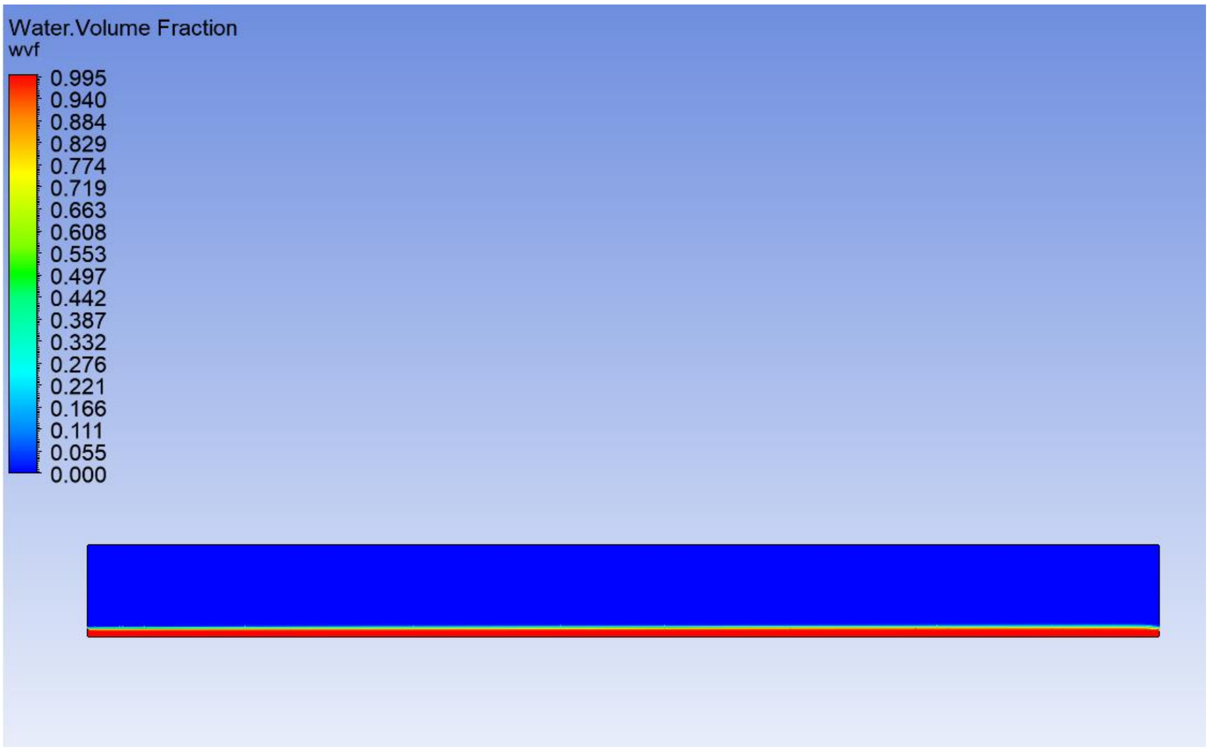

Fig. 4.26b Contours of water volume fraction for flow-time=2.10s and ambient temperature=35°C

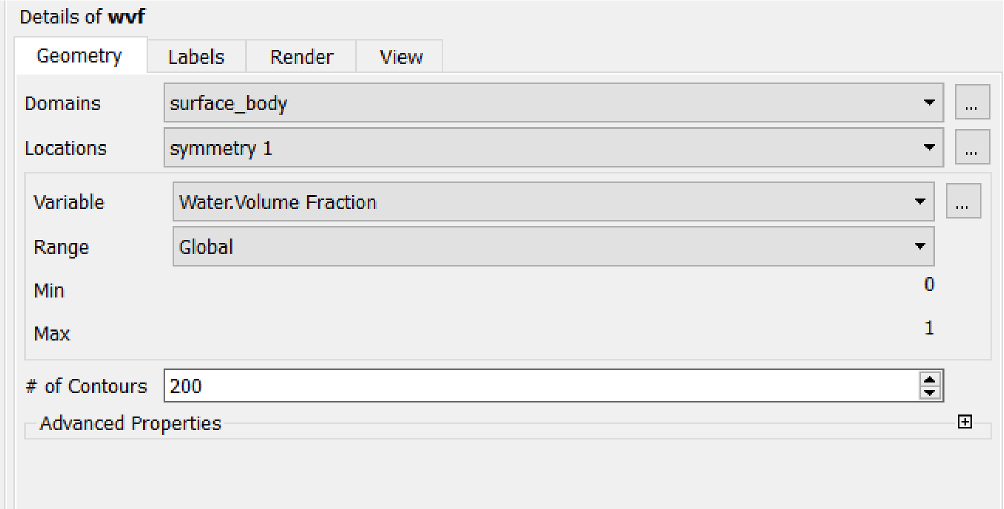
Details of **wvf**

Domains surface_body

Locations symmetry 1

Variable Water.Volume Fraction

Range Global

Min 0

Max 1

# of Contours 200

Fig. 4.27 Settings for contours of water volume fraction for flow-time=2.10s and ambient temperature=35°C

4.2.5.2 Creating the sections

In order to create the two sections, we needed to determine the coordinates of the endpoints of each of the sections. After determining the coordinates of the endpoints of a section, a line was created between these two points to create the section. To determine the coordinates of the upper-end point, the “probe” tool was used. The upper-end point was chosen to be somewhere within the air-water interface.

For generating a section i.e. section 1 near the inlet gate opening of the flume,

- a point within the air-water interface was probed for its x and y coordinates (Fig. 4.28).
- “Line” command was invoked from the “location” tool and it was “named” as “section 1” (for example).
- Then appropriate domain was selected. “Two Points” “method” was selected.
- For “point 2”, the probed values for x and y coordinates were entered. Value for “z” co-ordinate was entered as “0”.
- Since the slope of the bed was very small, the cross-sections can be assumed to be vertical. So for “point 1” (the bottom end point of the section), the same x-value of the “point2” was entered.
- A common value of 0.01 m for y-coordinate for “point 1” for all the sections was determined depending upon the bed slope. The z-value was 0.
- Once this section 1 was created for a single simulation, it was not necessary to create this section for other simulations because this section was used to determine average inlet quantities of the flow and these values remain the same for all other simulations. Only section 2 was created for other simulations.

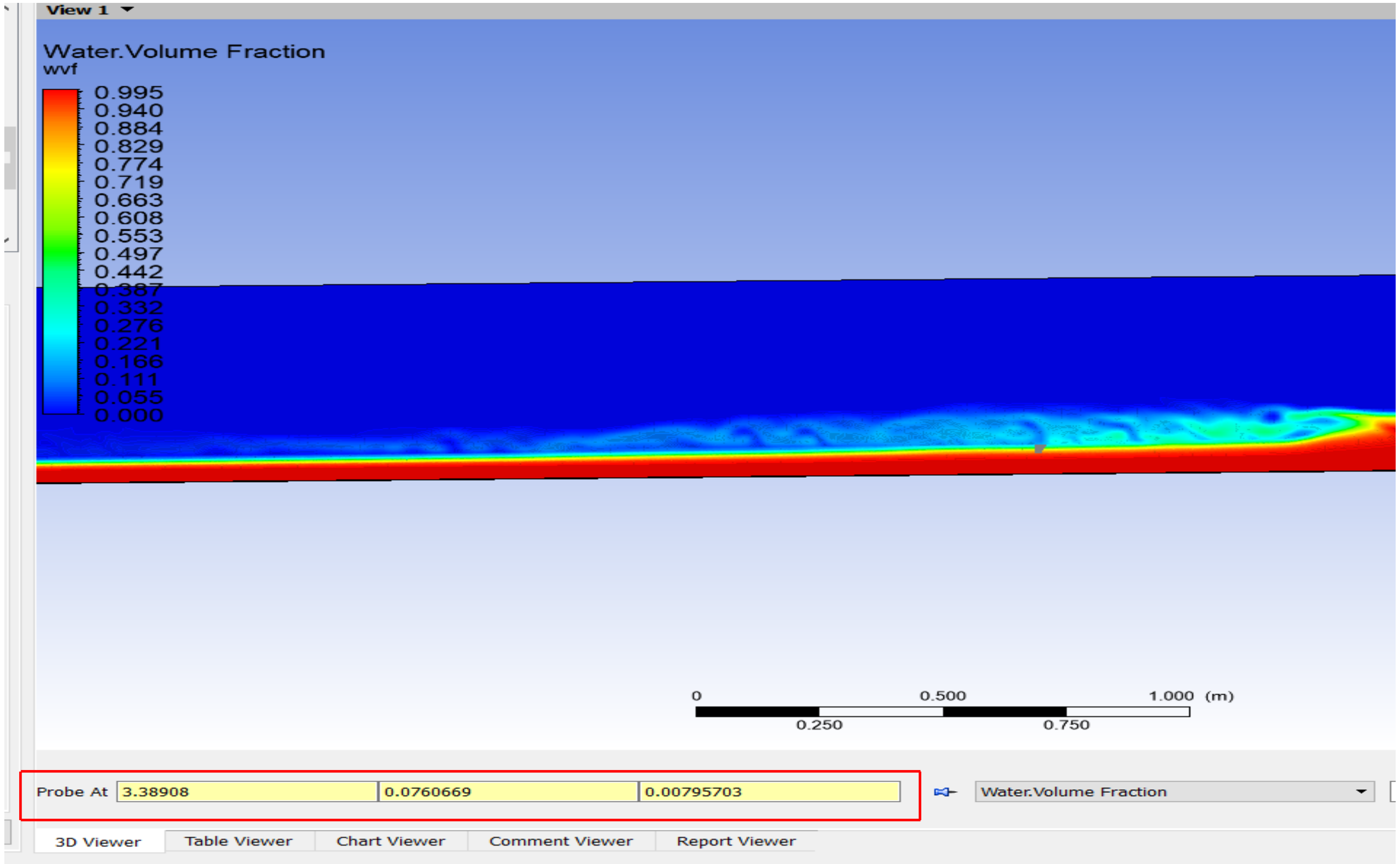

Probe At 3.38908 0.0760669 0.00795703

Fig. 4.28 The point "probed" at the toe of the jump for contours of water volume fraction for flow-time=2.10s and ambient temperature=35ºC. Co-ordinates of the point are shown within the red box

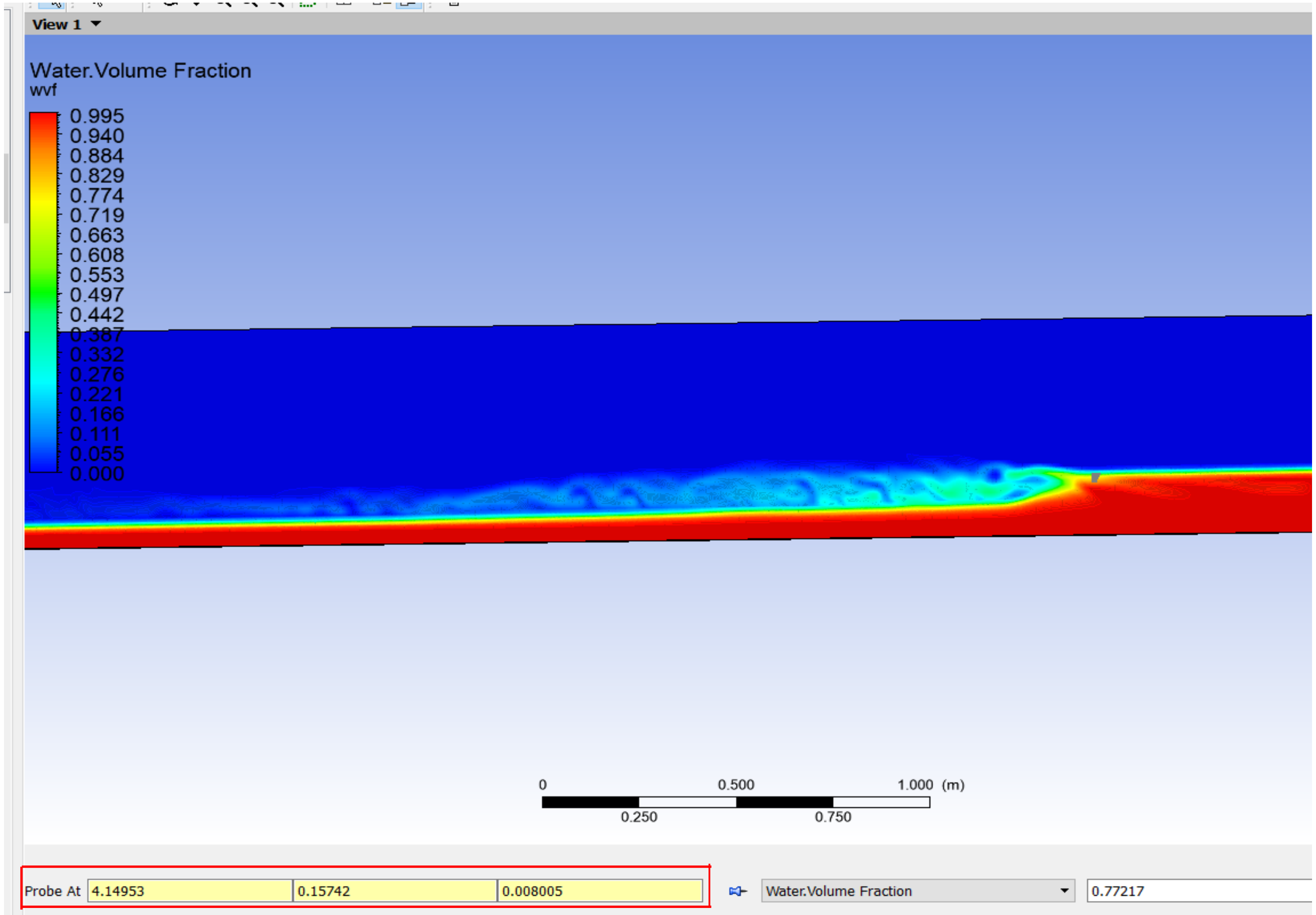

Probe At 4.14953 0.15742 0.008005

Water.Volume Fraction 0.77217

Fig. 4.29 The point "probed" downstream the jump for contours of water volume fraction for flow-time=2.10s and ambient temperature = 35ºC. Co-ordinates of the point are shown within the red box.

Similar steps were followed for creating a section 2 (that was named as post jump section) downstream hydraulic jump. Fig. 4.29 shows the probed point that was considered the upper-end point of the section.

4.2.5.3 Generating the table for thermal quantities averaged across the sections.

A table was created using the “table” tool. Rows and columns were named appropriately as shown in Fig. 4.20. For obtaining the average temperature across section 1 (pre-jump section),

- Clicking on the appropriate cell, the “CFD-post” “function” was selected from the “insert” ribbon. From the CFD-post selection toolbox, “lenghAve” was selected.
- From “Variable”, “Temperature” was selected.
- From “Location”, “inlet section” was selected
- Alternatively, the following command was typed in the command/formula box of the table, to get the average temperature in section 1:

  =lengthAve(Temperature)@inlet section.

The values of average temperature, specific enthalpy, and specific entropy were the same in section1 for all the simulations. So these values were evaluated only for one simulation.

Similar steps were followed to obtain average values of specific entropy and specific enthalpy in section2 for all other simulations.

For each of the flows in which hydraulic jumps were not allowed to form deliberately, similar steps were followed as explained in **sections 4.2.5.1, 4.2.5.2 and 4.2.5.3. S**ection 2, in this case, was taken at the same locations as was taken for the corresponding simulation with the same ambient temperature.

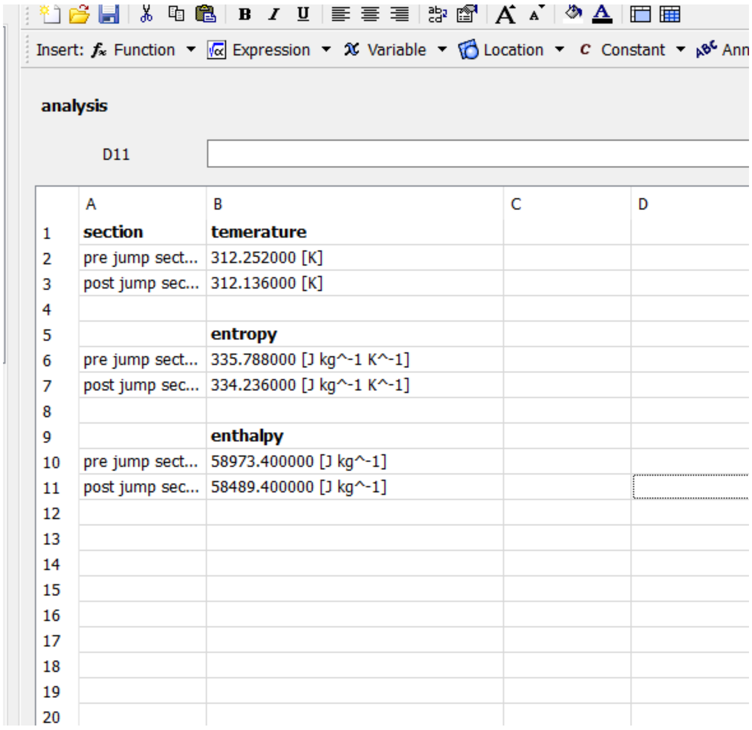

	A	B	C	D
1	**section**	**temerature**		
2	pre jump sect...	312.252000 [K]		
3	post jump sec...	312.136000 [K]		
4				
5		**entropy**		
6	pre jump sect...	335.788000 [J kg^-1 K^-1]		
7	post jump sec...	334.236000 [J kg^-1 K^-1]		
8				
9		**enthalpy**		
10	pre jump sect...	58973.400000 [J kg^-1]		
11	post jump sec...	58489.400000 [J kg^-1]		
12				
13				
14				
15				
16				
17				
18				
19				
20				

Fig. 4.30. Table with averaged temperature, specific entropy and specific enthalpy across the two sections.

CHAPTER 5

5.1 Results and Discussion

All the simulations were carried out considering the inlet water temperature to be fixed at 40ºC. Six different ambient temperatures were considered for the six simulations. The ambient temperatures were 10ºC, 15ºC, 20ºC, 25ºC, 30ºC and 35ºC. The mass flow rate for all three simulations was kept constant at 106 kg/s resulting in a constant inlet velocity of 1.893 m/s. A stable hydraulic jump was obtained for a tailgate opening of either 0.062 m (i.e. for all 10 slots open) or 0.068 m (i.e. for all 11 slots open). The depth of the supercritical flow was 0.056 m for all cases and the sequent depth was found to be within the range of 0.16m to 0.15. Inlet Froude number for all the simulations was 2.55. The change in temperature, specific enthalpy and specific entropy were observed as discussed in the following sections:

5.1.1 Simulation 1

The ambient temperature was set to 10ºC. The Froude number corresponding to the sequent depth was found to be 0.565. The data for the simulation with a hydraulic jump is presented in **5.1.1.1** and the data for the simulation without the formation of a hydraulic jump is presented in **5.1.1.2**. Section 2 (section downstream the hydraulic jump) was named as Post jump section and was taken at the same for both the simulations.

5.1.1.1 Simulation 1 (with a hydraulic jump)

The following table shows the average temperature, specific entropy, and specific enthalpy at the section downstream of the hydraulic jump (post jump section):

Table 5.1 - Average temperature, specific enthalpy, specific entropy at inlet section and Section 2 for the flow with a hydraulic jump for 10ºC ambient temperature.

Sl no.	Flow Property	Section 1 (Inlet Jump Section)	Section 2 (Post Jump Section)	Difference $\Delta T_{j1}= T_0- T_{j1}$ $\Delta h_{j1}= h_0- h_{j1}$ $\Delta s_{j1}= s_0- s_{j1}$
1	Temperature	T_0 = 40ºC	T_{j1} = 38.278ºC	ΔT_{j1}= 1.722 ºC
2	Specific enthalpy	h_0 = 62093.330 J/kg	h_{j1} = 55526.900 J/kg	Δh_{j1}= 6566.4 J/kg
3	Specific entropy	s_0 = 345.767 J/kg-K	s_{j1} = 324.730 J/kg-K	Δs_{j1}= 21.037 J/kg-K

5.1.1.2 Simulation 1 (without hydraulic jump)

The following table represents the average temperature, specific entropy, and specific enthalpy at the section, at the same location, for the flow without the hydraulic jump.

Table 5.2 - Average temperature, specific enthalpy, specific entropy at inlet section and Section 2 for the flow without hydraulic jump for 10ºC ambient temperature.

Sl no.	Flow Property	Section1 (Inlet Jump Section)	Section2 (Post Jump Section)	Difference $\Delta T_1 = T_0 - T_1$ $\Delta h_1 = h_0 - h_1$ $\Delta s_1 = s_0 - s_1$
1	Temperature	T_0 = 40ºC	T_1 =38.409ºC	ΔT_1 =1.591ºC
2	Specific Enthalpy	h_0 = 62093.330 J/kg	h_1 =56076.5 J/kg	Δh_1 =6016.83 J/kg
3	Specific Entropy	s_0 = 345.767 J/kg-K	s_1 =326.497 J/kg-K	Δs_1 =19.27 J/kg-K

It can be observed that the drop in temperature from the inlet section to the Section 2, with the hydraulic jump was, ΔT_{j1}= 1.722ºC and the temperature drop due to only convective, other modes of heat loss from water and without hydraulic jump effects was, ΔT_1 =1.591ºC. So there was an increase of 8.234% in temperature drop in water due to the hydraulic jump.

Specific enthalpy drop, Δh_{j1}= 6566.4 J/kg was observed with the hydraulic jump. Specific enthalpy drop without hydraulic jump was found to be Δh_1 =6016.83 J/kg. So there is an enhancement of drop-in specific enthalpy with a hydraulic jump by 9.134%.

Drop-in specific entropy with the hydraulic jump was Δs_{j1}= 21.037 J/kg-K and without a hydraulic jump, the specific entropy was Δs_1 =19.27 J/kg-K. Thus the hydraulic jump resulted in an increase in the drop of specific entropy by 9.169%.

5.1.2 Simulation 2

The ambient temperature was set to 15ºC. The Froude number corresponding to the sequent depth was found to be 0.585. The data for the simulation with a hydraulic jump is presented in **5.1.2.1** and the data for the simulation without the formation of a hydraulic jump is presented in **5.1.2.2**. Section 2 (section downstream the hydraulic jump) was named as Post jump section and was taken at the same for both the simulations.

5.1.2.1 Simulation 2 (with hydraulic jump)

The following table shows the average temperature, specific entropy, and specific enthalpy at the section downstream of the hydraulic jump (post jump section):

Table 5.3 - Average temperature, specific enthalpy, specific entropy at inlet section and Section 2 for the flow with the hydraulic jump for 15°C ambient temperature.

Sl no.	Flow Property	Section 1 (Inlet Jump Section)	Section 2 (Post Jump Section)	Difference $\Delta T_{j2}= T_0- T_{j2}$ $\Delta h_{j2}= h_0- h_{j2}$ $\Delta s_{j2}= s_0- s_{j2}$
1	Temperature	T_0 = 40ºC	T_{j2} = 38.510°C	ΔT_{j2}= 1.49°C
2	Specific Enthalpy	h_0 = 62093.330 J/kg	h_{j2} = 56527.3 J/kg	Δh_{j2}= 5566.03 J/kg
3	Specific Entropy	s_0 = 345.767 J/kg-K	s_{j2} = 327.943J/kg-K	Δs_{j2}= 17.824 J/kg-K

5.1.2.2 Simulation 2 (without hydraulic jump)

The corresponding average temperature, specific entropy and specific enthalpy at the section for the flow without hydraulic jump are represented below:

Table 5.4 - Average temperature, specific enthalpy, specific entropy at inlet section and Section 2 for the flow without hydraulic jump for 15ºC ambient temperature.

Sl no.	Flow Property	Section 1 (Inlet Jump Section)	Section 2 (Post Jump Section)	Difference $\Delta T_2= T_0- T_1$ $\Delta h_2= h_0- h_1$ $\Delta s_2= s_0- s_1$
1	Temperature	T_0 = 40ºC	T_2 =38.636ºC	ΔT_2=1.364ºC
2	Specific Enthalpy	h_0 = 62093.330 J/kg	h_2 =57025.1 J/kg	Δh_2=5068.23 J/kg
3	Specific Entropy	s_0 = 345.767 J/kg-K	s_2 =329.542 J/kg-K	Δs_2 =16.225 J/kg-K

It was observed that the drop in temperature with the hydraulic jump was ΔT_{j2}= 1.49ºC while the drop in temperature with only heat loss due to conduction and convection without considering the hydraulic jump was ΔT_2=1.364ºC. Thus the hydraulic jump enhanced the temperature drop by 9.23%.

A decrease in specific enthalpy with the hydraulic jump was found to be Δh_{j2}= 5566.03 J/kg whereas the decrease in specific enthalpy without the hydraulic jump was Δh_2=5068.23 J/kg. An increase of 9.822% in specific enthalpy drop due to the hydraulic jump was observed.

The drop in specific entropy with the hydraulic jump was Δs_{j2}= 17.824 J/kg-K and the drop in specific entropy without considering the hydraulic jump was Δs_2 =16.225 J/kg-K. Thus the hydraulic jump enhanced the drop in enthalpy by 9.855%.

5.1.3 Simulation 3

The ambient temperature was set to 20ºC. The Froude number corresponding to the sequent depth was found to be 0.543. The data for the simulation with a hydraulic jump is presented in **5.1.3.1** and the data for the simulation without the formation of a hydraulic jump is presented in **5.1.3.2**. Section 2 (section downstream the hydraulic jump) was named as Post jump section and was taken at the same for both the simulations.

5.1.3.1 Simulation 3 (with hydraulic jump)

The following table shows the average temperature, specific entropy, and specific enthalpy at the section downstream of the hydraulic jump (post jump section):

Table 5.5 - Average temperature, specific enthalpy, specific entropy at inlet section and Section 2 for the flow with a hydraulic jump for 20ºC ambient temperature.

Sl no.	Flow Property	Section 1 (Inlet Jump Section)	Section 2 (Post Jump Section)	Difference $\Delta T_{j3} = T_0 - T_{j3}$ $\Delta h_{j3} = h_0 - h_{j3}$ $\Delta s_{j3} = s_0 - s_{j3}$
1	Temperature	T_0 = 40 ºC	T_{j3} = 38.721ºC	ΔT_{j3}= 1.279 ºC
2	Specific Enthalpy	h_0 = 62093.330 J/kg	h_{j3} = 57385.9 J/kg	Δh_{j3} = 4707.43 J/kg
3	Specific Entropy	s_0 = 345.767 J/kg-K	s_{j3} = 330.699 J/kg-K	Δs_{j3} = 15.068 J/kg-K

5.1.3.2 Simulation 3 (without hydraulic jump)

The corresponding average temperature, specific entropy and specific enthalpy at the section for the flow without hydraulic jump are represented below:

Table 5.6 - Average temperature, specific enthalpy, specific entropy at inlet section and Section 2 for the flow without hydraulic jump for 20ºC ambient temperature.

Sl no.	Flow Property	Section 1 (Inlet Jump Section)	Section 2 (Post Jump Section)	Difference $\Delta T_3 = T_0 - T_3$ $\Delta h_3 = h_0 - h_3$ $\Delta s_3 = s_0 - s_3$
1	Temperature	T_0 = 40ºC	T_3 = 38.812ºC	ΔT_3 = 1.188ºC
2	Specific enthalpy	h_0 = 62093.330 J/kg	h_3 =57721.53 J/kg	Δh_3 = 4011.93 J/kg
3	Specific entropy	s_0 = 345.767 J/kg-K	s_3 = 331.932 J/kg-K	Δs_3 = 13.835 J/kg-K

In this simulation, the observed temperature drop with a hydraulic jump was ΔT_{j3}= 1.279 ºC and without the hydraulic jump was ΔT_3 = 1.122ºC. The hydraulic jump resulted in a 7.66% increase in temperature drop.

A decrease in specific enthalpy with the hydraulic jump was found to be Δh_{j3} = 4707.43 J/kg and without the hydraulic jump, the enthalpy decrease was Δh_3 = 5043.03 J/kg. The increase in specific enthalpy drop due to hydraulic jump was 8.36%.

A decrease in specific entropy with the hydraulic jump was found to be Δs_{j3} = 15.068 J/kg-K and without the hydraulic jump, the enthalpy decrease was Δs_3 = 13.835 J/kg-K. The increase in specific enthalpy drop due to hydraulic jump was 8.91%.

5.1.4 Simulation 4

The ambient temperature was set to 25ºC. The Froude number corresponding to the sequent depth was found to be 0.551. The data for the simulation with the hydraulic jump is presented in **5.1.4.1** and the data for the simulation without the formation of the hydraulic jump is presented in **5.1.4.2**. Section 2(section downstream the hydraulic jump) was named as Post jump section and was taken at the same for both the simulations.

5.1.4.1 Simulation 4 (with hydraulic jump)

The following table shows the average temperature, specific entropy, and specific enthalpy at the section downstream of the hydraulic jump (post jump section):

Table 5.7 - Average temperature, specific enthalpy, specific entropy at inlet section and Section 2 for the flow with the hydraulic jump for 25ºC ambient temperature.

Sl no.	Flow Property	Section 1 (Inlet Jump Section)	Section 2 (Post Jump Section)	Difference $\Delta T_{j4} = T_0 - T_{j4}$ $\Delta h_{j4} = h_0 - h_{j4}$ $\Delta s_{j4} = s_0 - s_{j4}$
1	Temperature	T_0 = 40 ºC	T_{j4} = 39.096ºC	ΔT_{j4}= 0.904 ºC
2	Specific enthalpy	h_0 = 62093.330 J/kg	h_{j4} = 58862.8 J/kg	Δh_{j4}= 3230.53 J/kg
3	Specific entropy	s_0 = 345.767 J/kg-K	s_{j4} = 335.432 J/kg-K	Δs_{j4}= 10.335 J/kg-K

5.1.4.2 Simulation 4 (without hydraulic jump)

The corresponding average temperature, specific entropy and specific enthalpy at the section for the flow without hydraulic jump are represented below:

Table 5.8 - Average temperature, specific enthalpy, specific entropy at inlet section and Section 2 for the flow without hydraulic jump for 25ºC ambient temperature.

Sl no.	Flow Property	Section1 (Inlet Jump Section)	Section2 (Post Jump Section)	Difference $\Delta T_4 = T_0 - T_4$ $\Delta h_4 = h_0 - h_4$ $\Delta s_4 = s_0 - s_4$
1	Temperature	T_0 = 40º C	T_4 = 39.129ºC	ΔT_4= 0.871 ºC
2	Specific enthalpy	h_0 = 62093.330 J/kg	h_4 =59085.9 J/kg	Δh_4 =3007.43 J/kg
3	Specific entropy	s_0 = 345.767 J/kg-K	s_4 = 336.149 J/kg-K	Δs_4 = 9.618 J/kg-K

The observed temperature drop with the hydraulic jump was ΔT_{j4}= 0.904ºC and without the hydraulic jump was ΔT_4= 0.871ºC. The hydraulic jump resulted in a 3.788% increase in temperature drop.

A decrease in specific enthalpy with the hydraulic jump was found to be Δh_{j4}= 3230.53 J/kg and without the hydraulic jump, enthalpy decrease was Δh_4 =3007.43 J/kg. The increase in specific enthalpy drop due to hydraulic jump was 6.905 %.

A decrease in specific entropy with the hydraulic jump was found to be Δs_{j4}= 10.335 J/kg-K and without the hydraulic jump, enthalpy decrease was Δs_4 = 9.618 J/kg-K. The increase in specific enthalpy drop due to hydraulic jump was 7.454 %.

5.1.5 Simulation 5

The ambient temperature was set to 30ºC. The Froude number corresponding to the sequent depth was found to be 0.519. The data for the simulation with a hydraulic jump is presented in **5.1.5.1** and the data for the simulation without the formation of the hydraulic jump is presented in **5.1.5.2**. Section 2(section downstream the hydraulic jump) was named as Post jump section and was taken at the same for both the simulations.

5.1.5.1 Simulation 5 (with hydraulic jump)

The following table shows the average temperature, specific entropy, and specific enthalpy at the section downstream of the hydraulic jump (post jump section):

Table 5.9 - Average temperature, specific enthalpy, specific entropy at inlet section and Section 2 for the flow with the hydraulic jump for 30ºC ambient temperature.

Sl no.	Flow Property	Section 1 (Inlet Jump Section)	Section 2 (Post Jump Section)	Difference $\Delta T_{j5} = T_0 - T_{j5}$ $\Delta h_{j5} = h_0 - h_{j5}$ $\Delta s_{j5} = s_0 - s_{j5}$
1	Temperature	T_0 = 40 ºC	T_{j5} = 39.318ºC	ΔT_{j5} = 0.682 ºC
2	Specific enthalpy	h_0 = 62093.330 J/kg	h_{j5}= 59880.0 J/kg	Δh_{j5} = 2213.33 J/kg
3	Specific entropy	s_0 = 345.767 J/kg-K	s_{j5} = 338.689 J/kg-K	Δs_{j5} = 7.078 J/kg-K

5.1.5.2 Simulation 5 (without hydraulic jump)

The corresponding average temperature, specific entropy and specific enthalpy at the section for the flow without hydraulic jump are represented below:

Table 5.10 - Average temperature, specific enthalpy, specific entropy at inlet section and Section 2 for the flow with the hydraulic jump for 30ºC ambient temperature.

Sl no.	Flow Property	Section 1 (Inlet Jump Section)	Section 2 (Post Jump Section)	Difference $\Delta T_5 = T_0 - T_5$ $\Delta h_5 = h_0 - h_5$ $\Delta s_5 = s_0 - s_5$
1	Temperature	T_0 = 40ºC	T_5 = 39.34ºC	ΔT_5= 0.631ºC
2	Specific enthalpy	h_0 = 62093.330 J/kg	h_5 = 60091.9 J/kg	Δh_5 =2001.43 J/kg
3	Specific entropy	s_0 = 345.767 J/kg-K	s_5 = 339.370 J/kg-K	Δs_5 =6.397 J/kg-K

The observed temperature drop with hydraulic jump was ΔT_{j5}= 0.682ºC and without the hydraulic jump was ΔT_5= 0.659ºC. The hydraulic jump resulted in a 3.49 % increase in temperature drop.

A decrease in specific enthalpy with hydraulic jump was found to be Δh_{j5}= 2213.33 J/kg and without the hydraulic jump, enthalpy decrease was Δh_5 = 2001.43 J/kg. The increase in specific enthalpy drop due to hydraulic jump was 10.587 %.

A decrease in specific entropy with hydraulic jump was found to be Δs_{j5}= 7.078 J/kg-K and without the hydraulic jump, enthalpy decrease was Δs_5 = 6.397 J/kg-K. The increase in specific enthalpy drop due to hydraulic jump was 10.64 %.

5.1.6 Simulation 6

The ambient temperature was set to 35ºC. The Froude number corresponding to the sequent depth was found to be 0.447. The data for the simulation with the hydraulic jump is presented in **5.1.6.1** and the data for the simulation without the formation of the hydraulic jump is presented in **5.1.6.2**. Section 2 (section downstream the hydraulic jump) was named as Post jump section and was taken at the same for both the simulations.

5.1.6.1 Simulation 6 (with hydraulic jump)

The ambient temperature was set to 35ºC. The following table shows the average temperature, specific entropy, and specific enthalpy at the section downstream of the hydraulic jump (post jump section):

Table 5.11 - Average temperature, specific enthalpy, specific entropy at inlet section and Section 2 for the flow with hydraulic jump for 35ºC ambient temperature.

Sl no.	Flow Property	Section 1 (Inlet Jump Section)	Section 2 (Post Jump Section)	Difference $\Delta T_{j6}= T_0- T_{j6}$ $\Delta h_{j6}= h_0- h_{j6}$ $\Delta s_{j6}= s_0- s_{j6}$
1	Temperature	T_0 = 40 ºC	T_{j6} = 39.587 ºC	ΔT_{j6}= 0.413 ºC
2	Specific enthalpy	h_0 = 62093.330 J/kg	h_{j6}= 61003.9 J/kg	Δh_{j6}= 1089.43 J/kg
3	Specific entropy	s_0 = 345.767 J/kg-K	s_{j6} = 342.286 J/kg-K	Δs_{j6}= 3.481 J/kg-K

5.1.6.2 Simulation 6 (without hydraulic jump)

The ambient temperature was set to 35ºC. The following table shows the average temperature, specific entropy, and specific enthalpy at the section downstream of the hydraulic jump (post jump section):

Table 5.12 - Average temperature, specific enthalpy, specific entropy at inlet section and Section2 for the flow without hydraulic jump for 35ºC ambient temperature.

Sl no.	Flow Property	Section 1 (Inlet Jump Section)	Section 2 (Post Jump Section)	Difference $\Delta T_6 = T_0 - T_6$ $\Delta h_6 = h_0 - h_6$ $\Delta s_6 = s_0 - s_6$
1	Temperature	T_0 = 40ºC	T_6 = 39.608ºC	ΔT_6 = 0.392ºC
2	Specific enthalpy	h_0 = 62093.330 J/kg	h_6 = 61090.9 J/kg	Δh_6 = 1002.43 J/kg
3	Specific entropy	s_0 = 345.767 J/kg-K	s_6 = 342.566 J/kg-K	Δs_6 = 3.201 J/kg-K

The observed temperature drop with the hydraulic jump was ΔT_{j6}= 0.682ºC and without the hydraulic jump was ΔT_6= 0.631ºC. The hydraulic jump resulted in a 5.085 % increase in temperature drop.

A decrease in specific enthalpy with the hydraulic jump was found to be Δh_{j6}= 1089.43 J/kg and without the hydraulic jump, enthalpy decrease was Δh_6 = 1002.43 J/kg. The increase in specific enthalpy drop due to hydraulic jump was 8.679 %.

A decrease in specific entropy with the hydraulic jump was found to be Δs_{j6}= 3.481 J/kg-K and without the hydraulic jump, enthalpy decrease was Δs_6 = 3.201 J/kg-K. The increase in specific enthalpy drop due to hydraulic jump was 8.747 %.

5.1.7 Comparison of Temperature, specific enthalpy and specific entropy drop

5.1.7.1 Temperature drop

For all the simulations, ΔT_{jk} denotes, the temperature drop occurring with the hydraulic jump in the kth simulation while ΔT_k is the corresponding temperature drop occurring without the hydraulic jump in the kth simulation.

For simulation 1 with an ambient temperature of 10ºC, ΔT_{j1}=1.722ºC and ΔT_1=1.591ºC. So, an increase of 0.131ºC in temperature drop due to hydraulic jump was observed.

In simulation 2 with an ambient temperature of 15ºC, ΔT_{j2}=1.49ºC and ΔT_2=1.364ºC. The increase in temperature drop due to the hydraulic jump was 0.126ºC.

In simulation 3, ambient temperature was 20ºC and ΔT_{j3}=1.49ºC and ΔT_3 =1.364ºC. An increase in temperature drop due to hydraulic jump was observed to be 0.091ºC.

In simulation 4, ambient temperature was 25ºC and ΔT_{j4}=0.904ºC and ΔT_4 =0.871ºC. An increase in temperature drop due to hydraulic jump was observed to be 0.033ºC.

In simulation 5, ambient temperature was 30ºC and ΔT_{j5}=0.682ºC and ΔT_5 =0.631ºC. An increase in temperature drop due to hydraulic jump was observed to be 0.023ºC.

In simulation 6 with the ambient temperature of 35ºC and ΔT_{j6}=0.682ºC and ΔT_6 =0.631ºC, the observable increase in temperature drop with the hydraulic jump was 0.021ºC.

Considering only the average temperature of flow across section 2, it was observed that this temperature increased with an increase in ambient temperature (Fig. 5.1).

Without any hydraulic jump, this temperature also increases with the ambient temperature simply because of the reduced heat transfer rate owing to decreasing temperature difference between the water and the ambient (Fig. 5.1). The variation of ΔT_{jk} and ΔT_k with ambient temperature is plotted in Fig. 5.2.

Fig. 5.3 shows the variation of the increase in temperature drops with the ambient temperature. It was observed that the increase in temperature drop, occurring due to the effect of hydraulic jump decreased with the increase in ambient temperature or with the decrease in temperature difference between the water and the ambient. The drop in temperature for 10ºC ambient temperature was slightly greater than the drop in temperature for 15ºC ambient. There was a sharp decrease in the improvement of temperature drop due to hydraulic jump after 15ºC ambient temperature and the rate of decrease in the improvement of temperature drop became lesser at 25ºC and still lesser at 30ºC and 35ºC.

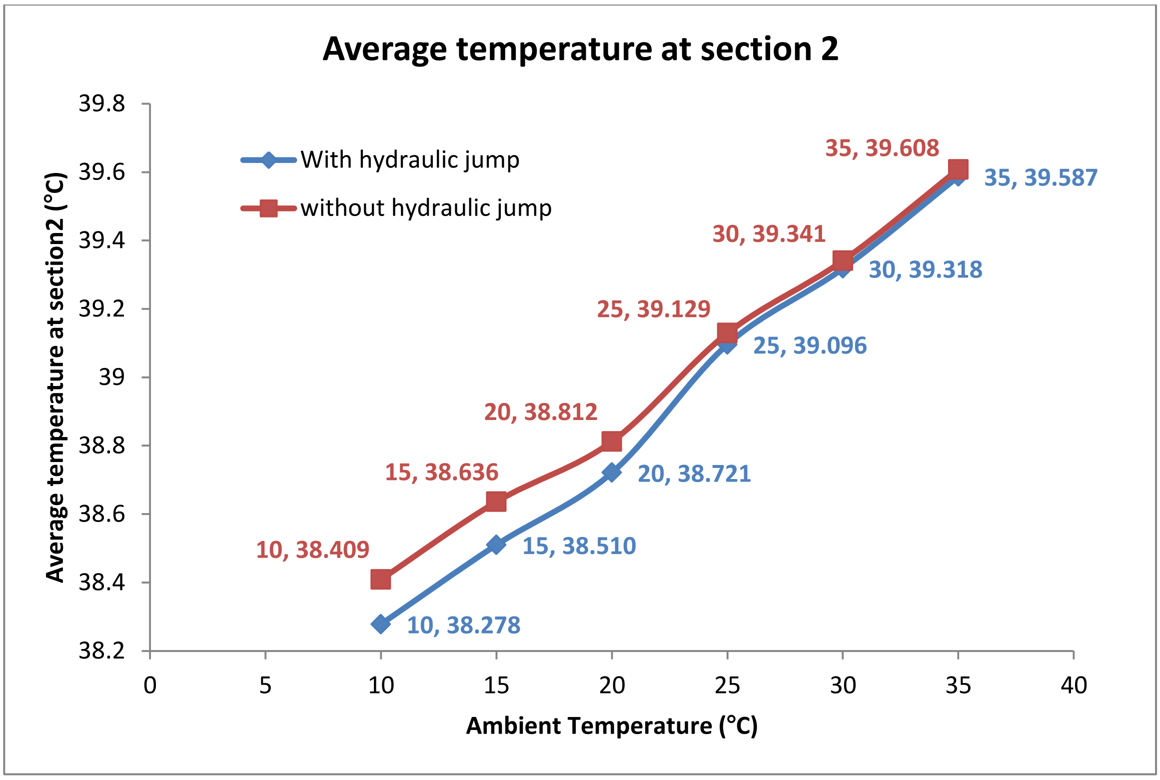

Fig. 5.1 Variation of average temperature at section 2 for the flows with and without hydraulic jumps.

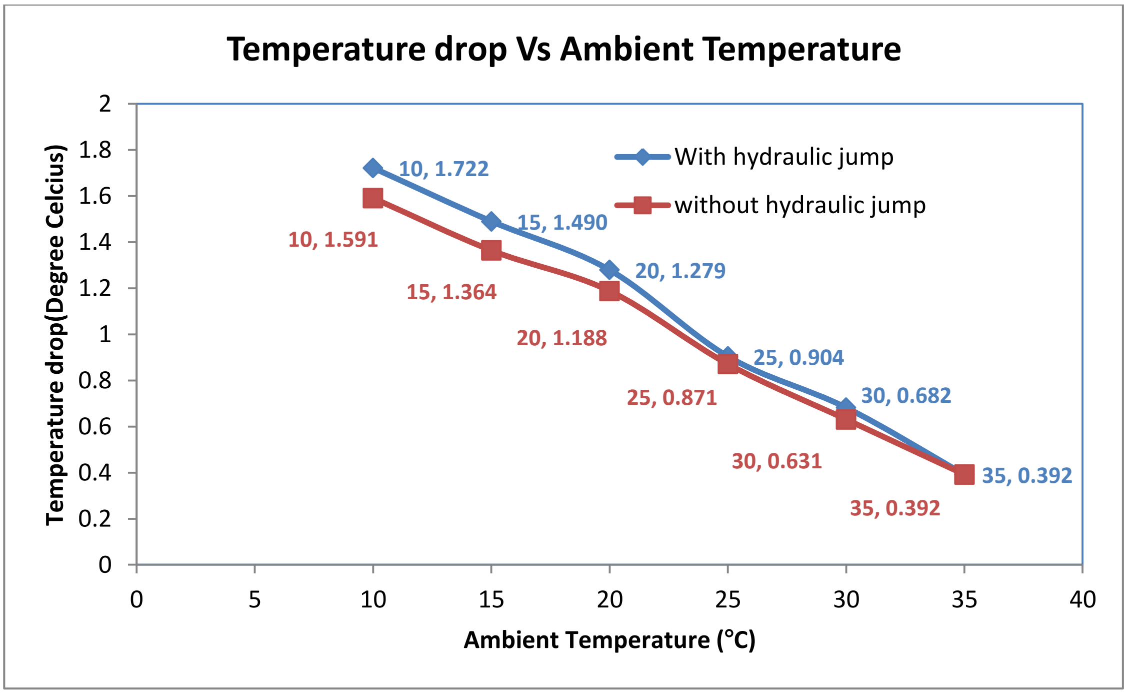

Fig. 5.2 Variation of Temperature drop due to hydraulic jump (ΔT_{jk}) and without hydraulic jump (ΔT_k)

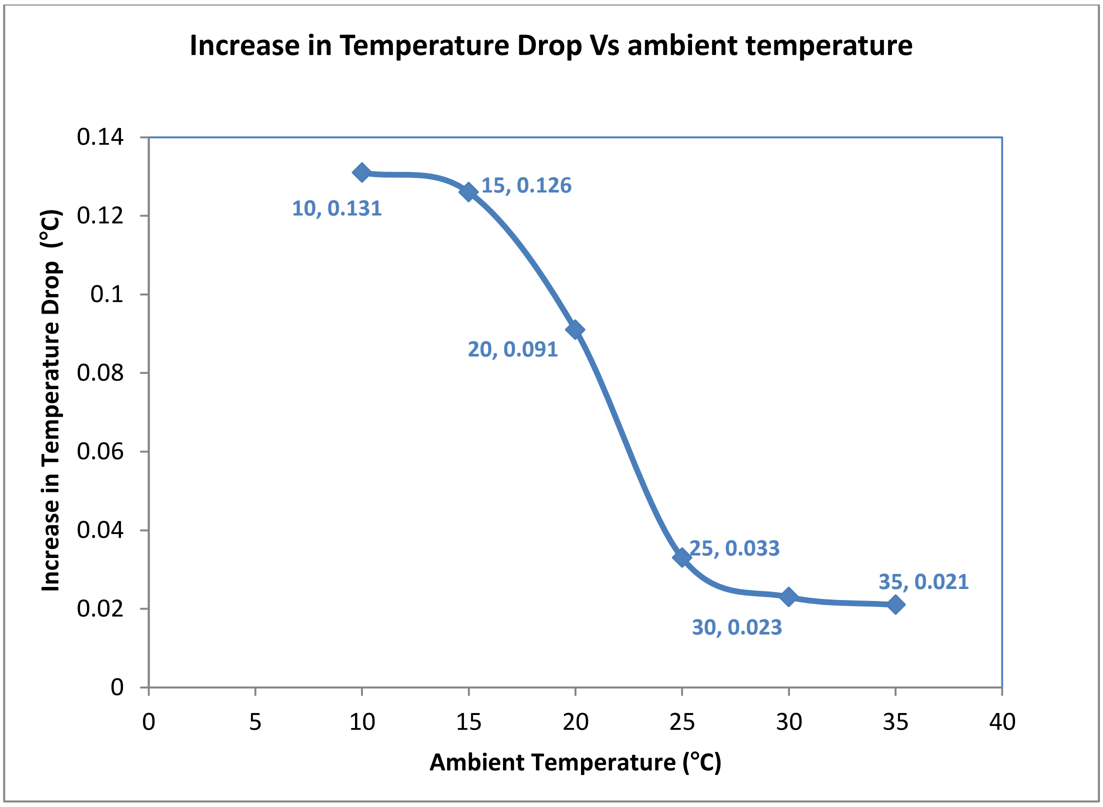

Fig. 5.3 Variation of increase in temperature drop due to hydraulic jump; (ΔT_{jk}-ΔT_k)

5.1.7.2 Specific Entropy drop

For all the simulations, Δs_{jk} denotes, the specific entropy drop occurring with the hydraulic jump in the kth simulation while Δs_k is the corresponding specific entropy drop occurring without the hydraulic jump in the kth simulation.

For simulation 1 with an ambient temperature of 10°C, Δs_{j1}=21.037 J/kg-K and Δs_1=19.27 J/kg-K. So, an increase of 1.767 J/kg-K in specific entropy drop due to hydraulic jump was observed.

In simulation 2 with an ambient temperature of 15°C, Δs_{j2}=17.824 J/kg-K and Δs_2=16.225 J/kg-K. The increase in specific entropy drop due to the hydraulic jump was 1.599 J/kg-K.

In simulation 3, the ambient temperature was 20°C and Δs_{j3}=15.068 J/kg-K and Δs_3 =13.835 J/kg-K. An increase in specific entropy drop due to hydraulic jump was observed to be 1.233 J/kg-K.

In simulation 4, the ambient temperature was 25°C and Δs_{j4}=10.335 J/kg-K and Δs_4 =9.618 J/kg-K. An increase in specific entropy drop due to hydraulic jump was observed to be 0.717 J/kg-K.

In simulation 5, the ambient temperature was 30ºC and Δs_{j5}=7.078 J/kg-K and Δs_5 =6.395 J/kg-K. An increase in specific entropy drop due to hydraulic jump was observed to be 0.683 J/kg-K.

In simulation 6 with the ambient temperature of 35ºC and Δs_{j6}=3.481 J/kg-K and Δs_6 =3.201 J/kg-K, the observable increase in specific entropy drop with the hydraulic jump was 0.280 J/kg-K.

Fig. 5.4 represents the variation of average specific entropy at section 2 with and without hydraulic jump for different ambient temperatures. Fig. 5.5 represents the variation of specific entropy drop (Δs_{jk}) and with the hydraulic jump and specific entropy drop (Δs_k) without hydraulic jump for different ambient temperatures.

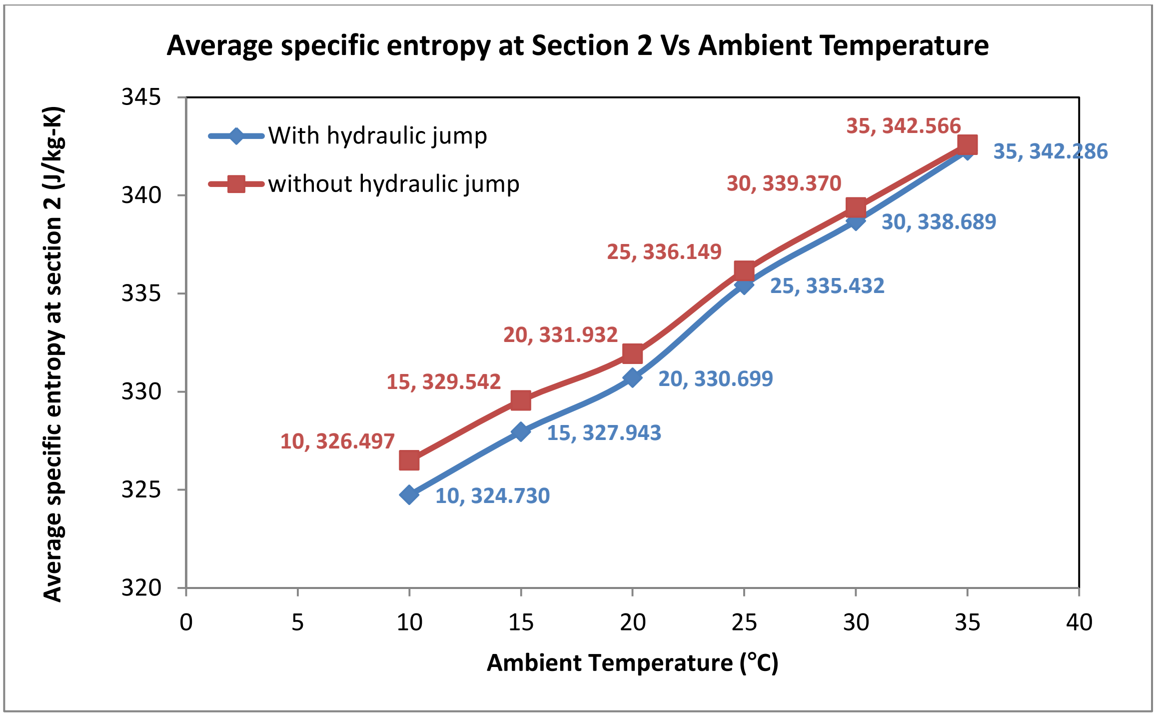

Fig. **5.4** Variation of average specific entropy at section 2 for the flows with and without hydraulic jumps.

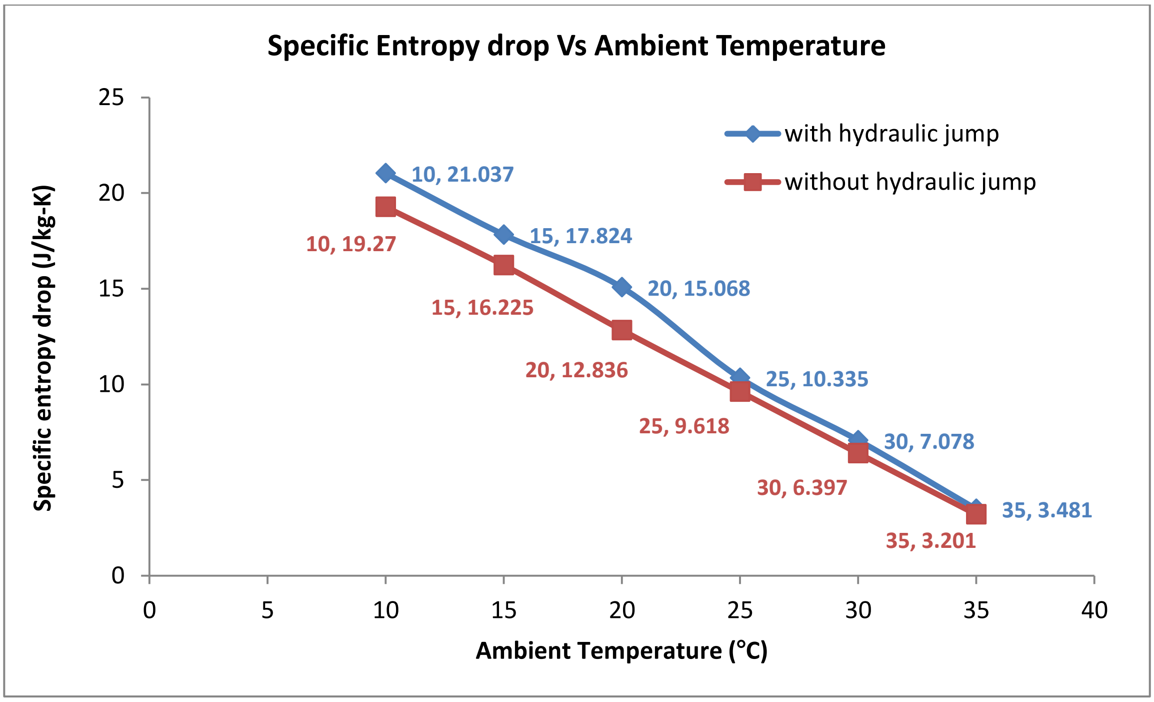

Fig. **5.5** Variation of specific entropy drop due to hydraulic jump (Δs_{jk}) and without hydraulic jump (Δs_k)

With the occurrence of the hydraulic jump, the increase(improvement) in specific entropy drop by hydraulic jump was found to decrease with an increase in ambient temperature. As shown in Fig. 5.6, the increase in specific entropy drop decreases rapidly between ambient temperatures of 10ºC to 25ºC. The rate of drop in specific enthalpy becomes less at 25°C and 30°C. From 30°C to 35°C, the drop in specific entropy was found to increase again.

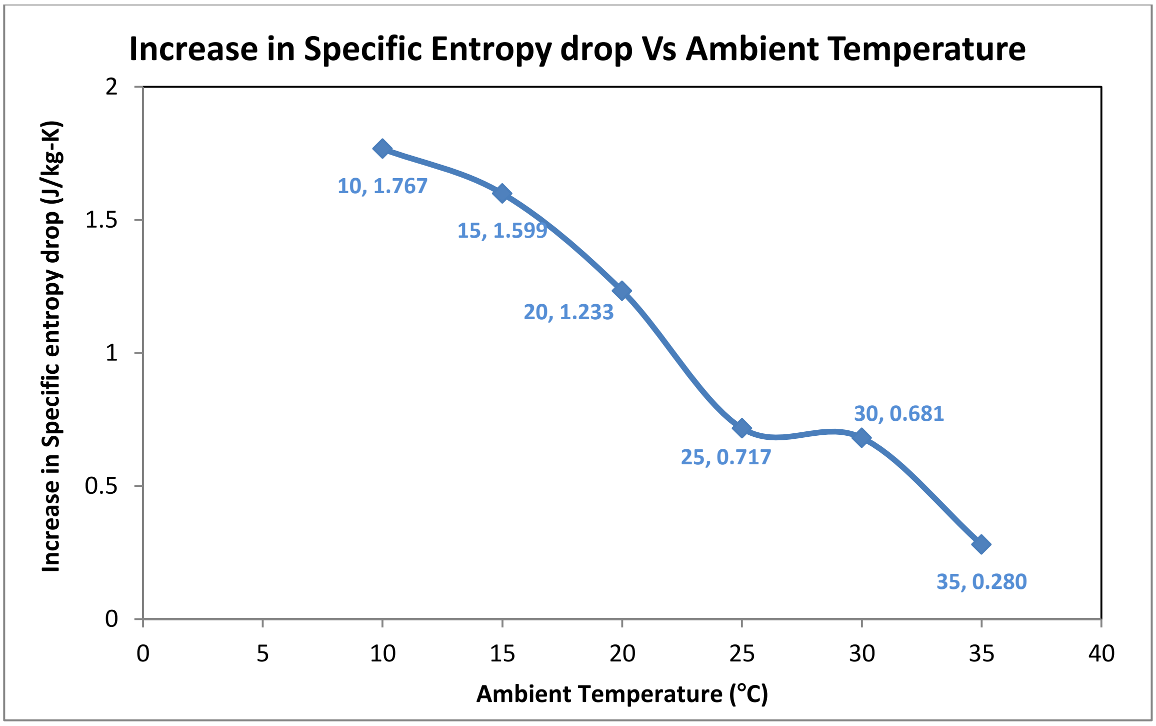

Fig. 5.6 Variation of increase in specific entropy drop due to hydraulic jump;(Δs_{jk}-Δs_k)

5.1.7.3 Specific Enthalpy drop

For all the simulations, Δh_{jk} denotes, the specific enthalpy drop occurring with the hydraulic jump in the kth simulation while Δh_k is the corresponding specific enthalpy drop occurring without the hydraulic jump in the kth simulation.

For simulation 1 with an ambient temperature of 10ºC, Δh_{j1}= 6566.4 J/kg and Δh_1= 6016.83 J/kg. So, an increase of 549.6 J/kg in specific enthalpy drop due to hydraulic jump was observed.

In simulation 2 with an ambient temperature of 15ºC, Δh_{j2}= 5566.0 J/kg and Δh_2= 5068.23 J/kg. The increase in specific enthalpy drop due to the hydraulic jump was 497.8 J/kg.

In simulation 3, ambient temperature was 20ºC and Δh_{j3}= 4707.4 J/kg and Δh_3 = 4011.93 J/kg. An increase in specific enthalpy drop due to hydraulic jump was observed to be 335.6 J/kg.

In simulation 4, ambient temperature was 25ºC and Δh_{j4}= 3230.5 J/kg and Δh_4 = 3007.43 J/kg. An increase in specific enthalpy drop due to hydraulic jump was observed to be 223.1 J/kg.

In simulation 5, ambient temperature was 30ºC and Δh_{j5}= 2213.3 J/kg and Δh_5 = 2001.430 J/kg. An increase in specific enthalpy drop due to hydraulic jump was observed to be 211.9 J/kg.

In simulation 6 with the ambient temperature of 35ºC and Δh_{j6}= 1089.4 J/kg and Δh_6 = 1002.430 J/kg, the observable increase in specific enthalpy drop with the hydraulic jump was 87.0 J/kg.

Fig. 5.7 shows the average enthalpy at section 2 for the flow with the hydraulic jump and without the hydraulic jump. Fig. 5.8 shows the specific enthalpy drops for the simulation with the hydraulic jump (Δh_{jk}) and without hydraulic jump (Δh_k) for all the six ambient temperatures. Fig. 5.9 shows the variation of increase in specific enthalpy drop due to hydraulic jump as compared to the specific enthalpy drop without the hydraulic jump. It was observed that the specific enthalpy drop was enhanced due to the hydraulic jump effect but this enhancement in enthalpy drop decreased with the increase in ambient temperature. The decrease in enthalpy drop increase was lesser from 10ºC to 15ºC ambient. From 15ºC to 25ºC, there was a sharp decrease in the enthalpy drop enhancement. From 25ºC to 30ºC, the decrease in enthalpy drop increase was very less but was again more from 30ºC to 35ºC.

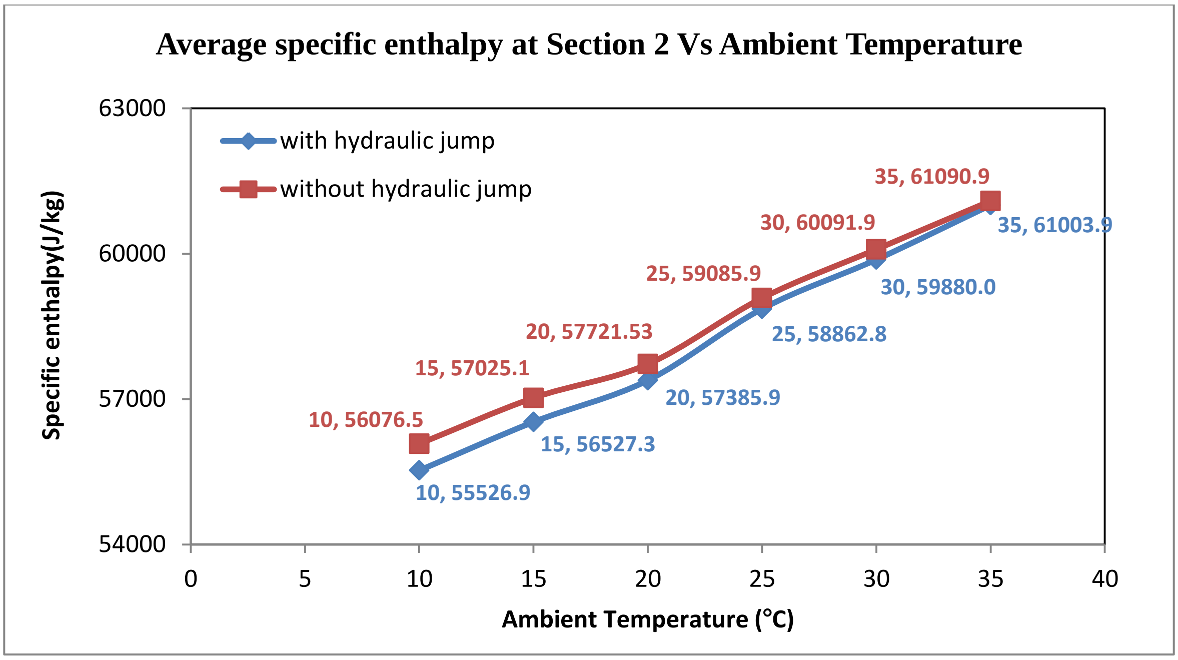

Fig. 5.7 Variation of average specific enthalpy at section 2 for the flows with and without hydraulic jumps

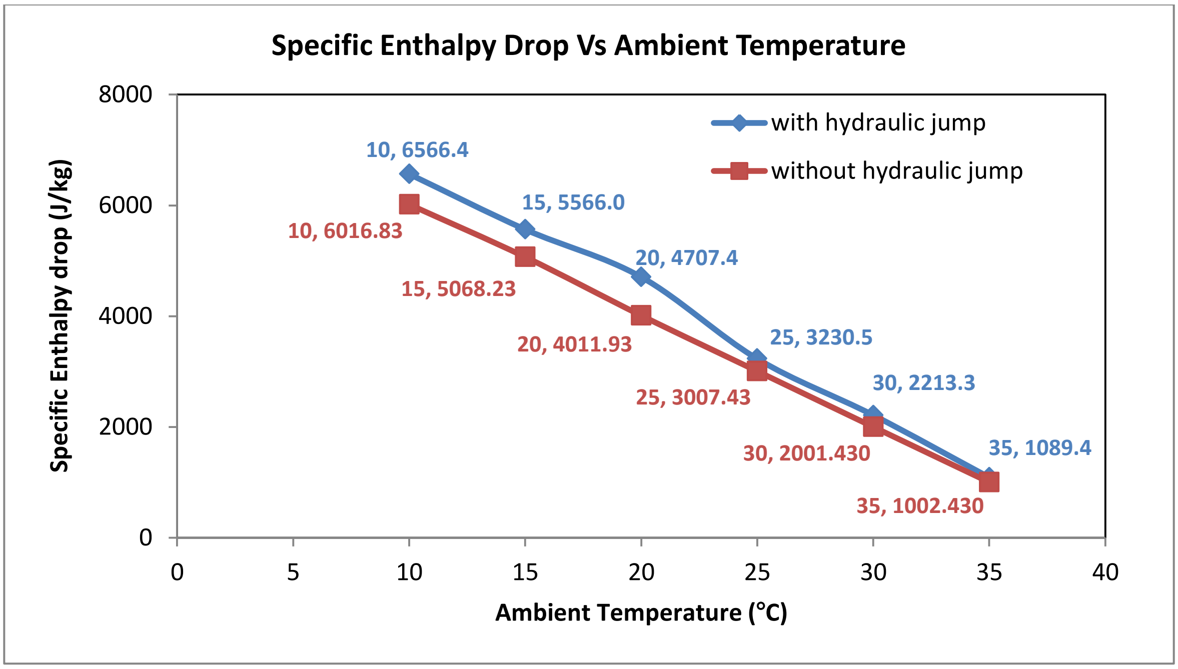

Fig. 5.8 Variation of specific enthalpy drop due to hydraulic jump (Δh_{jk}) and without hydraulic jump (Δh_k)

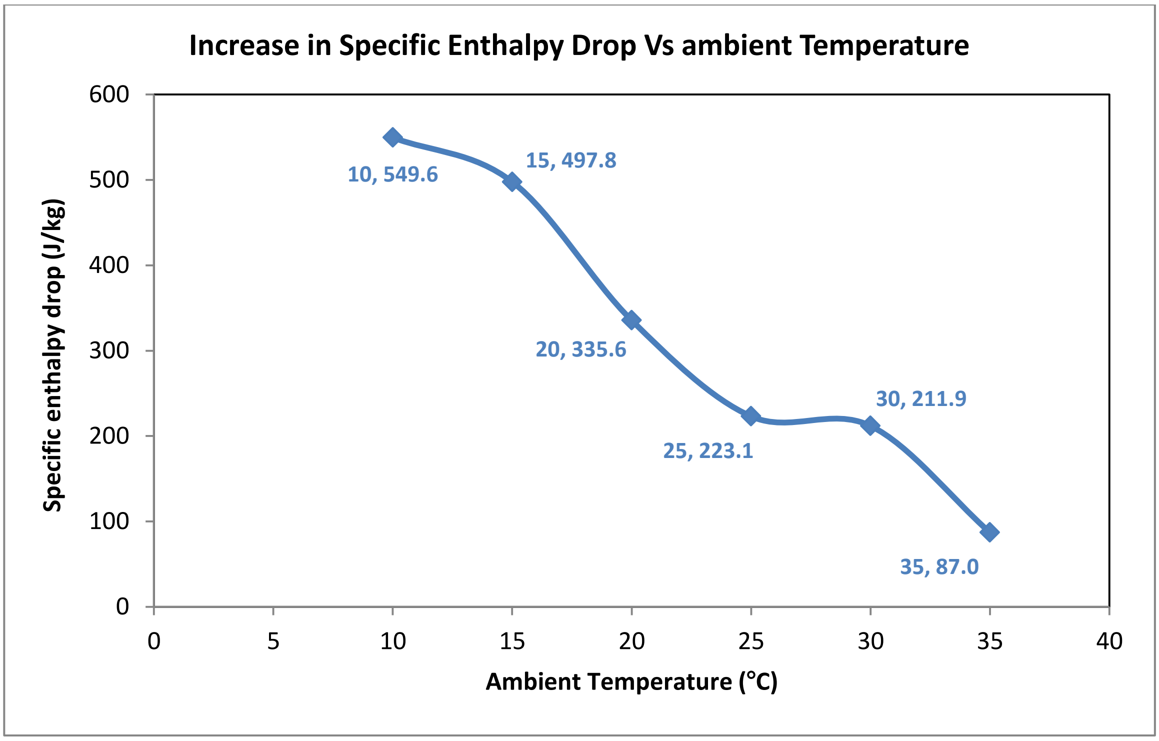

Fig. 5.9 Variation of increase in specific enthalpy drop due to hydraulic jump; (Δh_{jk}-Δh_k)

CHAPTER 6

6.1. Conclusions

Hydraulic jump in a rectangular flume with a mild slope of 1:2400 has been simulated using Ansys fluent. This study attempts to identify the capabilities of the hydraulic jump to dissipate heat from water at the constant inlet water temperature of 40°C and for different ambient temperatures. Six different ambient temperatures, from 10°C to 35°C with the steps of 5ºC, are considered. "Standard k-ε" turbulence model with standard wall function is adopted for the simulation and the "Energy" model is activated for incorporating the heat transfer by convection and conduction in the simulations. The "Volume of Fluid" model is used for tracking the free surface of the flow and to simulate the roller. Considering a section downstream of the hydraulic jump, the temperature, specific entropy, and specific enthalpy drops are measured with respect to the inlet conditions. These drops in the mentioned physical thermal quantities were compared with the corresponding drops occurring due to only convection at the free surface and conduction at walls.

The key findings of this study can be summarised as:

- The hydraulic jump increased the heat dissipation from the water to the ambient i.e. the average temperature at a cross-section downstream of the hydraulic jump was found to be less than the average temperature across the same section for a flow without the hydraulic jump.
- Improvement in average temperature drop by the hydraulic jump decreased with the increase in ambient temperature. The same can be concluded for the specific entropy and specific enthalpy. In other words, more was the difference in temperature between the water and the ambient, more was the enhancement of heat dissipation by the hydraulic jump
- The increase or improvement in temperature drop was found to be a non-linear function of the ambient temperature for a constant water inlet temperature.
- The maximum improvement in the temperature drop (0.131ºC) was obtained for the low ambient temperature of 10ºC.
- The enhancement in temperature drop fell rapidly for ambient temperatures greater than 15ºC and became constant at approximately 0.02ºC for ambient temperatures of 30ºC and 35ºC.

- The increases in specific entropy and specific enthalpy drops due to hydraulic jump were also a nonlinear function of the ambient temperature for the constant temperature of the water. Both the increase in specific entropy drop and specific enthalpy drop followed almost the same variation with ambient temperature.
- Maximum improvement in specific entropy drop and specific enthalpy drop occurred at low ambient temperatures of 10ºC and decreased rapidly for temperatures lesser than 15ºC.

CHAPTER 7

7.1. Future Scopes of the Study

The present study reveals the effect of hydraulic jump on the enhancement of heat dissipation that results in a certain improvement in temperature, specific entropy, and specific enthalpy decrease. However, due to the limitations of computational resources, the inlet temperature of the water was held constant and only the ambient temperatures were varied. As a result, the exact relationship between the capability of the hydraulic jump to enhance the heat dissipation with the temperature difference between water and the ambient could not be achieved. Also, the exact simulation of the actual operation of the tailgate was difficult to achieve and an approximate approach was adopted. This resulted in a longer simulation time for obtaining a stable location of the hydraulic jump toe. With varying the ambient temperature, the monotonically decreasing trend of the enhancement in specific entropy and specific enthalpy drop showed some anomalies between 25ºC and 30ºC.

The following considerations can resolve the above issues:

- Use of higher computational resources such as systems with RAM at least 16 GB and clock speed greater or equal to 2.4 GHz in conjunction with the disk space greater than 500 GB dedicated for the purpose, shall allow performing a greater number of simulations for different ambient temperatures and different inlet water temperatures.
- Adopting very fine mesh (with the mesh size lesser than 0.01 m) at the region of formation of hydraulic jump shall resolve the roller much better. This will enhance the computations of heat dissipation due to the hydraulic jump.
- The use of a higher fidelity turbulence model such as “Realizable k-ε” is always recommended for simulations involving vigorous turbulence.
- The boundary condition corresponding to the tailgate can be modified using dynamic mesh or any suitable UDF for simulating the actual operation of a tailgate.

NOTATIONS:

The following notations have been used in this dissertation work:

α_k , α_ε = inverse turbulent Prandtl numbers for k and ε Equations respectively

α_q = volume fraction of the q^{th} phase in a computational cell.

α_t = turbulent diffusivity

C_k = Kolmogorov constant

C_p = Specific heat capacity at constant pressure

δ_{ij} = Kronecker's delta

ε_{ijk} = permutation tensor

E_1 = initial Specific energy of the supercritical flow

E_2 = specific energy of the supercritical flow

E_L = loss in specific energy

ε = turbulent kinetic energy dissipation (rate) per unit mass

F_1 = initial Froude number (of supercritical flow)
fraction

f_i = i^{th} component of body force per unit mass

G_b = generation of turbulence kinetic energy due to buoyancy effects

G_k = generation of turbulence kinetic energy due to mean velocity gradients

Gr = Grashof’s number

Δh_{jk} = specific enthalpy drop occurring with the hydraulic jump in the k^{th}

Δh_k = specific enthalpy drop occurring without the hydraulic jump in

k = turbulent kinetic energy per unit mass

κ = wavenumber

μ = dynamic viscosity of the fluid

μ_t = Eddy (dynamic) viscosity

μ_{eff} = effective viscosity

μ_{mol} = molecular viscosity

η = Kolmogorov length scale

p = pressure

p' = fluctuating component of pressure

$\overline{p}$ = mean component of the pressure

Pr_t = turbulent Prandtl number

R = Characteristic gas constant

Ra = Rayleigh’s number

Re = Reynolds number

$S_{\alpha q}$ = user defined mass source of the phase in transport equation for volume fraction

S_{ij} = rate of strain tensor; $S_{ij} = \frac{1}{2}\left(\frac{\partial u_i}{\partial x_j} + \frac{\partial u_j}{\partial x_i}\right)$

Δs_{jk} = specific entropy drop occurring with the hydraulic jump in the kth simulation

Δs_k = specific entropy drop occurring without the hydraulic jump in kth simulation

S_k , S_ε = are user-defined source terms in k and ε transport Equations respectively

ΔT_{jk} = the temperature drop occurring with the hydraulic jump in the kth simulation

ΔT_k = temperature drop occurring without the hydraulic jump in the kth simulation

τ = Kolmogorov time scale

τ_{ij} = Reynolds stress tensor

τ_t = Reynolds stress

u_i = ith component of the velocity vector

u_i' = ith component of instantaneous fluctuating velocity

$\bar{u}_i$ = ith component of mean turbulent velocity

U = average velocity of mean strained flow

V_1 = initial velocity of (supercritical) flow

ν_t = Eddy (kinematic) viscosity

υ_η = Kolmogorov velocity scale

x_i = ith component of space –coordinate

y_1 = Depth of flow for the supercritical stream

y_2 = Depth of flow for the subcritical stream

Y_M = the contribution of fluctuating dilatation in

- $\rho\overline{u_i'u_j'}$ = component of Reynolds stress tensor

θ' = fluctuating component of temperature

$\bar{\theta}$ = mean component of temperature

$\rho\overline{u^2}$ = Normal component of Reynolds stress in incompressible strained mean flow

Ω_{ij} = Rate of rotation tensor ; $\Omega_{ij} = \frac{1}{2}(\frac{\partial u_i}{\partial x_j} - \frac{\partial u_j}{\partial x_i})$

θ = temperature

γ = Ratio of specific heat capacities

ρ = density of the fluid

ρ_q = density of qth phase

σ_k, σ_ε = turbulent Prandtl numbers for k and ε transport Equations respectively

REFERENCES

Abbaspour, A., & Farsadizadeh, D. (2009). Numerical study of hydraulic jumps on corrugated beds using turbulence models. *Turkish Journal of Engineering and Environmental Sciences*, *33*(1), pp. 61-72.

Argaman, Y. (1977). Comprehensive temperature model for aerated biological systems. Prog. Wat. Tech. Vol. 9, pp. 397-409, Pergamon Press, 1977.

Baddour, R. E. (1991). Thermal hydraulic jump: theory and experiment. *Journal of fluid mechanics*, *226*, pp. 243-256.

Bayon, A., & Lopez-Jimenez, P. A. (2015). Numerical analysis of hydraulic jumps using OpenFOAM. *Journal of Hydroinformatics*, *17*(4), pp. 662-678.

Bayon, A., Valero, D., García-Bartual, R., & López-Jiménez, P. A. (2016). Performance assessment of OpenFOAM and FLOW-3D in the numerical modeling of a low Reynolds number hydraulic jump. *Environmental modelling & software*, *80*, pp. 322-335.

Carvalho, R. F., Lemos, C. M., & Ramos, C. M. (2008). Numerical computation of the flow in hydraulic jump stilling basins. *Journal of Hydraulic Research*, *46*(6), pp. 739-752.

Chanson, H. (2007). Bubbly flow structure in hydraulic jump. *European Journal of. Mechanics-B/Fluids*, *26*(3), pp. 367-384.

Chippada, S. (1996). *Numerical study of thin-film flows and open-channel flows*. Rice University

Davidson, L. (2018). Fluid mechanics, turbulent flow and turbulence modelling. *Chalmers University of Technology, Goteborg, Sweden (June 19, 2022).*

Ford, D. L., Chih, S. S., & Sobosta, E. C. (1972).Temperature prediction in activated sludge basins using mechanical screens. In *Proceedings of the 27th Industrial Waste Conference, Purdue University, West Lafayette, Indiana, May* (Vol. 27, p.587).

Gulliver, J. S., Thene, J. R., & Rindels, A. J. (1990). Indexing gas transfer in self-aerated flows. *Journal of environmental engineering*, *116*(3), pp. 503-523.

Harada, S., & Li, S. S. (2018). Modelling hydraulic jump using the bubbly two-phase flow method. *Environmental Fluid Mechanics*, *18*(2), pp. 335-356.

Hirt, Cyril W., and Billy D. Nichols. "Volume of fluid (VOF) method for the dynamics of free boundaries." *Journal of computational physics* 39, no. 1 (1981): pp.201-225.

Jobson, H. E., & Keefer, T. N. (1979). Modeling highly transient flow, mass, and heat transport in the Chattahoochee River near Atlanta, *Georgia* (Vol. 1136). US Government Printing Office.

Launder, B. E., & Spalding, D. B. (1983). The numerical computation of turbulent flows. In *Numerical prediction of flow, heat transfer, turbulence and combustion* (pp. 96-116). Pergamon.

Ma, J., Oberai, A. A., Lahey, R. T., & Drew, D. A. (2011). Modeling air entrainment and transport in a hydraulic jump using two-fluid RANS and DES turbulence models. *Heat and mass transfer*, *47*(8), pp. 911-919.

Marriott, M., & Jayaratne, R. (2010). Hydraulic roughness–links between Manning's coefficient, Nikuradse's equivalent sand roughness and bed grain size. *Advances in Computing and Technology 2010*, pp. 27-32.

Mollik, T., Roy, B., & Saha, S. (2017). Turbulence modeling of channel flow and heat transfer: A comparison with DNS data. *Procedia Engineering*, *194,* pp. 450-456.

Moss, M. D. (1976). *The effects of roughness on heat transfer from open channel flow* (Doctoral dissertation, Georgia Institute of Technology).

Novotny, V., & Krenkel, P. A. (1973). Evaporation and heat balance in aerated basins. In *AIChE Symposium Series* (Vol. 70, No. 136, pp. 150-159).

Rahber, Nader, and Mehdi H. (2008)."Study of Hydraulic Jump on Heat Transfer at Various."5th WSEAS International Conference on FLUID MECHANICS (FLUIDS'08) Acapulco, Mexico, January 25-27, 2008

Rashidi, M., Hetsroni, G., & Banerjee, S. (1991). Mechanisms of heat and mass transport at gas-liquid interfaces. *International journal of heat and mass transfer*, *34*(7), pp. 1799-1810.

Sarkar, S., & Lakshmanan, B. (1991). Application of a Reynolds stress turbulence model to the compressible shear layer. *AIAA Journal*, *29*(5), pp. 743-749.

Shih, T. H., Liou, W. W., Shabbir, A., Yang, Z., & Zhu, J. (1994). *A new k-epsilon eddy viscosity model for high Reynolds number turbulent flows: Model development and validation* (No. CMOTT-94-6).

Spalding, D. B. (1977). Heat and Mass Transfer in Rivers, Bays, Lakes, and Estuaries. In *Advances in Heat Transfer* (Vol. 13, pp. 61-117). Elsevier.

Stang, O. (1982). On the Heat Exchange Between Rivers and Atmosphere. *Hydrology Research*, *13*(2), 65.

Talati, S. N. (1988). *Heat loss in aeration tanks* (Master's thesis, UCLA).

Valero, D., Viti, N., & Gualtieri, C. (2018). Numerical simulation of hydraulic jumps. Part 1: Experimental data for modelling performance assessment. *Water*, *11*(1), 36.

Wang, Y., & Khayat, R. E. (2019). The influence of heating on liquid jet spreading and hydraulic jump. *Journal of Fluid Mechanics*, *883*. doi:10.1017/jfm.2019.924

Williams, G.P., 1963. Heat transfer coefficients for natural water surfaces (pp. 203-212). National Research Council Canada, Division of Building Research.

Yakhot, V., & Orszag, S. A. (1986). Renormalization group analysis of turbulence. I. Basic theory. *Journal of scientific computing*, *1*(1), pp. 3-51.

Zhao, Q., Misra, S. K., Svendsen, I. A., & Kirby, J. T. (2004, June). Numerical study of a turbulent hydraulic jump. In *Proceeding of 17th Engineering Mechanics Conference, University of Delaware, New York.*